Chapter 5

(Results and Discussion)

5.1. PART-I: SERIES-I

5.1.1. Computational studies

5.1.1.1. Pharmacophore modelling

The crystal structures of hAChE (PDB code: 4EY7) and hBACE-1 (PDB code: 2ZJM) were utilized to create e-pharmacophore models using the structure-based drug design approach [Cheung et al. 2012, Godemann et al. 2009, Sharma et al. 2019b]. These crystal structures were chosen because their co-crystallized ligands contain the N-benzylpiperidine nucleus (donepezil and F1M). The hAChE e-pharmacophore model suggested the presence of hydrogen bond acceptor (A3), presence of two hydrophobic residues (H7 and H8), the presence of two aromatic rings (R10 and R11), and two hydrophobic residues (H7 and H8). While the hBACE-1 e-pharmacophore model suggested the presence of two hydrogen bond donors (D7 and D8), a single positive ionic group (P13), and the presence of two aromatic rings (R14 and R15) as the necessary pharmacophoric features for hAChE and hBACE-1 model (Figure 5.1).

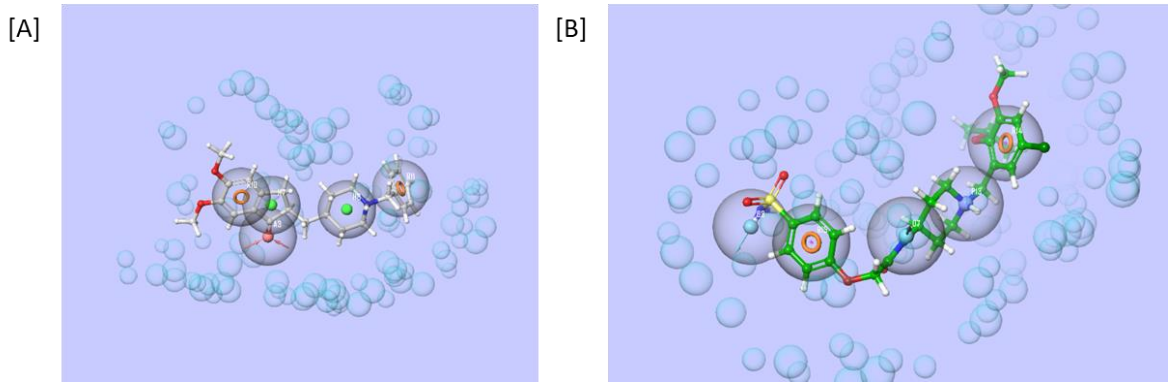

Figure 5.1. e-pharmacophore models representing their binding sites. [A] hAChE (PDB code: 4EY7); [B] hBACE-1 (PDB code: 2ZJM)

Utilizing these pharmacophoric characteristics, the ZINC15 database (accessed at https://zinc.docking.org in January 2020) compounds were screened using the Phase module of Schrödinger Maestro 2018_1. In this study, we used ZINC database which is

quite bigger as compared to the previously used database (Maybridge) with an anticipation that the chances of getting a new lead that should be entirely different from previously reported hits would be higher (low hit repetition probability) [Sharma et al. 2019b]. Phase screening of 193889 compounds through both these e-pharmacophore models (hAChE and hBACE-1) yielded 1000 hits, initially. The pharmacophore overlay of identified hit (**ZINC000015441499**) and compound **AV-2** on both AChE and BACE-1 were explored because earlier from our lab Sharma et al., also tried to develop the e-pharmacophore hypothesis on AChE and BACE-1 based on the N-benzylpiperidine nucleus and screened Maybridge database via phase screening and vsw methods which leads to the identified hit (**SEW06622**) having N-benzylpiperidine nucleus but in this study, both identified hit (**ZINC000015441499**) and compound **AV-2** possessed the quinazoline scaffold which is different from the previous study. The pharmacophoric study of the identified hit (**ZINC000015441499**) suggested that three rings (R7, R9, and R10), two hydrogen bond acceptors (A2 and A3), and a hydrophobic (H6) against hAChE and three rings (R7, R9 and R10) and a hydrogen bond acceptor (A2) against hBACE-1 were the necessary pharmacophoric features. While in case of hit **SEW06622**, two aromatic rings (R6 and R7) and a hydrogen bond acceptor (A1) were the essential pharmacophoric features against both the hAChE and hBACE-1 enzymes [Sharma et al. 2019b]. The details of the pharmacophoric features of identified hits **ZINC000015441499**, **SEW06622**, Donepezil, F1M, and compound **AV-2** on both hAChE and hBACE-1 models have been discussed and represented in Table 5.1.

Table 5.1. Table representing pharmacophoric features on hAChE and hBACE-1 models. [A] donepezil on hAChE; [B] F1M on hBACE-1; [C] hit **ZINC000015441499** on hAChE; [D] hit **ZINC000015441499** on hBACE-1; [E] **AV-2** on hAChE; [F] **AV-2** on hBACE-1; [G] hit **SEW06622** on hAChE; and hit **SEW06622** on hBACE-1.

[A] Pharmacophoric features of donepezil with hAChE						
Rank	**Feature label**	**Score**	**X**	**Y**	**Z**	**type**
1	H8	-2.3	-12.4244	-45.54	29.0397	H
2	A3	-1.7	-14.4551	-43.4543	23.906	A
3	R11	-1.56	-8.6407	-44.656	31.7985	R
4	R10	-1.24	-17.7708	-42.2845	25.3112	R
5	H7	-1.2	-15.7706	-43.0133	25.9866	H
[B] Pharmacophoric features of F1M with hBACE-1						
Rank	**Feature label**	**Score**	**X**	**Y**	**Z**	**type**
1	R14	-0.9	34.015	41.8233	3.4747	R
2	R15	-0.81	24.0208	36.6615	1.0166	R
3	P13	-0.59	32.1972	38.5883	2.6046	P
4	D7	-0.35	27.9694	37.2259	3.9117	D
5	D8	-0.16	22.1983	37.0676	-2.6383	D
[C] Pharmacophoric features of hit **ZINC000015441499** with hAChE						
Rank	**Feature label**	**Score**	**X**	**Y**	**Z**	**type**
1	A3	-1.51	-14.9802	-42.3376	22.9503	A
2	R7	-1.32	-14.903	-43.2785	26.3711	R
3	R10	-1.01	-10.1799	-45.2799	30.0684	R
4	R9	-0.85	-18.4616	-41.8536	23.8666	R
5	H6	-0.8	-11.8339	-46.9014	27.3757	H
6	A2	-0.67	-11.9176	-42.7737	27.9158	A
[D] Pharmacophoric features of hit **ZINC000015441499** with hBACE-1						
Rank	**Feature label**	**Score**	**X**	**Y**	**Z**	**type**
1	R10	-0.7	25.7759	35.3691	1.6385	R
2	R9	-0.57	34.233	41.9007	1.2042	R
3	A2	-0.56	26.8878	38.7838	1.2646	A
4	R7	-0.52	30.1666	39.8115	1.4699	R

[E] Pharmacophoric features of **AV-2** with hAChE						
Rank	**Feature label**	**Score**	**X**	**Y**	**Z**	**type**
1	H3	-2.18	-16.659	-42.2311	22.918	H
2	R7	-1.8	-14.7012	-43.7036	26.9089	R
3	R4	-1.06	-20.7029	-41.5541	25.4578	R
4	R6	-0.74	-22.1666	-38.2437	20.1219	R
[F] Pharmacophoric features of **AV-2** with hBACE-1						
Rank	**Feature label**	**Score**	**X**	**Y**	**Z**	**type**
1	R6	-0.83	30.5699	31.5597	-0.133	R
2	R4	-0.81	25.8312	35.4223	1.8595	R
3	A1	-0.7	27.4506	33.3905	0.8798	A
4	R7	-0.6	34.2131	41.4328	1.0201	R
[G] Pharmacophoric features of **SEW06622** with hAChE						
Rank	**Feature label**	**Score**	**X**	**Y**	**Z**	**type**
1	R6	-1.45	-16.2622	-42.8629	25.9144	R
2	R7	-1.42	-8.5314	-44.0368	32.4519	R
3	A1	-0.7	-14.6008	-43.4483	23.7769	A
[G] Pharmacophoric features of **SEW06622** with hBACE-1						
Rank	**Feature label**	**Score**	**X**	**Y**	**Z**	**type**
1	R7	-0.88	34.6845	41.7577	0.0676	R
2	R6	-0.84	25.6103	35.3917	1.891	R
3	A1	-0.54	27.3966	33.5319	0.8335	A
4	P5	-0.35	28.9015	37.0518	2.5661	P

The pharmacophore overlay of compound **AV-2** on hAChE suggested that the benzene ring of quinazoline moiety, phenyl, and benzyl ring were mimic the aromatic rings (R4, R6, and R7), piperazine moiety represents the hydrophobic (H3) character which could be considered as necessary pharmacophoric features for hAChE model. While the benzene ring of quinazoline moiety, phenyl, and benzyl ring represents aromatic rings (R4, R6, and R7), nitrogen atom of quinazoline mimics hydrogen bond acceptor (A1) of compound

AV-2 which can be regarded as necessary pharmacophoric features for hBACE-1 model (Figure 5.2).

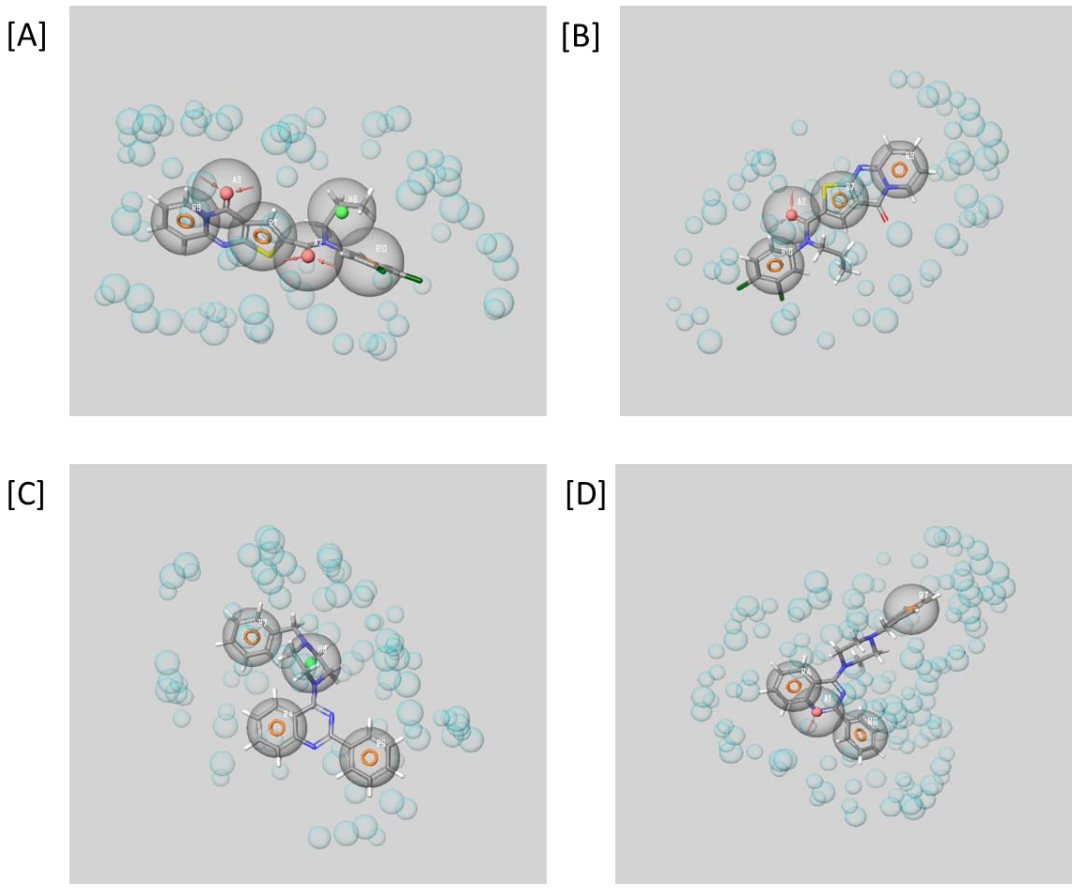

Figure 5.2. The pharmacophore overlay of hit (**ZINC000015441499**) and compound **AV-2**. [A] **ZINC000015441499** on AChE; [B] **ZINC000015441499** on BACE-1; [C] **AV-2** on AChE; [D] **AV-2** on BACE-1.

5.1.1.2. Virtual screening

Further, virtual screening workflow (vsw) was adopted, which consists of three steps high throughput virtual screening (HTVS), standard precision (SP), and extra precision (XP) and was set at the filtration criteria of 50%, 50%, and 25% respectively. The vsw resulted in 22 potential hits for AChE and BACE-1 individually which were further subjected to pose filtration using DPP function.

Two significant binding sites like PAS (Tyr72, Asp74, Tyr124, Trp286, and Tyr341) and CAS (Ser203, Glu334, and His447) were mainly considered for hAChE inhibitory

activity while Asp32 and Asp228 dyad residues at the N- and C-terminus interface were considered for hBACE-1 inhibitory activity. While, other binding sites including oxyanion hole (Gly120, Gly12, and Gly122), acyl binding site (Trp236, Phe295, and Phe297), and anionic subsite (Trp86, Glu202, and Phe338) for hAChE were also considered as they not only help in encroaching the compound to the enzyme active pocket but also play a significant role in improving the binding profile and stability of ligand-receptor complex [Carletti et al. 2010].

Therefore, as per their interaction with hAChE's CAS and PAS residues and aspartate dyad residues of hBACE-1, the DPP function resulted in three common hits (**ZINC000015441499**; **ZINC000010322640; ZINC000408991674**) for both the enzymes. These common hits were showing a good binding profile with the essential amino acids present at the active sites of both these targets (Figure 5.3).

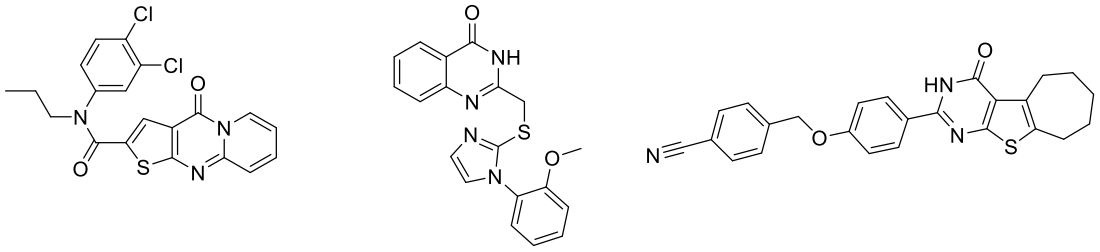

[A] ZINC000015441499 [B] ZINC000010322640 [C] ZINC000408991674

Figure 5.3. Structures of common identified hits. [A] **ZINC000015441499**; [B] **ZINC000010322640**; [C] **ZINC000408991674**.

Table 5.2. Molecular docking score and their respective MM-GBSA, ΔG (binding free energy) of identified hits against hAChE and hBACE-1.

Compd.	hAChE			MM-GBSA score (AChE)	hBACE-1		MM-GBSA score (BACE-1)
	Glide score	Interacting residues*			Glide score	Aspartate dyad interactions*	
		PAS	CAS				
ZINC000015441499	-19.98	Tyr72[a], Asp74[b], Tyr124[a], Trp286[a], Tyr341[a,c]	Ser203[d], His447[d]	-81.98	-6.89	Asp32[b], Asp228[b]	-63.21
ZINC000010322640	-14.72	Asp74[b], Tyr124[a], Trp286[a], Tyr341[a,c]	Ser203[d], His447[d]	-75.93	-5.23	Asp32[b,], Asp228[b]	-57.11
ZINC000408991674	-11.73	Tyr72[a], Asp74[b], Tyr124[a], Trp286[a,g] Tyr341[a,g]	Ser203[d], His447[d]	-65.52	-4.85	Asp32[b,], Asp228[b]	-50.36

* Interacting residues were observed within the distance of 5Å from ligands.

[a] hydrophobic; [b] charged; [c] π-cation; [d] polar; [e] salt-bridge; [f] H-bonding; [g] π- π stacking

5.1.1.3. MM-GBSA

Further, to determine the binding free energy of the 3 identified hits, the MM-GBSA analysis was performed on both the enzymes (hAChE and hBACE-1), which resulted in hit **ZINC000015441499** (Table 5.2) as the top scoring hit (based on docking and MM-GBSA score) with the minimum binding free and docking energy of -81.98 and -63.21 kcal/mol for both the enzymes, respectively.

5.1.1.4. Molecular Docking

For molecular docking studies initially, the co-crystallized ligands were extracted and re-docked into the prepared grids of hAChE and hBACE-1 enzymes to validate the generated grids. The superposition tool was employed to calculate the RMSD fluctuations in the re-docked and bound ligand which demonstrated that the RMSD values of co-crystallized and re-docked ligands were laying within the acceptable range of ≤ 2 Å

[Kontoyianni et al. 2004]. These validated grids were used to perform molecular docking studies of **ZINC000015441499** and the most promising ligand **AV-2.** The docking studies results indicated that the 4-oxo-N-propyl-4H-pyrido[1,2-a]thieno[2,3-d]pyrimidine-2-carboxamide moiety of hit compound **ZINC000015441499** and quinazoline moiety attached with phenyl ring of **AV-2** occupied the hAChE-PAS region, while N-(3,4-dichlorophenyl) moiety of top hit and benzylpiperazine scaffold of **AV-2** were encroached deep into CAS and involved in the formation of polar bonds with Ser203 and His447. The top hit and **AV-2** displayed charged (negative) and hydrophobic interactions with Asp74 and PAS amino acids (Tyr72, Tyr124, Trp286, and Tyr341), respectively. The thieno[2,3-d]pyrimidine-2-carboxamide nucleus of top hit showed π-π stacking interaction with Trp286 while **AV-2** displayed π-π stacking interaction with Tyr124 amino acid residues of the PAS region. The N-(3,4-chlorophenyl) group of top hit and quinazoline moiety of **AV-2** also showed hydrophobic and charged interaction with Trp86 and Glu202 of anionic subunit subsite, respectively (Figure 5.4, Figure 5.5, Figure 5.6, and Figure 5.7). The docking study of top hit and **AV-2** with hBACE-1 enzyme suggested that the oxo group present on the top hit and piperazine ring of **AV-2** were interacting electrostatically with both catalytic aspartate amino acid residues (Asp32 and Asp228) (Figure 5.4, Figure 5.5, Figure 5.6, and Figure 5.7).

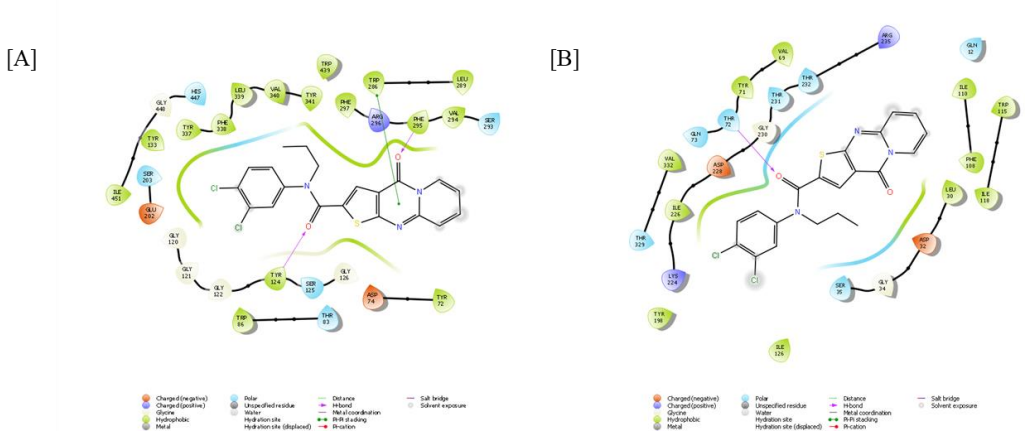

Figure 5.4. 2D binding pattern of **ZINC000015441499** on [A] hAChE (4EY7) and [B] hBACE-1 (2ZJM), respectively.

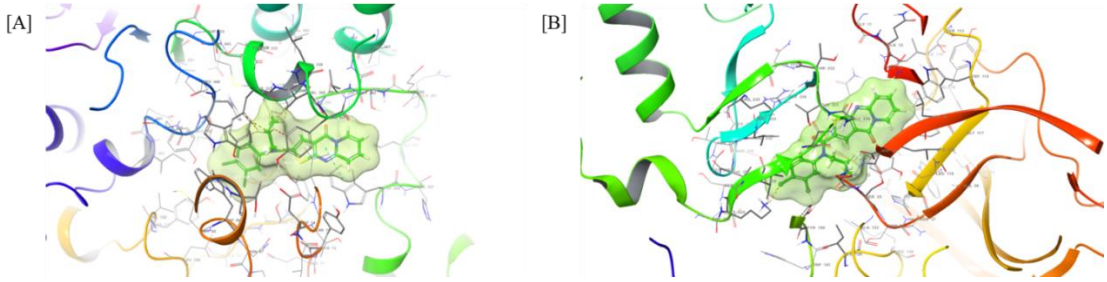

Figure 5.5. 3D binding pattern of **ZINC000015441499** on [A] hAChE (4EY7) and [B] hBACE-1 (2ZJM), respectively.

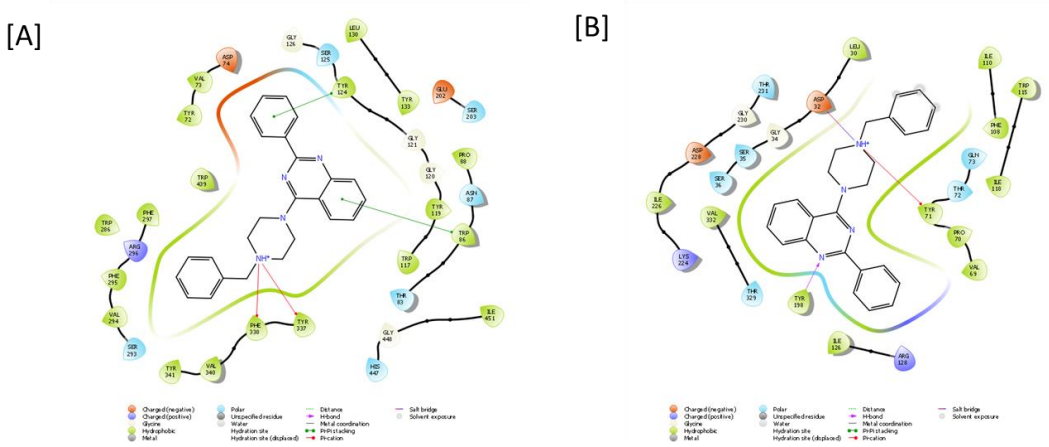

Figure 5.6. 2D binding pattern of compound **AV-2** on [A] hAChE (4EY7) and [B] hBACE-1 (2ZJM), respectively.

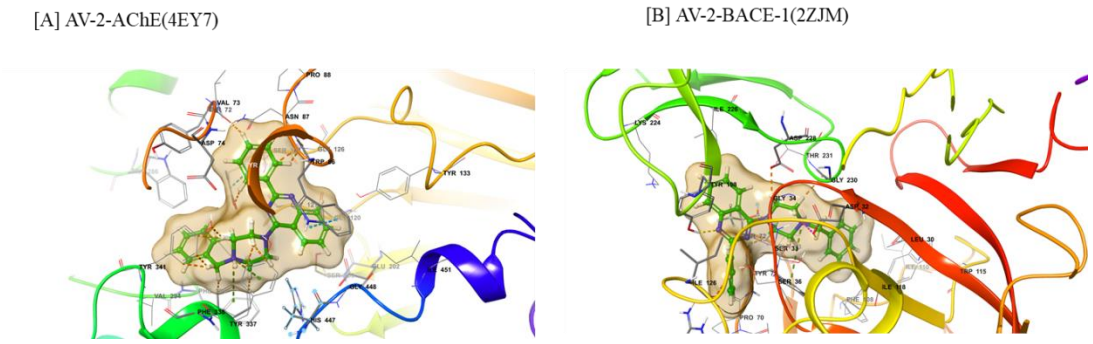

Figure 5.7. 3D binding pattern of compound **AV-2** with [A] hAChE (4EY7) and [B] hBACE-1 (2ZJM), respectively.

5.1.1.5. Molecular Dynamics Simulation

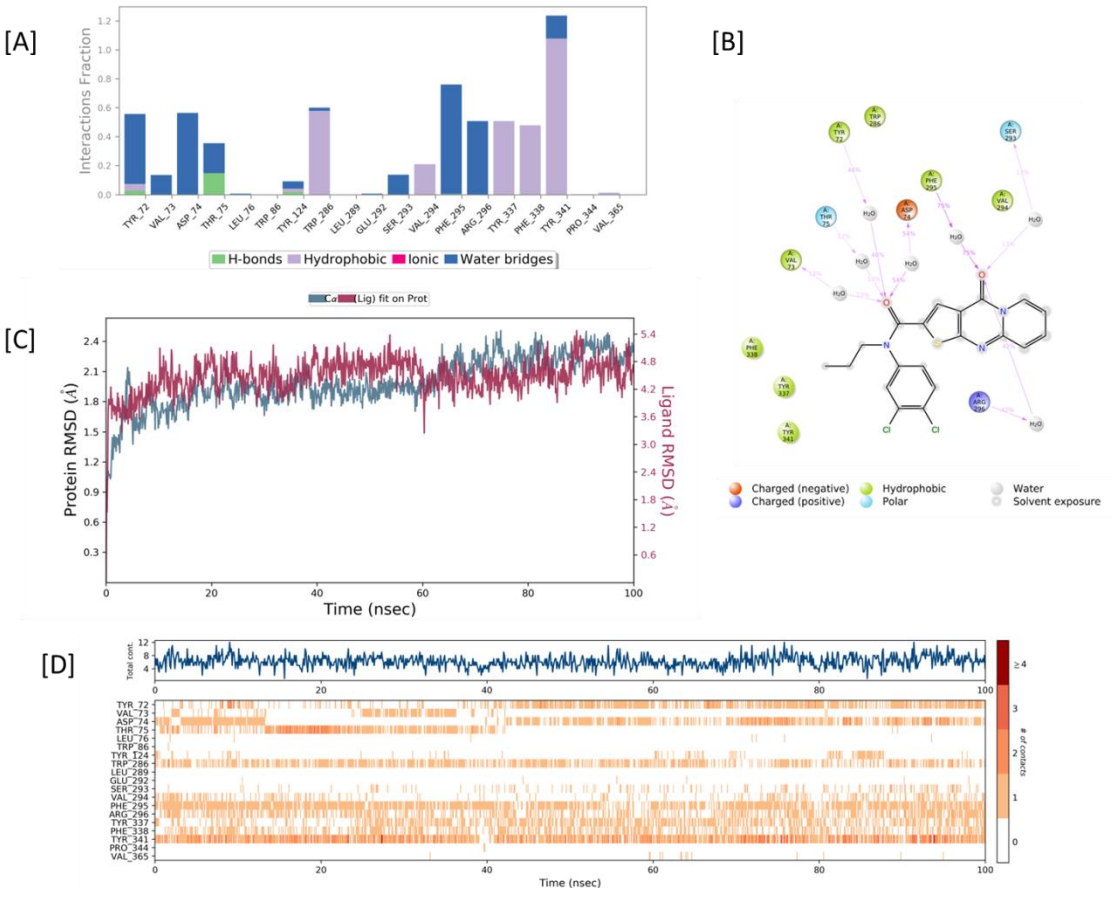

Figure 5.8. Molecular dynamics studies of ZINC000015441499-hAChE (4EY7) docked complex. [A] Histogram showing interaction fractions with active amino acid residues; [B] Graphical representation showing percentage interactions with active site residues; [C] RMSD graph of ligand-protein (ZINC000015441499-hAChE); [D] Timeline representation showing interaction with all the amino acid residues at each time frame.

Further, MD simulation runs of 100 ns were undertaken for the docked complex of top hit and compound **AV-2**, on both the targets (hAChE and hBACE-1), to assess the stability of docked poses. The MD results indicated that the top hit interacted with PAS region of hAChE (Figure 5.8). The benzo-4-oxo-N-propyl-4H-pyrido[1,2-a]thieno[2,3-d]pyrimidine-2-carboxamide moiety of top hit showed hydrophobic interaction with Tyr72, Tyr124, Trp286, and Tyr341 of the PAS active site. While the carboxamide group of top hit was also interacting with the Asp74 of PAS through charged interaction.

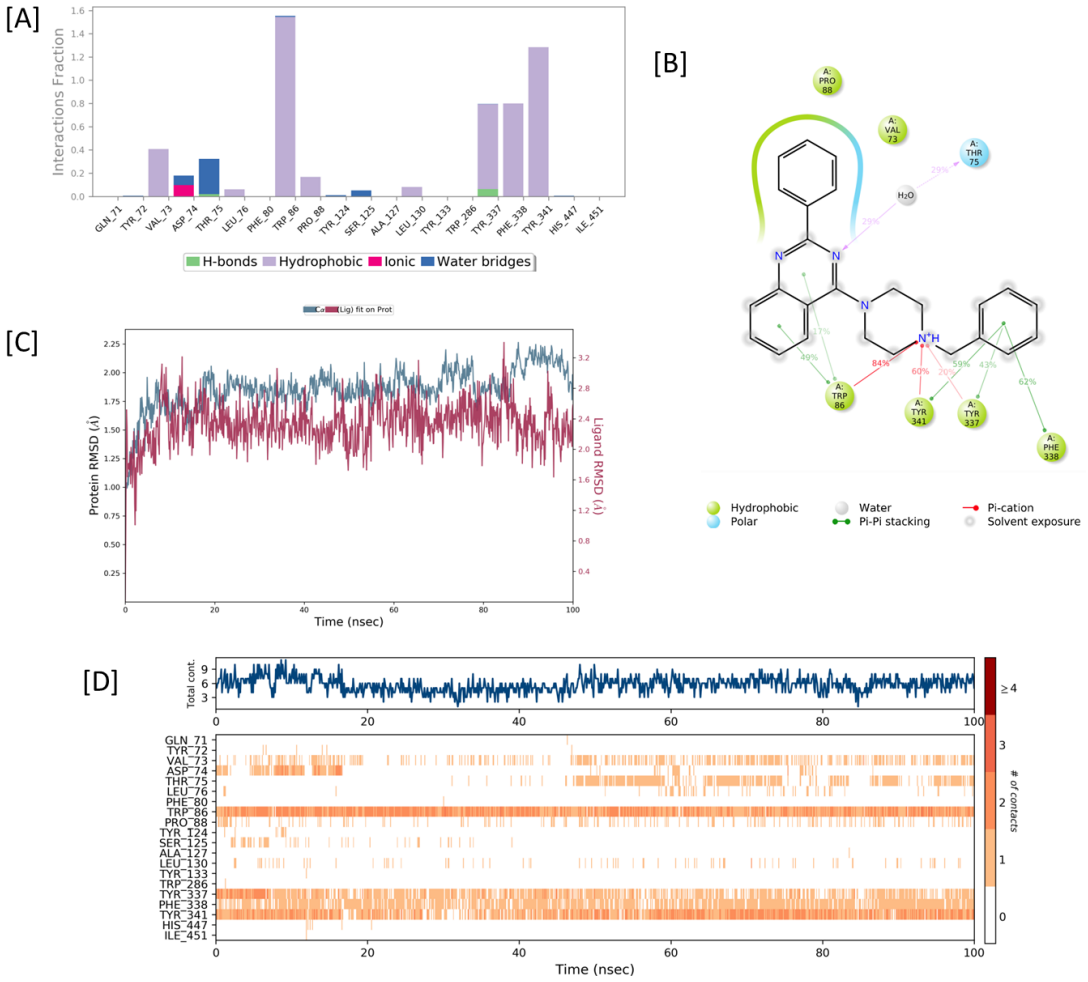

Figure 5.9. MD simulation analysis of **AV-2**-hAChE (4EY7) docked ligand-protein complex. [A] Histogram indicating ligand interaction fractions with different amino acid residues of active sites; [B] 2D interaction diagram showing percentage interactions different amino acid residues of active sites; [C] RMSD graph of ligand-protein (**AV-2**-

hAChE); [D] Timeline depiction protein-ligand interactions with their respective active amino acid residues at each time frame.

Similarly, the benzyl ring of compound **AV-2** showed π-π stacked interaction with Tyr341 of the PAS region while the quinazoline moiety showed hydrophobic interaction with Trp86 of the anionic subunit subsite (Figure 5.9).

The MD results of top hit and **AV-2** complexed with the hBACE-1 indicated stable ligand-protein complex throughout the run. The oxo group present on the top hit was found to be interacting with the Asp32 via water bridge interaction (Figure 5.10). The nitrogen atom of the piperazine moiety present on the compound **AV-2** was found to be interacting with the Asp32 and Asp228 (catalytic aspartate dyad residues) via electrostatic charged and H-bond interaction (Figure 5.11). Thus, findings of docking and MD simulations support our theory that designed series of compounds may enhance their inhibitory profile against both these targets.

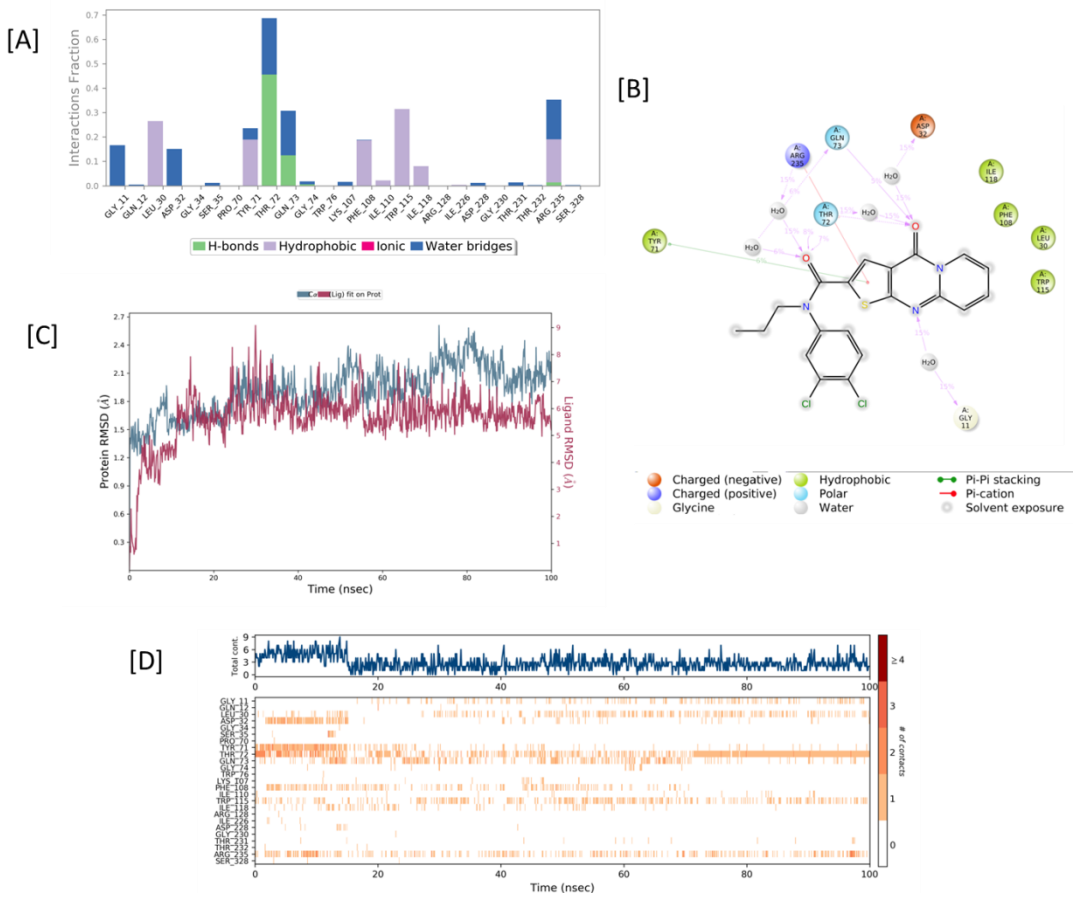

Figure 5.10. Molecular dynamics studies of ZINC000015441499-hBACE-1 (2ZJM) docked complex. [A] Histogram showing interaction fractions with active amino acid residues; [B] Graphical representation showing percentage interactions with active site residues; [C] RMSD graph of ligand-protein (ZINC000015441499-hBACE-1); [D] Timeline representation showing interaction with all the amino acid residues at each time frame.

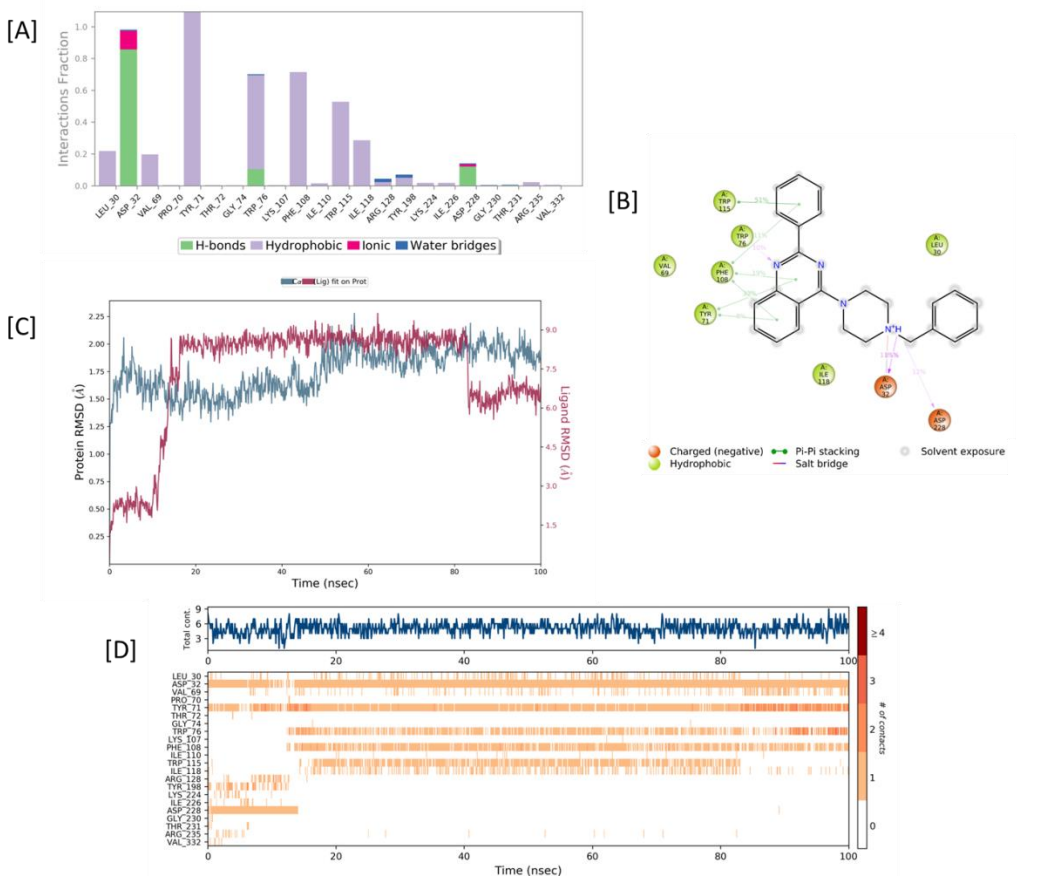

Figure 5.11. MD simulation analysis of **AV-2**-hBACE-1 (2ZJM) docked ligand-protein complex. [A] Histogram indicating ligand interaction fractions with different amino acid residues of active sites; [B] 2D interaction diagram showing percentage interactions different amino acid residues of active sites; [C] RMSD graph of ligand-protein (**AV-2**-hBACE-1); [D] Timeline depiction protein-ligand interactions with their respective active amino acid residues at each time frame.

The MD simulations of the identified hit (**ZINC000015441499**) and compound **AV-2** were analysed and compared with the identified hit (**SEW06622**) from our previous study was summarized and presented in Table 5.3 which demonstrated that identified hit (**ZINC000015441499**) showed better interaction fractions with different active regions as compared to the previously identified hit (**SEW06622**).

Table 5.3. Molecular dynamics simulation analysis of identified hits and compound **AV-2**

S. No.	Compound	hAChE interaction fractions (IF)					hBACE-1 interactions fractions (IF)
		PAS	**CAS**	**Anionic subunit subsite**	**Acyl binding pocket**	**Oxyanion hole**	**Aspartate dyad**
1.	**ZINC000001544149 9**	Tyr72^{w}: 0.56 Asp74^{w}: 0.59 Tyr124^{w,h}:0.11 Trp286^{hy}: 0.61 Tyr341^{w,hy}:1.23	--	Ph338^{w}: 0.51	Phe295^{w}:062	--	Asp32^{w}: 0.15
2.	**SEW06622**	Tyr72^{hy}: 0.32 Asp74^{w}: 0.12 Tyr124^{h}:1.12 Trp286^{hy}: 0.72 Tyr341^{hy}:0.89	--	Trp86^{w,hy}:0.32	--	--	Asp32^{i}: 0.07
3.	**AV-2**	Asp74^{i,w}: 0.22 Tyr341^{hy}: 1.23	--	Trp86^{hy} : 1.56 Phe338^{hy}: 0.81	--	--	Asp32^{hy,i}: 1.06 Asp228^{hy,i}: 0.21

^{w} water bridge; ^{h} H-bonding; ^{hy} hydrophobic; ^{i} ionic

5.1.1.6. Density Functional Theory (DFT) studies

Further, electrostatic properties of the compound **AV-2** were estimated using density functional theory (DFT) by Jaguar module of the Schrödinger Maestro 2018_1. The energy gap between the highest occupied molecular orbitals (HOMO) and lowest unoccupied molecular orbitals (LUMO) is useful in predicting the reactivity and kinetic stability of the compound where high energy gap represents stability and vice versa. The results suggested that a low energy gap i.e., 0.1732 kcal/mol between HOMO and LUMO possessed by the compound **AV-2** revealed its reactivity against both hAChE and hBACE-1 enzymes. The frontier molecular orbitals (FMO) including both HOMO and LUMO of compound **AV-2** are represented in Figure 5.12. The electrophilic and

nucleophilic properties of the compound **AV-2** were predicted by generating electrostatic potential on the molecular structure. The red colour refers to the favourable site where the probability of an electrophilic attack is more while the blue colour indicates the region where the chances of nucleophilic attack are high. The electrostatic potential of compound **AV-2** was found to be -11.52 kcal/mol and represented in Figure 5.12.

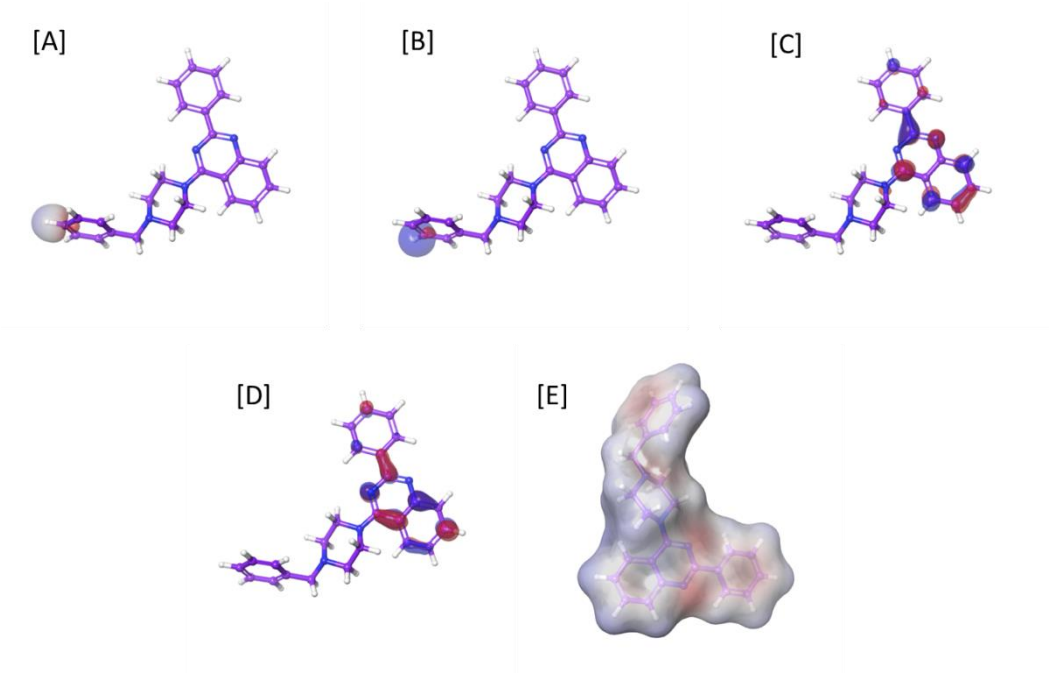

Figure 5.12. HOMO-LUMO orbital density and molecular electrostatic potential (MEP) surface of the compound **AV-2**; A & B) HOMO and HOMO-1 orbital density of compound **AV-2**; C & D) LUMO and LUMO+1 orbital density of compound **AV-2**; E) molecular electrostatic potential (MEP) surface of the compound **AV-2**.

The Fukui function of compound **AV-2** indicated that the probability of electrophilic attack at the –N atom of benzylpiperazine is favourable while the quinazoline and phenyl are favourable for both nucleophilic and electrophilic attack. Both Fukui f^+ and f^- structures of compound **AV-2** are shown in Figure 5.13.

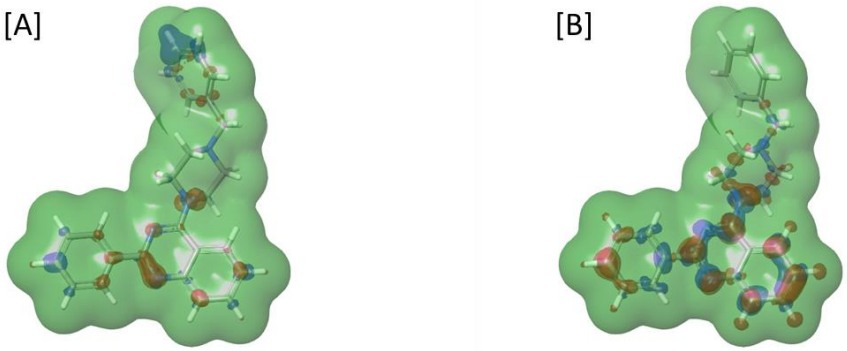

Figure 5.13. Graphical representation of electrophilic fukui function + ve *f* (r) left and nucleophilic fukui function – ve *f* (r) right of compound **AV-2**.

The pKa of all the nitrogen atoms present in the representative compound **AV-2** were also determined in which the pKa of nitrogen of piperazine which is attached to the benzylic portion of **AV-2** found to be 3.9 which indicated that it gets easily protonated at physiological pH 7.4 and provides favourable interactions with catalytic dyad of hBACE-1.

5.1.1.7. QikProp analysis

Additionally, drug-likeliness is a crucial need for the drug candidate. As neurotherapeutic drugs need to cross the BBB to perform their desired action [Tripathi et al. 2019]. Therefore, several physiochemical parameters like Lipinski's rule of five including mol MW, QPlog Po/w, donorHB, accptHB, and the other expected parameters like SASA, QPlogBB, QPlogPo/w, and Caco-2 cell permeability (PPCaco) of compound **AV-2** and standard donepezil were characterized using computer-aided prediction through QikProp module of Schrödinger Maestro 2018_1. The results indicated that the compound **AV-2** pass all the *in-silico* likeliness characteristics and was found comparable with the standard donepezil (Table 5.4).

Table 5.4. QikProp analysis of compound **AV-2**

Compound	Mol_ Wt[a]	Donor HB[b]	Acceptor HB[c]	SASA[d]	QplogBB[e]	Qplogo/w[f]	Rule of Five
Donepezil	393.61	1	7.1	759.67	0.14	4.25	Yes
AV-2	380.20	0	3.0	789.48	0.78	6.474	Yes

[a]Mol_MW- Molecular weight of the molecule (130 to 725).

[b]Donor HB- number of hydrogen bonds (0.0 to 6.0).

[c]Acceptor HB- number of hydrogen bonds (2.0 to 20.0).

[d]SASA- total solvent accessible surface area (SASA) in square angstroms using a probe with 1.4 A radius (300 to1000).

[e]QPlogBB- predicted brain/blood partition coefficient (-3.0 to 1.2).

[f]QPlogPo/w- this gives the predicted octanol/water partition coefficient (-2.0 to 6.5).

5.1.2. Chemistry

5.1.2.1. Synthesis of Series I (AV-1 to AV-21)

Following the series of designed compounds (**AV-1** to **AV-21)** were synthesized and characterized. The desired intermediates (**9c-15c**) were synthesized by treating 2-aminobenzamide (**1a**) with various substituted aromatic aldehydes (**2b-8b**) via a molecular iodine-catalysed oxidative coupling reaction in methanol at 80°C for 4-6 h. The formation of intermediates (**9c-15c)** was confirmed by ^{1}H NMR and ^{13}C NMR spectra. The ^{1}H NMR spectra displayed the characteristic singlet peak of amide proton (-NH) in the range of 13-10 ppm. The intermediate compounds (**9c-15c**) underwent chlorination reaction in the presence of $SOCl_2$ with a catalytic amount of N, N-dimethylformamide (DMF) in dry dichloromethane (DCM) at 40°C for 5-6 h. The presence of Cl-C=N and N=C signals in ^{13}C NMR in the range of 160-150 ppm value confirmed the formation of secondary intermediates (**16d-22d)**. Finally the secondary intermediates (**16d-22d**) were treated with substituted piperazines (1-Benzhydrylpiperazine, 1-Benzylpiperazine, and 1-(4-nitrophenyl)piperazine) in the presence of K_2CO_3 in dry DMF at 80 °C for 4 h yielded

targeted compounds (**AV-1** to **AV-21**). The structure of the final compounds were confirmed by the FT-IR spectra which showed the appearance of a characteristic stretching band of C-N (piperazine linked) in the range of 1350-1000 cm^{-1}. The ^{1}H NMR spectra of the final compounds showed the appearance of eight proton signals of piperazine ring in the range of 4-2 ppm. The piperazine moiety of all the targeted had two wider triplet peaks for both $–NCH_2$ due to the interconversion of axial and equatorial hydrogens in the chair and boat conformations of piperazine. The ^{13}C NMR spectra of the final compounds also revealed the presence of piperazine ring carbons between the ranges of 50-40 ppm. The mass spectrometry (MS) was utilized to confirm the molecular weights of all synthesized derivatives which showed the presence of molecular ion peak of the final compounds. The % purity of all the synthesized compounds was determined by HPLC which confirmed the purity ≥ 95%.

5.1.2.2. Characterization of the intermediates (9c to 15c)

5.1.2.2.1. 2-Phenylquinazolin-4(3H)-one (9c)

Yield: 86%; MW: 222.24; R_f = 0.52 (MeOH:DCM, 2:98 v/v); ^{1}H NMR (500 MHz, $\delta_{H,}$ $CDCl_3$): 11.556 (s, 1H), 8.287 (d, J = 8 Hz, 1H), 8.245-8.226 (m, 2H), 7.856-7.796 (m, 2H), 7.577(dd, *J* = 2, 1.5 Hz, 3H), 7.513 (ddd, *J* = 1.5, 1.5, 1 Hz, 1H). ^{13}C NMR (125 MHz, $\delta_{C,}$ $CDCl_3$): 163.86, 151.73, 149.51, 134.97, 132.81, 131.71, 129.10, 128.63, 128.03, 127.37, 126.94, 126.86, 126.40, 120.82.

5.1.2.2.2. 2-(4-Hydroxyphenyl)quinazolin-4(3H)-one (10c)

Yield: 89%; MW: 238.24; R_f = 0.36 (MeOH:DCM, 2:98 v/v); ^{1}H NMR (500 MHz, $\delta_{H,}$ DMSO-d_6): 12.33 (s, 1H), 10.19 (s, 1H), 8.15 – 8.07 (m, 4H), 7.83 – 7.78 (m, 1H), 7.68 (d, *J* = 8.0 Hz, 1H), 7.50 – 7.44 (m, 1H), 6.90 (d, *J* = 8.8 Hz, 2H). ^{13}C NMR (125 MHz,

$\delta_{C,}$ DMSO-d_6): 162.84, 161.03, 152.66, 149.43, 134.98, 130.06, 127.56, 126.40, 126.29, 123.66, 121.02, 115.83.

5.1.2.2.3. 2-(2,3-Dimethoxyphenyl)quinazolin-4(3H)-one (11c)

Yield: 89%; MW: 282.29; R_f = 0.58 (MeOH:DCM, 2:98 v/v); ^{1}H NMR (500 MHz, $\delta_{H,}$ DMSO-d_6): 12.22 (s, 1H), 8.17 (dd, *J* = 7.9, 1.8 Hz, 1H), 7.85 (ddd, *J* = 8.5, 7.1, 1.6 Hz, 1H), 7.71 (dd, *J* = 8.2, 0.8 Hz, 1H), 7.57 – 7.53 (m, 1H), 7.27 – 7.22 (m, 3H), 3.89 (s, 3H), 3.77 (s, 3H). ^{13}C NMR (125 MHz, $\delta_{C,}$ DMSO-d_6): 161.78, 152.91, 152.56, 149.28, 147.22, 134.97, 127.91, 127.18, 126.28, 124.58, 121.86, 115.56, 61.44, 56.48.

5.1.2.2.4. 2-(3,4,5-Trimethoxyphenyl)quinazolin-4(3H)-one (12c)

Yield: 91%; MW: 312.32; R_f = 0.52 (MeOH:DCM, 2:98 v/v); ^{1}H NMR (500 MHz, $\delta_{H,}$ DMSO-d_6): 8.16 (dd, *J* = 7.9, 1.7 Hz, 1H), 7.84 (ddd, *J* = 8.7, 7.0, 1.8 Hz, 1H), 7.76 (d, *J* = 7.6 Hz, 1H), 7.57 (s, 2H), 7.52 (t, *J* = 7.2 Hz, 1H), 3.91 (s, 6H), 3.75 (s, 3H). ^{13}C NMR (125 MHz, $\delta_{C,}$ DMSO-d_6): 162.82, 152.91, 149.03, 140.69, 135.12, 128.08, 127.85, 126.98, 126.33, 121.26, 105.65, 104.83, 60.63, 56.59.

5.1.2.2.5. 2-(p-Tolyl)quinazolin-4(3H)-one (13c)

Yield: 90%; MW: 236.27; R_f = 0.61 (MeOH:DCM, 2:98 v/v); ^{1}H NMR (500 MHz, $\delta_{H,}$ DMSO-d_6): 12.48 (s, 1H), 8.15 (dd, *J* = 7.9, 1.0 Hz, 1H), 8.10 (d, *J* = 8.2 Hz, 2H), 7.85 – 7.81 (m, 1H), 7.73 (d, *J* = 7.8 Hz, 1H), 7.53 – 7.49 (m, 1H), 7.36 (d, *J* = 8.1 Hz, 2H), 2.39 (s, 3H). ^{13}C NMR (125 MHz, $\delta_{C,}$ DMSO-d_6): 162.75, 152.70, 149.29, 141.95, 135.07, 130.34, 129.68, 128.15, 127.88, 126.89, 126.31, 121.35, 21.46.

5.1.2.2.6. 2-(4-Nitrophenyl)quinazolin-4(3H)-one (14c)

Yield: 92%; MW: 267.24; R_f = 0.48 (MeOH:DCM, 2:98 v/v); ^{1}H NMR (500 MHz, $\delta_{H,}$ DMSO-d_6): 8.53 (s, 1H), 8.41 (d, *J* = 7.8 Hz, 2H), 8.26 (d, *J* = 8.3 Hz, 1H), 8.19 (d, *J* = 7.8 Hz, 1H), 7.89 (t, *J* = 7.8 Hz, 1H), 7.81 (d, *J* = 7.8 Hz, 1H), 7.74 (d, *J* = 8.3 Hz, 1H),

7.62 – 7.58 (m, 1H). ^{13}C NMR (125 MHz, $\delta_{C,}$ DMSO-d_6): 163.76, 149.78, 149.47, 147.68, 135.33, 134.07, 129.81, 128.48, 128.13, 127.87, 126.42, 124.14.

5.1.2.2.7. 2-(4-(Trifluoromethoxy)phenyl)quinazolin-4(3H)-one (15c)

Yield: 94%; MW: 306.24; R_f = 0.63 (MeOH:DCM, 2:98 v/v); ^{1}H NMR (500 MHz, $\delta_{H,}$ DMSO-d_6): 8.95 (s, 1H), 8.38 (d, *J* = 8.2 Hz, 2H), 8.18 (d, *J* = 7.8 Hz, 1H), 7.93 (d, *J* = 8.2 Hz, 1H), 7.87 (t, *J* = 7.6 Hz, 1H), 7.78 (d, *J* = 8.1 Hz, 1H), 7.71 (dd, *J* = 9.9, 5.3 Hz, 1H), 7.57 (t, *J* = 7.4 Hz, 1H). ^{13}C NMR (125 MHz, $\delta_{C,}$ DMSO-d_6): 162.62, 151.69, 148.82, 137.04, 135.21, 129.20, 128.06, 127.59, 127.46, 126.37, 125.98, 125.95, 121.65.

5.1.2.3. Characterization of the intermediates (16d to 22d)

5.1.2.3.1. 4-Chloro-2-phenylquinazoline (16d)

Yield: 93%; MW: 240.69; R_f = 0.94 (MeOH:DCM, 2:98 v/v); ^{1}H NMR (500 MHz, $\delta_{H,}$ DMSO-d_6): 8.17 (dd, *J* = 12.9, 5.1 Hz, 3H), 7.92 – 7.86 (m, 2H), 7.68 – 7.63 (m, 1H), 7.59 (ddd, *J* = 7.4, 6.2, 3.6 Hz, 3H). ^{13}C NMR (125 MHz, $\delta_{C,}$ DMSO-d_6): 162.78, 162.23, 154.11, 135.47, 132.57, 129.33, 129.14, 128.77, 127.61, 126.54, 126.24, 121.12.

5.1.2.3.2. 4-(4-Chloroquinazolin-2-yl)phenol (17d)

Yield: 91%; MW: 256.68; R_f = 0.87 (MeOH:DCM, 2:98 v/v); ^{1}H NMR (500 MHz, $\delta_{H,}$ DMSO-d_6): 8.32 – 8.28 (m, 2H), 8.18 (dd, *J* = 7.9, 1.2 Hz, 1H), 7.90 – 7.86 (m, 1H), 7.81 (d, *J* = 7.8 Hz, 1H), 7.58 (d, *J* = 7.9 Hz, 3H). ^{13}C NMR (125 MHz, $\delta_{C,}$ DMSO-d_6): 162.44, 152.27, 151.05, 147.92, 135.33, 131.62, 130.87, 127.54, 127.19, 126.44, 121.34, 119.43.

5.1.2.3.3. 4-Chloro-2-(2,3-dimethoxyphenyl)quinazoline (18d)

Yield: 91%; MW: 300.74; R_f = 0.87 (MeOH:DCM, 2:98 v/v); ^{1}H NMR (500 MHz, $\delta_{H,}$ DMSO-d_6): 8.20 (d, *J* = 7.9 Hz, 1H), 7.92 (t, *J* = 7.7 Hz, 1H), 7.78 (d, *J* = 8.1 Hz, 1H), 7.63 (t, *J* = 7.5 Hz, 1H), 7.34 – 7.31 (m, 1H), 7.25 (d, *J* = 4.8 Hz, 2H), 3.90 (s, 3H), 3.79

(s, 3H). ^{13}C NMR (125 MHz, $\delta_{C,}$ DMSO-d_6): 161.31, 153.69, 152.3, 147.18, 135.56, 127.94, 126.61, 125.73, 124.71, 121.96, 121.14, 116.40, 61.64, 56.56.

5.1.2.3.4. 4-Chloro-2-(3,4,5-trimethoxyphenyl)quinazoline (19d)

Yield: 63%; MW: 331; R_f = 0.82 (MeOH:DCM, 2:98 v/v); ^{1}H NMR (500 MHz, $\delta_{H,}$ $CDCl_3$): 8.89 (s, 2H), 7.41 (s, 2H), 7.36 (s, 2H), 4.09 (s, 9H).^{13}C NMR (125 MHz, $\delta_{C,}$ $CDCl_3$): 159.08, 156.80, 152.49, 151.48, 149.06, 119.58, 106.90, 102.69, 56.63, 56.45.

5.1.2.3.5. 4-Chloro-2-(p-tolyl)quinazoline (20d)

Yield: 70%; MW: 254.71; R_f = 0.89 (MeOH:DCM, 2:98 v/v); ^{1}H NMR (500 MHz, $\delta_{H,}$ DMSO-d_6): 8.18 (dd, *J* = 8.0, 1.5 Hz, 1H), 8.08 (dd, *J* = 6.1, 2.1 Hz, 2H), 7.92 (ddd, *J* = 10.8, 9.8, 4.7 Hz, 2H), 7.62 – 7.58 (m, 1H), 7.42 (d, *J* = 8.4 Hz, 2H), 2.42 (s, 3H). ^{13}C NMR (125 MHz, $\delta_{C,}$ DMSO-d_6): 162.78, 161.95, 154.72, 143.37, 135.65, 129.74, 129.03, 127.73, 126.63, 125.21, 120.83, 21.58.

5.1.2.3.6. 4-Chloro-2-(4-nitrophenyl)quinazoline (21d)

Yield: 74%; MW: 285.68; R_f = 0.76 (MeOH:DCM, 2:98 v/v); ^{1}H NMR (500 MHz, $\delta_{H,}$ DMSO-d_6): 8.44 - 8.39 (m, 2H), 8.27 (dd, *J* = 2.9, 1.4 Hz, 1H), 7.93 – 7.89 (m, 1H), 7.76 (d, *J* = 5.7 Hz, 1H), 7.47 (d, *J* = 3.9 Hz, 3H). ^{13}C NMR (125 MHz, $\delta_{C,}$ DMSO-d_6): 162.66, 151.85, 150.05, 145.29, 139.23, 130.26, 129.79, 125.45, 121.91, 120.35, 119.44, 117.34.

5.1.2.3.7. 4-Chloro-2-(4-(trifluoromethoxy)phenyl)quinazoline (22d)

Yield: 66%; MW: 324.68; R_f = 0.86 (MeOH:DCM, 2:98 v/v); ^{1}H NMR (500 MHz, $\delta_{H,}$ DMSO-d_6): 8.17 – 8.15 (m, 1H), 7.92 – 7.80 (m, 5H), 7.55 (ddd, *J* = 8.1, 6.3, 2.0 Hz, 1H), 7.16 (d, *J* = 8.5 Hz, 1H). ^{13}C NMR (125 MHz, $\delta_{C,}$ DMSO-d_6): 162.25, 152.73, 148.97, 135.44, 127.22, 126.53, 125.85, 122.47, 120.74, 111.86, 111.67.

5.1.2.4. Characterization of the targeted compounds (AV-1 to AV-21)

5.1.2.4.1. 4-(4-Benzhydrylpiperazin-1-yl)-2-phenylquinazoline (AV-1)

Yield: 89%; mp: 162-164 ^{o}C; R_f = 0.52 (MeOH:DCM, 2:98 v/v); IR (Alpha ATR, υ cm^{-1}): 1070.53 (C-N); ^{1}H NMR (500 MHz, $\delta_{H,}$ $CDCl_3$): 8.56 (dd, *J* = 6.0, 2.1 Hz, 1H), 7.99 (s, 1H), 7.97 (d, *J* = 8.4 Hz, 1H), 7.88 (dd, *J* = 8.4, 1.2 Hz, 1H), 7.71 (ddd, *J* = 8.4, 6.8, 1.5 Hz, 1H), 7.51 - 7.48 (m, 6H), 7.39 - 7.36 (m, 1H), 7.33 (dd, *J* = 10.3, 4.9 Hz, 4H), 7.23 (ddd, *J* = 6.7, 4.2, 1.6 Hz, 3H), 3.92 (t, *J* = 5.5 Hz, 4H), 2.68 (t, *J* = 5.1 Hz, 4H). ^{13}C NMR (125 MHz, $\delta_{C,}$ $CDCl_3$): 164.75, 162.55, 159.45, 152.86, 142.47, 138.70, 130.11, 128.63, 128.42, 128.30, 127.96, 127.13, 115.42, 51.97, 49.97. ESI-MS (m/z): 457.236 $[M + H]^+$. HPLC purity: 98.83%, retention time: 1.772 min.

5.1.2.4.2. 4-(4-Benzylpiperazin-1-yl)-2-phenylquinazoline (AV-2)

Yield: 84%; mp: 162-164 ^{o}C; R_f = 0.57 (MeOH:DCM, 2:98 v/v); IR (Alpha ATR, υ cm^{-1}): 1055 (C-N); ^{1}H NMR (500 MHz, $\delta_{H,}$ $CDCl_3$): 8.58 – 8.56 (m, 2H), 7.99 (dd, *J* = 8.5, 0.9 Hz, 1H), 7.91 (dd, *J* = 8.4, 1.4 Hz, 1H), 7.74 (ddd, *J* = 8.3, 6.8, 1.5 Hz, 1H), 7.52 – 7.48 (m, 3H), 7.44 – 7.36 (m, 6H), 3.92 (t, *J* = 5.4 Hz, 4H), 3.64 (s, 2H), 2.73 (t, *J* = 5.0 Hz, 4H). ^{13}C NMR (125 MHz, $\delta_{C,}$ $CDCl_3$): 164.80, 159.47, 152.87, 138.69, 137.83, 132.34, 130.14, 129.23, 128.99, 128.43, 128.36, 128.33, 127.27, 124.93, 124.78, 115.41, 63.11, 53.03, 49.77. ESI-MS (m/z): 381.202 $[M + H]^+$. HPLC purity: 99.89%, retention time: 1.826 min.

5.1.2.4.3. 4-(4-(4-Nitrophenyl)piperazin-1-yl)-2-phenylquinazoline (AV-3)

Yield: 81%; mp: 162-164 ^{o}C; R_f = 0.46 (MeOH:DCM, 2:98 v/v); IR (Alpha ATR, υ cm^{-1}): 998.75(C-N); ^{1}H NMR (500 MHz, $\delta_{H,}$ $CDCl_3$): 8.60 – 8.58 (m, 2H), 8.18 (d, *J* = 9.4 Hz, 2H), 8.04 (dd, *J* = 8.4, 0.5 Hz, 1H), 7.98 – 7.96 (m, 1H), 7.81 – 7.78 (m, 1H), 7.51 (ddd, *J* = 9.6, 8.0, 5.1 Hz, 4H), 6.88 (d, *J* = 9.4 Hz, 2H), 4.08 (t, *J* = 5.3 Hz, 4H), 3.72 (t, *J*

= 5.1 Hz, 4H).^{13}C NMR (125 MHz, $\delta_{C,}$ $CDCl_3$): 164.57, 159.41, 154.59, 152.89, 138.85, 138.40, 132.71, 130.38, 128.42, 126.01, 125.28, 124.54, 115.33, 112.58, 48.99, 46.66. ESI-MS (m/z): 412.174 $[M + H]^+$. HPLC purity: 97.45%, retention time: 1.694 min.

5.1.2.4.4. 4-(4-(4-Benzhydrylpiperazin-1-yl)quinazolin-2-yl)phenol (AV-4)

Yield: 76%; mp: 162-164 ^oC; R_f = 0.48 (MeOH:DCM, 2:98 v/v); IR (Alpha ATR, υ cm^{-1}): 3365 (-OH), 1028 (C-N); ^{1}H NMR (500 MHz, $\delta_{H,}$ $CDCl_3$): 8.19 – 8.15 (m, 2H), 8.03 (s, 1H), 7.95 (dd, *J* = 8.5, 1.4 Hz, 1H), 7.86 (dd, *J* = 8.3, 1.5 Hz, 1H), 7.70 (ddd, *J* = 8.4, 6.9, 1.4 Hz, 1H), 7.51 – 7.49 (m, 4H), 7.44 – 7.42 (m, 1H), 7.34 (ddd, *J* = 9.9, 5.4, 1.6 Hz, 5H), 7.24 (dt, *J* = 3.9, 1.6 Hz, 2H), 6.97 (d, *J* = 8.4 Hz, 1H), 4.35 (s, 1H), 3.89 (t, *J* = 5.4 Hz, 4H), 2.68 (t, *J* = 5.2 Hz, 4H).^{13}C NMR (125 MHz, $\delta_{C,}$ $CDCl_3$): 164.68, 159.16, 152.83, 150.98, 142.46, 132.30, 131.59, 128.64, 127.96, 127.15, 124.94, 124.42, 121.74, 115.22, 111.11, 110.61, 55.96, 51.98, 49.95. ESI-MS (m/z): 472.198 $[M + H]^+$. HPLC purity: 96.12%, retention time: 2.217 min.

5.1.2.4.5. 4-(4-(4-Benzylpiperazin-1-yl)quinazolin-2-yl)phenol (AV-5)

Yield: 79%; mp: 162-164 ^oC; R_f = 0.46 (MeOH:DCM, 2:98 v/v); IR (Alpha ATR, υ cm^{-1}): 3348 (-OH), 1062 (C-N); ^{1}H NMR (500 MHz, $\delta_{H,}$ $CDCl_3$): 8.21 – 8.17 (m, 3H), 7.96 (dd, *J* = 8.4, 1.1 Hz, 1H), 7.90 (dd, *J* = 8.4, 1.4 Hz, 1H), 7.72 (ddd, *J* = 8.4, 6.9, 1.5 Hz, 1H), 7.42 – 7.36 (m, 6H), 7.35 – 7.30 (m, 1H), 6.99 (d, *J* = 8.4 Hz, 1H), 3.98 (s, 2H), 3.89 (t, *J* = 5.1 Hz, 4H), 2.73 (t, *J* = 5.2 Hz, 4H). ^{13}C NMR (125 MHz, $\delta_{C,}$ $CDCl_3$): 164.77, 159.16, 152.87, 151.00, 148.77, 137.85, 132.32, 131.61, 129.23, 128.77, 128.36, 127.27, 124.93, 124.50, 121.74, 115.27, 111.14, 110.62, 63.11, 53.01, 49.79. ESI-MS (m/z): 397.199 $[M + H]^+$. HPLC purity: 97.56%, retention time: 2.237 min.

5.1.2.4.6. 4-(4-(4-(4-Nitrophenyl)piperazin-1-yl)quinazolin-2-yl)phenol (AV-6)

Yield: 78%; mp: 162-164 ^{o}C; R_f = 0.39 (MeOH:DCM, 2:98 v/v); IR (Alpha ATR, υ cm^{-1}): 3338 (-OH), 1084 (C-N), 1249,1317(-NO_2); ^{1}H NMR (500 MHz, $\delta_{H,}$ $CDCl_3$): 8.30 (dd, *J* = 7.9, 1.6 Hz, 1H), 8.19 (dt, *J* = 4.7, 2.1 Hz, 4H), 8.01 (dd, *J* = 8.5, 1.1 Hz, 1H), 7.95 (dd, *J* = 8.3, 1.5 Hz, 1H), 7.84 – 7.82 (m, 1H), 7.80 – 7.76 (m, 1H), 7.48 (dddd, *J* = 17.8, 8.4, 6.7, 1.6 Hz, 1H), 7.01 (d, *J* = 8.5 Hz, 1H), 6.92 – 6.89 (m, 2H), 4.06 (t, *J* = 5 Hz, 4H), 3.73 (t, *J* = 5 Hz, 4H).^{13}C NMR (125 MHz, $\delta_{C,}$ $CDCl_3$): 164.77, 159.16, 152.87, 151.00, 148.77, 137.85, 132.32, 131.61, 129.23, 128.77, 128.36, 127.27, 124.93, 124.50, 121.74, 115.27, 111.14, 110.62, 63.11, 53.01, 49.79. ESI-MS (m/z): 428.160 $[M + H]^+$. HPLC purity: 98.245%, retention time: 2.551 min.

5.1.2.4.7. 4-(4-Benzhydrylpiperazin-1-yl)-2-(3,4-dimethoxyphenyl)quinazoline (AV-7)

Yield: 84%; mp: 162-164 ^{o}C; R_f = 0.59 (MeOH:DCM, 2:98 v/v); IR (Alpha ATR, υ cm^{-1}): 1294,1192 (Ph-O-CH_3), 1084 (C-N); ^{1}H NMR (500 MHz, $\delta_{H,}$ $CDCl_3$): 8.17 (dd, *J* = 9.5, 5.1 Hz, 2H), 7.96 – 7.94 (m, 1H), 7.86 (dd, *J* = 8.3, 1.5 Hz, 1H), 7.72 – 7.68 (m, 1H), 7.51 – 7.50 (m, 4H), 7.35 – 7.32 (m, 5H), 7.25 – 7.22 (m, 2H), 6.98 (d, *J* = 8.4 Hz, 1H), 4.35 (s, 1H), 4.05 (s, 3H), 3.97 (s, 3H), 3.89 (t, *J* = 5.5 Hz, 4H), 2.68 (t, *J* = 5.4 Hz, 4H). ^{13}C NMR (125 MHz, $\delta_{C,}$ $CDCl_3$): 164.68, 159.14, 152.82, 150.99, 148.77, 142.47, 132.30, 128.71, 128.64, 127.96, 127.15, 124.94, 124.42, 121.75, 115.22, 111.12, 110.61, 55.96, 51.98, 49.95, 30.94, 29.72. ESI-MS (m/z): 517.259 $[M + H]^+$. HPLC purity: 98.13%, retention time: 2.281 min.

5.1.2.4.8. 4-(4-Benzylpiperazin-1-yl)-2-(2,3-dimethoxyphenyl)quinazoline (AV-8)

Yield: 77%; mp: 162-164 ^{o}C; R_f = 0.55 (MeOH:DCM, 2:98 v/v); IR (Alpha ATR, υ cm^{-1}): 1276,1183 (Ph-O-CH3), 1055 (C-N); ^{1}H NMR (500 MHz, $\delta_{H,}$ $CDCl_3$): 8.45 (d, *J* = 8.6 Hz, 1H), 8.04 (s, 1H), 7.95 (d, *J* = 8.5 Hz, 1H), 7.88 (d, *J* = 8.3 Hz, 1H), 7.70 (t, *J* = 7.7

Hz, 1H), 7.39 – 7.34 (m, 6H), 6.93 (d, *J* = 8.6 Hz, 1H), 3.89 (t, *J* = 5 Hz, 4H), 3.64 (s, 2H), 2.98 (s, 3H), 2.91 (s, 3H), 2.72 (t, *J* = 5 Hz, 4H).^{13}C NMR (125 MHz, $\delta_{C,}$ $CDCl_3$): 164.83, 157.92, 153.09, 152.46, 142.12, 131.22, 129.26, 128.69, 128.34, 127.11, 124.53, 124.22, 111.35, 104.60, 64.78, 60.69, 55.81, 52.89, 49.18. ESI-MS (m/z): 441.228 [M + H]$^+$. HPLC purity: 98.24%, retention time: 2.176 min.

5.1.2.4.9. 2-(2,3-Dimethoxyphenyl)-4-(4-(4-nitrophenyl)piperazin-1-yl)quinazoline (AV-9)

Yield: 69%; mp: 162-164 ^{o}C; R_f = 0.47 (MeOH:DCM, 2:98 v/v); IR (Alpha ATR, υ cm^{-1}): 1262,1175 (Ph-O-CH3), 1062 (C-N), 1271,1324(-NO_2); ^{1}H NMR (500 MHz, $\delta_{H,}$ $CDCl_3$): 8.43 (d, *J* = 8.4 Hz, 1H), 8.01 (s, 1H), 7.97 (d, *J* = 8.1 Hz, 1H), 7.84 (d, *J* = 8 Hz, 1H), 7.74 (t, *J* = 7.3 Hz, 1H), 7.39 – 7.34 (m, 5H), 6.93 (d, *J* = 7.4 Hz, 1H), 3.87 (t, *J* = 5 Hz, 4H), 2.95 (s, 3H), 2.92 (s, 3H), 2.70 (t, *J* = 5 Hz, 4H).^{13}C NMR (125 MHz, $\delta_{C,}$ $CDCl_3$): 164.86, 157.89, 153.16, 152.49, 142.22, 131.44, 129.61, 128.97, 128.44, 127.26, 124.36, 124.36, 111.54, 104.06, 64.88, 60.97, 55.19, 49.82. ESI-MS (m/z): 472.197 [M + H]$^+$. HPLC purity: 97.66%, retention time: 2.138 min.

5.1.2.4.10. 4-(4-Benzhydrylpiperazin-1-yl)-2-(3,4,5-trimethoxyphenyl)quinazoline (AV-10)

Yield: 73%; mp: 162-164 ^{o}C; R_f = 0.62 (MeOH:DCM, 2:98 v/v); IR (Alpha ATR, υ cm^{-1}): 1252,1110 (Ph-O-CH3), 994 (C-N); ^{1}H NMR (500 MHz, $\delta_{H,}$ $CDCl_3$): 7.93 (d, *J* = 8.4 Hz, 1H), 7.83 (d, *J* = 6.8 Hz, 3H), 7.68 (t, *J* = 7.6 Hz, 1H), 7.47 (d, *J* = 7.7 Hz, 4H), 7.32 (dt, *J* = 15.1, 7.4 Hz, 5H), 7.20 (t, *J* = 7.3 Hz, 2H), 5.28 (s, 1H), 3.97 (s, 6H), 3.91 (s, 3H), 3.85 (d, *J* = 4.2 Hz, 4H), 2.65 (t, *J* = 4 Hz, 4H).^{13}C NMR (125 MHz, $\delta_{C,}$ $CDCl_3$): 164.78, 159.02, 153.18, 152.82, 142.48, 140.20, 132.43, 128.92, 128.71, 128.04, 127.24, 125.00,

124.76, 115.36, 105.69, 61.00, 56.27, 53.50, 52.05, 50.01. ESI-MS (m/z): 547.268 $[M + H]^+$. HPLC purity: 97.89%, retention time: 2.224 min.

5.1.2.4.11. 4-(4-Benzylpiperazin-1-yl)-2-(3,4,5-trimethoxyphenyl)quinazoline (AV-11)

Yield: 76%; mp: 162-164 ^oC; R_f = 0.57 (MeOH: DCM, 2:98 v/v); IR (Alpha ATR, υ cm^{-1}): 1225,1117 (Ph-O-CH3), 999 (C-N); ^1H NMR (500 MHz, $\delta_{H,}$ $CDCl_3$): 7.98 (dd, *J* = 8.4, 0.8 Hz, 1H), 7.92 – 7.89 (m, 3H), 7.75 – 7.72 (m, 1H), 7.43 – 7.36 (m, 5H), 7.32 (dt, *J* = 5.3, 2.4 Hz, 1H), 4.02 (s, 6H), 3.95 (s, 3H), 3.88 (t, *J* = 5.2 Hz, 4H), 3.65 (s, 2H), 2.74 (t, *J* = 5.1 Hz, 4H).^{13}C NMR (125 MHz, $\delta_{C,}$ $CDCl_3$): 164.85, 158.96, 153.11, 152.76, 140.11, 132.42, 129.25, 128.90, 128.38, 127.31, 124.93, 124.82, 115.35, 105.59, 65.87, 63.11, 60.96, 56.18, 52.98, 49.81. ESI-MS (m/z): 471.235 $[M + H]^+$. HPLC purity: 98.17%, retention time: 1.889 min.

5.1.2.4.12. 4-(4-(4-Nitrophenyl)piperazin-1-yl)-2-(3,4,5-trimethoxyphenyl)quinazoline (AV-12)

Yield: 71%; mp: 162-164 ^oC; R_f = 0.52 (MeOH: DCM, 2:98 v/v); IR (Alpha ATR, υ cm^{-1}): 1236,1110 (Ph-O-CH3), 1022 (C-N), 1486,1313 (-NO_2); ^1H NMR (500 MHz, $\delta_{H,}$ $CDCl_3$): 8.21 – 8.19 (m, 2H), 8.04 (dd, *J* = 8.5, 1.0 Hz, 1H), 7.97 (dd, *J* = 8.4, 1.4 Hz, 1H), 7.90 (s, 2H), 7.80 (ddd, *J* = 8.4, 6.9, 1.4 Hz, 1H), 7.49 (ddd, *J* = 8.4, 6.9, 1.5 Hz, 1H), 6.92 – 6.90 (m, 1H), 4.08 (t, *J* = 5.3 Hz, 4H), 4.04 (s, 6H), 3.95 (s, 3H), 3.76 (t, *J* = 5.2 Hz, 4H).^{13}C NMR (125 MHz, $\delta_{C,}$ $CDCl_3$): 164.60, 158.96, 154.56, 153.20, 140.40, 138.92, 133.83, 132.79, 129.18, 126.04, 125.29, 124.56, 115.22, 112.62, 105.72, 60.98, 56.27, 49.01, 46.69. ESI-MS (m/z): 502.207 $[M + H]^+$. HPLC purity: 96.44%, retention time: 1.887 min.

5.1.2.4.13. 4-(4-Benzhydrylpiperazin-1-yl)-2-(p-tolyl)quinazoline (AV-13)

Yield: 80%; mp: 162-164 ^{o}C; R_f = 0.61 (MeOH: DCM, 2:98 v/v); IR (Alpha ATR, υ cm^{-1}): 2874 (-CH_3), 986 (C-N); ^{1}H NMR (500 MHz, $\delta_{H,}$ $CDCl_3$): 7.97 (dd, *J* = 8.4, 0.9 Hz, 1H), 7.94 – 7.92 (m, 1H), 7.90 (d, *J* = 1.4 Hz, 1H), 7.73 (ddd, *J* = 8.3, 6.8, 1.5 Hz, 1H), 7.50 – 7.48 (m, 4H), 7.41 (ddd, *J* = 8.3, 6.9, 1.4 Hz, 1H), 7.32 (ddd, *J* = 8.1, 6.8, 3.4 Hz, 7H), 7.25 – 7.21 (m, 2H), 4.36 (s, 1H), 3.86 (t, *J* = 5.4 Hz, 4H), 2.66 (t, *J* = 5.0 Hz, 4H), 2.62 (s, 3H). ^{13}C NMR (125 MHz, $\delta_{C,}$ $CDCl_3$): 164.38, 162.65, 152.54, 142.39, 132.31, 131.15, 130.46, 128.92, 128.86, 128.63, 127.96, 127.14, 125.79, 124.89, 124.87, 114.78, 76.29, 52.03, 52.02, 21.45. ESI-MS (m/z): 471.252 $[M + H]^+$. HPLC purity: 97.58%, retention time: 1.918 min.

5.1.2.4.14. 4-(4-Benzylpiperazin-1-yl)-2-(p-tolyl)quinazoline (AV-14)

Yield: 68%; mp: 162-164 ^{o}C; R_f = 0.66 (MeOH: DCM, 2:98 v/v); IR (Alpha ATR, υ cm^{-1}): 2991 (-CH3), 993 (C-N); ^{1}H NMR (500 MHz, $\delta_{H,}$ $CDCl_3$): 7.99 (dd, *J* = 8.4, 1.1 Hz, 1H), 7.95 – 7.92 (m, 2H), 7.77 – 7.73 (m, 1H), 7.45 (ddd, *J* = 8.4, 6.9, 1.6 Hz, 1H), 7.39 (d, *J* = 2.7 Hz, 2H), 7.37 (s, 1H), 7.34 (ddd, *J* = 8.0, 5.0, 1.8 Hz, 3H), 7.31 (d, *J* = 2.6 Hz, 1H), 7.29 (d, *J* = 1.5 Hz, 1H), 3.86 (t, *J* = 4.9 Hz, 4H), 3.64 (s, 2H), 2.71 (t, *J* = 5.3 Hz, 4H), 2.63 (s, 3H). ^{13}C NMR (125 MHz, $\delta_{C,}$ $CDCl_3$): 164.41, 162.67, 152.56, 139.30, 137.79, 137.26, 132.33, 131.14, 130.44, 129.23, 128.94, 128.87, 128.35, 127.26, 125.89, 124.95, 124.86, 63.11, 53.10, 49.82, 21.43. ESI-MS (m/z): 395.224 $[M + H]^+$. HPLC purity: 98.47%, retention time: 2.056 min.

5.1.2.4.15. 4-(4-(4-Nitrophenyl)piperazin-1-yl)-2-(p-tolyl)quinazoline (AV-15)

Yield: 74%; mp: 162-164 ^{o}C; R_f = 0.53 (MeOH:DCM, 2:98 v/v); IR (Alpha ATR, υ cm^{-1}): 2982 (-CH3), 989 (C-N), 1513,1322 (-NO_2) ; ^{1}H NMR (500 MHz, $\delta_{H,}$ $CDCl_3$): 7.99 (dd, *J* = 8.4, 1.1 Hz, 1H), 7.95 – 7.92 (m, 2H), 7.75 (ddd, *J* = 8.5, 6.9, 1.5 Hz, 1H), 7.45

(ddd, *J* = 8.4, 6.9, 1.6 Hz, 1H), 7.41 (d, *J* = 2.1 Hz, 1H), 7.38 (t, *J* = 2.6 Hz, 2H), 7.37 (d, *J* = 1.9 Hz, 1H), 7.34 (ddd, *J* = 9.3, 4.5, 2.2 Hz, 2H), 7.31 (dd, *J* = 6.3, 3.7 Hz, 1H), 3.86 (t, *J* = 5 Hz, 4H), 2.71 (t, *J* = 5 Hz, 4H), 2.63 (s, 3H). ^{13}C NMR (125 MHz, $\delta_{C,}$ $CDCl_3$): 164.21, 162.76, 152.65, 138.35, 135.82, 134.62, 133.31, 133.14, 130.40, 129.16, 128.53, 128.25, 128.19, 127.89, 126.42, 124.81, 124.74, 52.10, 48.81, 20.41. ESI-MS (m/z): 426.189 $[M + H]^+$. HPLC purity: 96.61%, retention time: 2.119 min.

5.1.2.4.16. 4-(4-Benzhydrylpiperazin-1-yl)-2-(4-nitrophenyl)quinazoline (AV-16)

Yield: 69%; mp: 162-164 ^oC; R_f = 0.51 (MeOH:DCM, 2:98 v/v); IR (Alpha ATR, υ cm^{-1}): 1532,1393 ($-NO_2$), 977 (C-N); ^{1}H NMR (500 MHz, $\delta_{H,}$ $CDCl_3$): δ 8.72 (d, *J* = 8.7 Hz, 2H), 8.32 (d, *J* = 8.8 Hz, 2H), 7.99 (d, *J* = 8.4 Hz, 1H), 7.91 (d, *J* = 8.4 Hz, 1H), 7.76 (t, *J* = 7.6 Hz, 1H), 7.51 (d, *J* = 7.7 Hz, 4H), 7.44 (t, *J* = 7.5 Hz, 1H), 7.34 (t, *J* = 7.6 Hz, 4H), 7.25 (t, *J* = 7.4 Hz, 2H), 4.36 (s, 1H), 3.96 (t, *J* = 5.1 Hz, 4H), 2.69 (t, *J* = 5.4 Hz, 4H).^{13}C NMR (125 MHz, $\delta_{C,}$ $CDCl_3$): 164.64, 157.19, 152.61, 148.89, 144.71, 142.28, 132.73, 129.17, 128.69, 127.93, 127.24, 125.62, 125.03, 123.48, 115.48, 51.95, 49.92, 29.72. ESI-MS (m/z): 502.225 $[M + H]^+$. HPLC purity: 96.62%, retention time: 2.048 min.

5.1.2.4.17. 4-(4-Benzylpiperazin-1-yl)-2-(4-nitrophenyl)quinazoline (AV-17)

Yield: 65%; mp: 162-164 ^oC; R_f = 0.54 (MeOH:DCM, 2:98 v/v); IR (Alpha ATR, υ cm^{-1}): 1552,1341 ($-NO_2$), 948 (C-N); ^{1}H NMR (500 MHz, $\delta_{H,}$ $CDCl_3$): 8.73 (d, *J* = 8.8 Hz, 2H), 8.33 (d, *J* = 9.0 Hz, 2H), 8.00 (dd, *J* = 8.4, 1.3 Hz, 1H), 7.94 (dd, *J* = 8.4, 1.4 Hz, 1H), 7.78 (ddd, *J* = 8.4, 6.9, 1.5 Hz, 1H), 7.48 (ddd, *J* = 8.4, 6.9, 1.4 Hz, 1H), 7.42 – 7.39 (m, 3H), 7.38 – 7.37 (m, 1H), 7.33 (dt, *J* = 5.3, 2.2 Hz, 1H), 3.95 (t, *J* = 5.1 Hz, 4H), 3.65 (s, 2H), 2.74 (t, *J* = 5.5 Hz, 4H). ^{13}C NMR (125 MHz, $\delta_{C,}$ $CDCl_3$): 164.74, 157.22, 152.65, 148.89, 144.74, 137.70, 129.21, 129.17, 128.39, 127.34, 125.68, 125.03, 123.49,

115.52, 63.07, 52.98, 49.77. ESI-MS (m/z): 426.191 $[M + H]^+$. HPLC purity: 96.23%, retention time: 1.768 min.

5.1.2.4.18. 2-(4-Nitrophenyl)-4-(4-(4-nitrophenyl)piperazin-1-yl)quinazoline (AV-18)

Yield: 63%; mp: 162-164 ^oC; R_f = 0.41 (MeOH:DCM, 2:98 v/v); IR (Alpha ATR, υ cm^{-1}): 1546,1391 ($-NO_2$), 977 (C-N); ^1H NMR (500 MHz, $\delta_{H,}$ $CDCl_3$): 8.73 (d, J = 9.0 Hz, 2H), 8.33 (d, J = 9.0 Hz, 2H), 8.00 (d, J = 7.7 Hz, 1H), 7.94 (d, J = 7.6 Hz, 1H), 7.78 (ddd, J = 8.3, 7.0, 1.3 Hz, 1H), 7.48 (ddd, J = 8.2, 7.0, 1.2 Hz, 2H), 7.40 (s, 1H), 7.38 (s, 1H), 7.33 (s, 1H), 7.32 (s, 1H), 3.95 (t, *J* = 5 Hz, 4H), 3.65 (s, 2H), 2.74 (t, *J* = 5 Hz, 4H). ^{13}C NMR (125 MHz, $\delta_{C,}$ $CDCl_3$): 164.74, 157.22, 152.65, 148.89, 144.74, 137.70, 132.74, 129.21, 129.17, 128.39, 127.34, 125.68, 125.03, 123.49, 115.52, 63.07, 52.98, 49.77. ESI-MS (m/z): 457.163 $[M + H]^+$. HPLC purity: 96.12%, retention time: 1.822 min.

5.1.2.4.19. 4-(4-Benzhydrylpiperazin-1-yl)-2-(4-(trifluoromethoxy)phenyl)quinazoline (AV-19)

Yield: 76%; mp: 162-164 ^oC; R_f = 0.58 (MeOH:DCM, 2:98 v/v); IR (Alpha ATR, υ cm^{-1}): 1256, 1157 ($-O-CF_3$), 1001(C-N); ^1H NMR (500 MHz, $\delta_{H,}$ $CDCl_3$): 8.59 (d, *J* = 8.7 Hz, 2H), 7.96 (dd, *J* = 8.4, 1.3 Hz, 1H), 7.89 (dd, *J* = 8.4, 1.4 Hz, 1H), 7.73 (ddd, *J* = 8.3, 6.9, 1.5 Hz, 1H), 7.52 – 7.50 (m, 4H), 7.39 (ddd, *J* = 8.4, 6.8, 1.4 Hz, 1H), 7.35 – 7.31 (m, 6H), 7.25 – 7.22 (m, 2H), 4.35 (s, 1H), 3.92 (t, *J* = 5.0 Hz, 4H), 2.67 (t, *J* = 5.2 Hz, 4H).^{13}C NMR (125 MHz, $\delta_{C,}$ $CDCl_3$): 164.74, 158.21, 152.75, 142.41, 137.33, 132.47, 130.00, 128.94, 128.65, 128.56, 127.94, 127.84, 127.17, 124.98, 124.94, 120.47, 115.36, 76.33, 51.95, 49.96. ESI-MS (m/z): 541.220 $[M + H]^+$. HPLC purity: 99.14%, retention time: 2.140 min.

5.1.2.4.20. 4-(4-Benzylpiperazin-1-yl)-2-(4-(trifluoromethoxy)phenyl)quinazoline (AV-20)

Yield: 79%; mp: 162-164 ^{o}C; R_f = 0.52 (MeOH:DCM, 2:98 v/v); IR (Alpha ATR, υ cm^{-1}): 1253, 1158 (-O-CF_3), 1002 (C-N); ^{1}H NMR (500 MHz, $\delta_{H,}$ $CDCl_3$): 8.60 (d, *J* = 8.8 Hz, 2H), 7.97 (dd, *J* = 8.5, 1.3 Hz, 1H), 7.91 (dd, *J* = 8.4, 1.4 Hz, 1H), 7.74 (ddd, *J* = 8.4, 6.9, 1.5 Hz, 1H), 7.43 (ddd, *J* = 9.2, 5.4, 1.8 Hz, 2H), 7.40 – 7.39 (m, 2H), 7.37 (s, 1H), 7.36 (d, *J* = 1.8 Hz, 1H), 7.34 – 7.34 (m, 1H), 7.32 (t, *J* = 1.7 Hz, 1H), 3.91 (t, *J* = 5.0 Hz, 4H), 3.64 (s, 2H), 2.72 (t, *J* = 5.2 Hz, 4H). ^{13}C NMR (125 MHz, $\delta_{C,}$ $CDCl_3$): 164.74, 158.21, 152.75, 142.41, 137.33, 132.47, 130.00, 128.94, 128.65, 128.56, 127.94, 127.84, 127.17, 124.98, 124.94, 120.47, 115.36, 76.33, 51.95, 49.96. ESI-MS (m/z): 465.188 $[M + H]^+$. HPLC purity: 99.24%, retention time: 2.399 min.

5.1.2.4.21. 4-(4-(4-Nitrophenyl)piperazin-1-yl)-2-(4(trifluoromethoxy)phenyl)quinazoline (AV-21)

Yield: 66%; mp: 162-164 ^{o}C; R_f = 0.59 (MeOH:DCM, 2:98 v/v); IR (Alpha ATR, υ cm^{-1}): 1241, 1162 (-O-CF_3), 1006 (C-N), 1501, 1303 (-NO_2); ^{1}H NMR (500 MHz, $\delta_{H,}$ $CDCl_3$): 8.62 (d, *J* = 8.8 Hz, 2H), 8.20 (d, *J* = 9.3 Hz, 2H), 8.03 (dd, *J* = 8.4, 0.9 Hz, 1H), 7.98 (dd, *J* = 8.4, 1.4 Hz, 1H), 7.81 (ddd, *J* = 8.5, 6.9, 1.5 Hz, 1H), 7.51 (ddd, *J* = 8.3, 6.8, 1.4 Hz, 1H), 7.35 (d, *J* = 8.7 Hz, 2H), 6.91 (d, *J* = 9.4 Hz, 2H), 4.10 (t, *J* = 5 Hz, 4H), 3.74 (t, *J* = 5 Hz, 4H). ^{13}C NMR (125 MHz, $\delta_{C,}$ $CDCl_3$): 164.61, 158.19, 154.55, 152.79, 150.92, 138.93, 137.00, 132.89, 130.01, 129.28, 126.03, 125.53, 124.59, 120.55, 119.48, 115.28, 112.62, 48.99, 46.66. ESI-MS (m/z): 496.160 $[M + H]^+$. HPLC purity: 99.08%, retention time: 2.475 min.

5.1.2.5. Single crystal X-ray crystallography

The single crystal X-ray crystallography (SC-XRD) of the representative compound **AV-2** was performed after getting the single crystal structure of the compound *via* slow evaporation in ethanol. The SC-XRD data showed that the compound **AV-2** exists in the monoclinic orientation at 100 K (Figure 5.14), (**Table 5.5**).

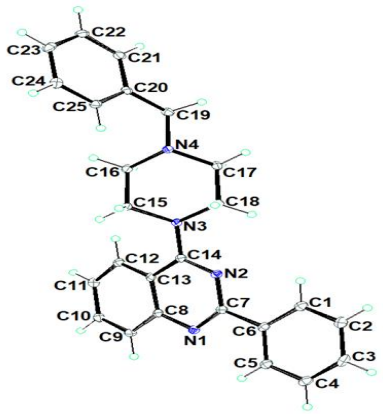

Figure 5.14. ORTEP diagram of compound **AV-2** obtained at 100 K.

Table 5.5. Crystallography and structure refinement data of compound **AV-2**

Crystal data and structure refinement for AV-2	
Identification code	**AV-2**
Empirical formula	$C_{25}H_{24}N_4$
Formula weight	380.48
Temperature/K	100(2)
Crystal system	Monoclinic
Space group	$P2_1/n$
a/Å	5.6679(8)
b/Å	13.149(2)
c/Å	25.971(4)
α/°	90
β/°	92.307(5)
γ/°	90
Volume/Å^3	1933.9(5)
Z	4
ρ_{calc}g/cm^3	1.307
μ/mm^{-1}	0.079
F(000)	808.0
Crystal size/mm^3	0.32 × 0.3 × 0.26
Radiation	MoKα (λ = 0.71073)

2Θ range for data collection/°	4.41 to 49.998
Index ranges	$-6 \leq h \leq 6, -15 \leq k \leq 15, -30 \leq l \leq 30$
Reflections collected	24952
Independent reflections	3405 [R_{int} = 0.0494, R_{sigma} = 0.0283]
Data/restraints/parameters	3405/0/262
Goodness-of-fit on F^2	1.175
Final R indexes [I>=2σ (I)]	R_1 = 0.0499, wR_2 = 0.1006
Final R indexes [all data]	R_1 = 0.0570, wR_2 = 0.1037
Largest diff. peak/hole / e $Å^{-3}$	0.18/-0.28
CCDC Number	2300901

5.1.3. Pharmacology

5.1.3.1. In-vitro studies

5.1.3.1.1. Cholinesterase inhibition assay (hAChE and hBChE)

The synthesized compounds (**AV-1** to **AV-21)** were assessed for their inhibitory potential, selectivity profile, and preliminary structural activity relationship (SAR) studies against hAChE and hBChE by Ellman colorimetry method with slight modifications using donepezil and rivastigmine as standard compounds [Ellman et al. 1961]. The 1-Benzhydrylpiperazine substituted compounds containing strong EWGs like para-substituted nitro and tri-floromethoxy (p-NO_2 and p-OCF_3) at the phenyl ring (**AV-16**: IC_{50} = 0.373 ± 0.023 µM; **AV-19**: IC_{50} = 0.248 ± 0.018 µM) and compounds containing weak ERGs (p-OH and p-methyl) (**AV-4**: IC_{50} = 0.489 ± 0.019 µM; **AV-13**: IC_{50} = 0.288 ± 0.011µM) showed hAChE inhibitory potential in sub-micromolar range. However, strong ERGs like 2,3-di-methoxy and 3,4,5-tri-methoxy (2,3-di-OCH_3 and 3.4.5-tri-OCH_3) weakened hAChE inhibitory potential (**AV-7**: IC_{50} = 0.550 ± 0.026 µM; **AV-10**: IC_{50} = 0.519 ± 0.027 µM).

In the 1-(4-nitrophenyl)piperazine containing compounds, the introduction of strong EWGs like p-NO_2 and p-OCF_3 (**AV-18**: IC_{50} = 0.558 ± 0.025 µM; **AV-21**: IC_{50} = 0.441 ± 0.019 µM) and ERGs such as p-OH and p-methyl at phenyl ring (**AV-6**: IC_{50} = 0.268 ± 0.017 µM; **AV-15**: IC_{50} = 0.296 ± 0.019 µM) demonstrated hAChE inhibitory potential in

sub-micromolar range. While strong ERGs (2,3-di-OCH_3 and 3.4.5-tri-OCH_3) weakened hAChE inhibitory potential (**AV-9**: IC_{50} = 0.826 ± 0.036 µM; **AV-12**: IC_{50} = 0.303 ± 0.018 µM).

Further, 1-Benzylpiperazine substituted compounds containing strong EWGs at phenyl ring (p-NO_2 and p-OCF_3) produced hAChE inhibitory potential in the sub-micromolar range (**AV-17**: IC_{50} = 0.425 ± 0.028 µM; **AV-20**: IC_{50} = 0.257 ± 0.022 µM). Similarly compounds containing ERGs (p-OH and p-methyl) also demonstrated hAChE inhibitory potential in the sub-micromolar range (**AV-5**: IC_{50} = 0.516 ± 0.027 µM; **AV-14**: IC_{50} = 0.527 ± 0.019 µM) while strong ERGs (2,3-di-OCH_3 and 3.4.5-tri-OCH_3) groups containing compounds (**AV-8**: IC_{50} = 0.277 ± 0.018 µM; **AV-11**: IC_{50} = 0.393 ± 0.018 µM) showed weakened hAChE inhibitory potential.

Overall, the results showed moderate to good inhibition of hAChE in the sub-micromolar range. The compound **AV-2** of the series showed comparable (3.94 fold less) hAChE inhibitions as compared to donepezil. However, the entire compound from the series produced hBChE inhibition ≥ 10 µM which indicated selectivity towards the hAChE over hBChE. **AV-2** being the most active compound of the series also corroborated our in *silico* (docking and dynamics) findings that it is interacting with AChE-PAS and CAS residues. The *in-vitro* data of all the compounds are represented in Table 5.6.

Table 5.6. Structures, inhibitory profile of designed compounds against ChE (hAChE and hBuChE) and hBACE-1 enzymes and their selectivity.

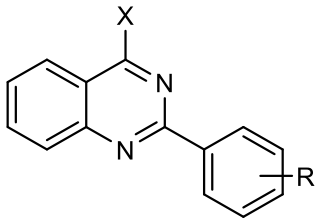

Comp. Code			IC_{50} (μM) ± SEM[a]		
	R	X	hAChE	hBChE	hBACE-1
AV-1	-H	1-Benzhydrylpiperazine	0.283 ± 0.016	>10	0.296 ± 0.075
AV-2	-H	1-Benzylpiperazine	0.193 ± 0.008	>10	0.254 ± 0.045
AV-3	-H	1-(4-nitrophenyl)piperazine	0.301 ± 0.018	>10	0.318 ± 0.060
AV-4	p-OH	1-Benzhydrylpiperazine	0.489 ± 0.019	>10	0.921 ± 0.073
AV-5	p-OH	1-Benzylpiperazine	0.516 ± 0.027	>10	1.044 ± 0.060
AV-6	p-OH	1-(4-nitrophenyl)piperazine	0.268 ± 0.017	>10	1.105 ± 0.082
AV-7	-2,3-di-MeO	1-Benzhydrylpiperazine	0.550 ± 0.026	>10	2.226 ± 0.066
AV-8	-2,3-di-MeO	1-Benzylpiperazine	0.277 ± 0.018	>10	2.671 ± 0.055
AV-9	-2,3-di-MeO	1-(4-nitrophenyl)piperazine	0.826 ± 0.036	>10	2.733 ± 0.052
AV-10	-3,4,5-tri-MeO	1-Benzhydrylpiperazine	0.519 ± 0.027	>10	0.882 ± 0.067
AV-11	-3,4,5-tri-MeO	1-Benzylpiperazine	0.393 ± 0.018	>10	0.663 ± 0.045
AV-12	-3,4,5-tri-MeO	1-(4-nitrophenyl)piperazine	0.303 ± 0.018	>10	0.961 ± 0.073
AV-13	p-methyl	1-Benzhydrylpiperazine	0.288 ± 0.011	>10	3.214 ± 0.085
AV-14	p-methyl	1-Benzylpiperazine	0.527 ± 0.019	>10	2.998 ± 0.092
AV-15	p-methyl	1-(4-nitrophenyl)piperazine	0.296 ± 0.019	>10	3.412 ± 0.091
AV-16	p-nitro	1-Benzhydrylpiperazine	0.373 ± 0.023	>10	3.398 ± 0.025
AV-17	p-nitro	1-Benzylpiperazine	0.425 ± 0.028	>10	3.301 ± 0.033

AV-18	p-nitro	1-(4-nitrophenyl)piperazine	0.558 ± 0.025	>10	3.598 ± 0.046
AV-19	p-O-CF_3	1-Benzhydrylpiperazine	0.248 ± 0.018	>10	0.481 ± 0.065
AV-20	p-O-CF_3	1-Benzylpiperazine	0.257 ± 0.022	>10	0.423 ± 0.071
AV-21	p-O-CF_3	1-(4-nitrophenyl)piperazine	0.441 ± 0.019	>10	0.523 ± 0.086
ZINC000001544149	-	-	0.514 ± 0.022	3.78 ± 0.037	1.05 ± 0.066
Donepezil	-	-	0.046 ± 0.005	1.3 ± 0.06	0.252 ± 0.098
Rivastigmine	-	-	nd	1.005 ± 0.02	nd

a - Results are expressed as the mean IC_{50} ± SEM (n = 3);

b - SI (selectivity index) = IC_{50} of hBChE/IC_{50} of hAChE;

5.1.3.1.2. Enzyme kinetics studies

The Lineweaver-Burk method was used to determine the enzyme inhibitory mechanism of compound **AV-2** on hAChE [Sharma et al. 2019c]. The Lineweaver-Burk plot and Michaelis-Menten graph results revealed that K_m remained constant and V_{max} decreased with increasing concentrations of substrate which demonstrated mixed type of inhibition for compound **AV-2**. The enzyme kinetics results indicated that compound **AV-2** inhibited both the enzyme-substrate complex and free enzyme non-competitively. It was observed that after extrapolation the intersection points on both the 1/V and 1/[S] axes were higher than zero, indicating that the compound **AV-2** was more frequently attached to the free enzyme rather than enzyme-substrate complexes. Further, Dixon plot was constructed between the slope of the Lineweaver-Burk plot and three different concentrations (0.03, 0.15, and 0.30 μM) of compound **AV-2**. The interaction point on the

x-axis revealed that compound **AV-2** has a dissociation constant K_d = 0.224 µM (Figure 5.15).

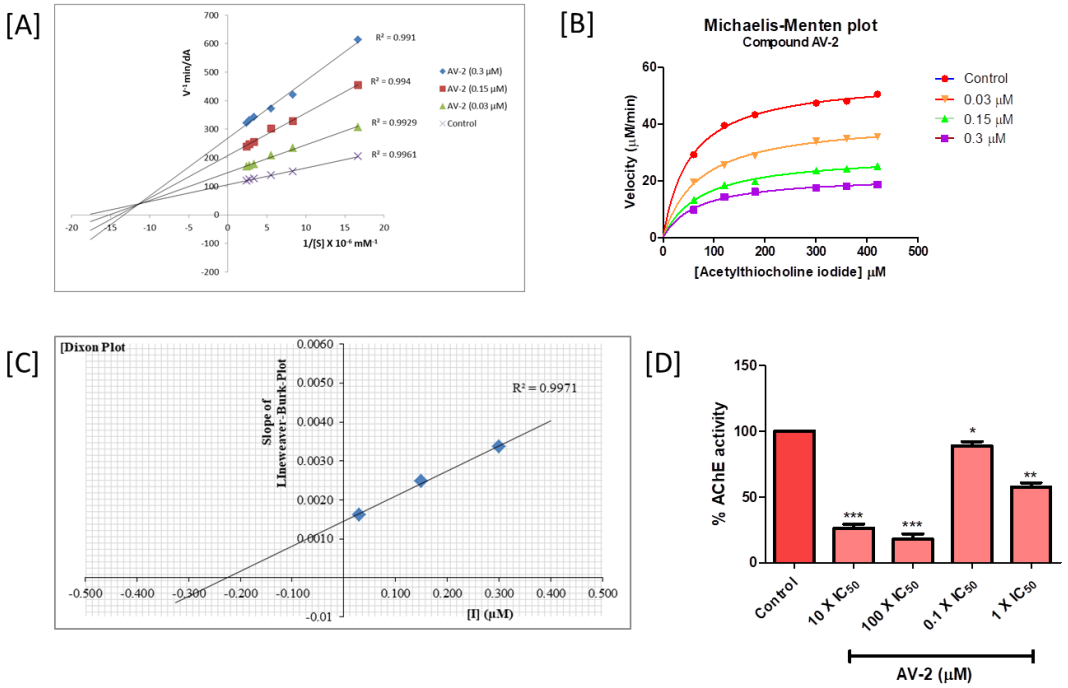

Figure 5.15. Enzyme kinetics studies of compound **AV-2** [A] Lineweaver-burk plot, [B] Michaelis-Menten plot, and [C] Dixon plot, [D] Enzyme reversibility study. Data are expressed as mean ± SEM (n=3). $^{*}p < 0.05$, $^{**}p < 0.01$, and $^{***}p < 0.001$ vs control.

5.1.3.1.3. Enzyme reversibility inhibition studies

The irreversibility nature of the drugs may cause several side effects and toxicity [Colovic et al. 2013] Therefore, the reversibility of the designed compounds is one of the important factors to be determined. The enzyme reversibility inhibition study was executed to identify the reversibility nature of the most promising compound **AV-2**. The result indicated that after incubation of the compound **AV-2** with hAChE at concentrations of 10 and 100 times more to that of the IC_{50} values reduced the activity to a minimum. Further, 100 times diluting it with ATCI substrate solution, the enzymatic activity was recovered by more than 60 % as shown in Figure 5.15. Thus, the compound **AV-2** can be regarded as a reversible inhibitor of AChE.

5.1.3.1.4. BACE-1 inhibition assay

To achieve significant multi-targeting inhibition, the current series of compounds was also designed to interact with the catalytic dyad residues (Asp32 and Asp228) of hBACE-1 in order to inhibit downstream regulation pathway. The hBACE-1 inhibitory potential of the designed derivatives (**AV-1** to **AV-22**) was determined on FRET-based BACE-1 fluorescence assay kit (Sigma Aldrich, Catalog No. CS0010) and compared with the standard drug donepezil Table 5.6.

The *in-vitro* hBACE-1 activity finding suggested that the introduction of various substituted phenyl rings (containing EWG and ERG) at the 2nd position of the quinazoline ring resulted in moderate hBACE-1 inhibitory activity. However, an unsubstituted phenyl ring increases the hBACE-1 inhibitory activity (**AV-1, AV-2** and **AV-3**). Amongst which the compound (**AV-2**) containing benzyl piperazine at the 4th position of the quinazoline ring showed most prominent hBACE-1 inhibitory activity (**AV-2**: IC_{50} = 0.254 ± 0.045 µM). It was assumed that the presence of benzyl piperazine at the 4th position may impart enough flexibility and optimum chain length to the structure resulting in better inhibition potential as compared to the 1-Benzhydrylpiperazine and 1-(4-nitrophenyl)piperazine containing compounds (**AV-1**: IC_{50} = 0.296 ± 0.075 µM; **AV-3**: IC_{50} = 0.318 ± 0.060 µM). Based on the *in-vitro* findings, compound **AV-2** was considered as MTDL and proceeds for further investigations.

The SAR studies were envisaged by modification at the 2nd and 4th positions of quinazoline moiety. The overall SAR (Figure 5.16) suggested that the substitution of various piperazines demonstrated the inhibition profile against hAChE and hBACE-1 as per following the trend 1-(4-nitrophenyl)piperazine < 1-Benzhydrylpiperazine < 1-

Benzylpiperazine. The introduction of one carbon chain between phenyl and piperazine in 1-Benzylpiperazine may provide enough flexibility resulting in better inhibition activity as compared to 1-(4-nitrophenyl)piperazine. ERG at the 4th position of the phenyl (R) ring improves the inhibition activity against hAChE and hBACE-1 instead of EWG. Overall the unsubstituted phenyl ring revealed good inhibition against hAChE and hBACE-1 enzymes.

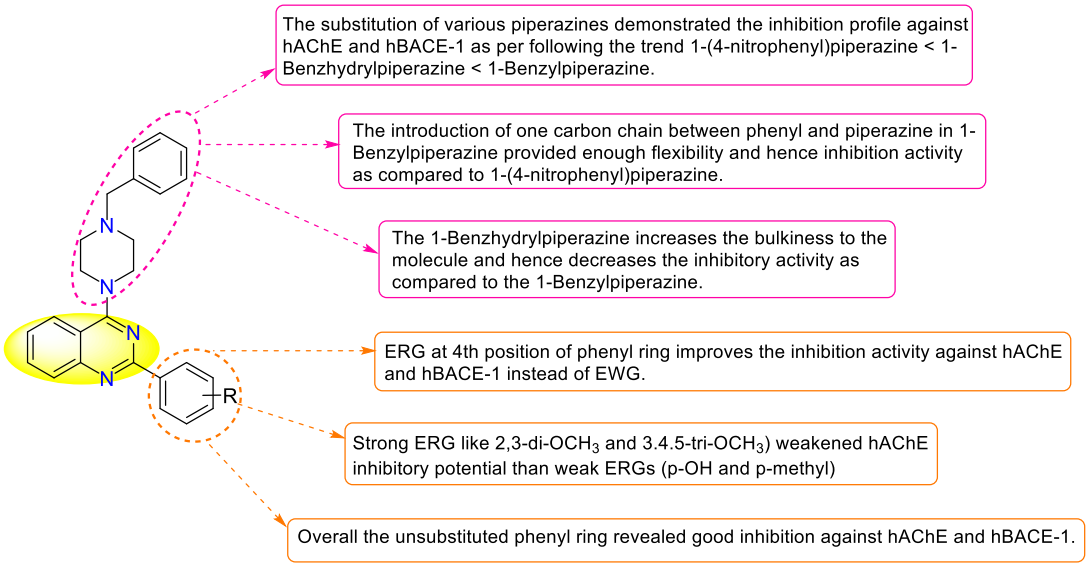

Figure 5.16. SAR of the designed series against hAChE and hBACE-1 enzymes.

5.1.3.1.5. PAMPA-BBB assay

The primary issue with developing drugs to treat AD is their ability to penetrate the BBB. PAMPA-BBB assay was executed to identify the permeability constant of screened compounds (**AV-1**, **AV-2**, and **AV-3**) and compared them with the standard drug donepezil [Di et al. 2003]. The experiment relies on the passive diffusion of compounds from a donor compartment to an acceptor compartment over a parallel artificial membrane constructed of lipids from the porcine brain. The correlation between experimental $P_{e(exp)}$ and reference permeability $P_{e(ref)}$ was established using the permeability of nine commercial drugs as described in our earlier published article as a

standard benchmark for experiment validation and found that the compounds having CNS permeability constant P_e higher than 4.7×10^{-6} cm s^{-1} possess excellent brain permeability and compounds having P_e less than 1.9×10^{-6} cm s^{-1} were considered to acquired poor permeability. However, the permeability values of the compounds in the range of 2.0-4.6 $\times 10^{-6}$ cm s^{-1} proved uncertainty in its permeability. The assay findings demonstrated that all the screened compounds possessed excellent BBB permeability (CNS+) which may be due to the presence of aromatic ring systems imparting lipophilic characteristics of the compounds. The results of the PAMPA-BBB experiment are summarized in

Table **5.7**.

5.1.3.1.6. Propidium iodide displacement assay

In the PAMPA-BBB assay, compounds **AV-1**, **AV-2**, and **AV-3** had the highest levels of brain permeability and were the most effective hAChE inhibitors. Moreover, significant interactions with PAS residues were suggested by molecular docking and dynamics simulation studies. Hence, the PI displacement test was conducted to determine the affinity of these ligands at 10 μM and 50 μM concentrations for the PAS-binding (

Table **5.7**). PI binds to the enzyme's PAS region and increases fluorescence intensity by up to eight times which after being replaced by inhibitors reduce fluorescence intensity [Silva et al. 2013]. Compounds **AV-1**, **AV-2** and **AV-3** exhibited higher displacement of PI (**AV-1**: 10 μM = 15.3%, 50 μM = 24.6%; **AV-2**: 10 μM = 24.1%, 50 μM = 35.4%; **AV-3**: 10 μM = 12.9%, 50 μM = 23.7%) compared to donepezil (10 μM = 22.1%; 50 μM: 33.2%). The assay's results turned out to be consistent with our *in-vitro* hAChE test and computational analyses. Compound **AV-2** was chosen for further evaluations due to its

balance inhibitory potential against both targets (hAChE and hBACE-1), as well as the high displacement of PI from PAS-AChE.

Table 5.7. The PAMPA-BBB permeability and PI displacement assay for screened compounds.

Comp.	PAMPA-BBB permeability		PI displacement from AChE PAS (% inhibition) [b]	
	$P_{e(exp)}$ (10^{-6} cm s^{-1})	Permeability prediction [a]	At 10 μM	At 50 μM
AV-1	6.14 ± 0.16	CNS+	15.3 ± 1.5	24.6 ± 1.2
AV-2	5.82 ± 0.26	CNS+	24.1 ± 1.8	35.4 ± 1.7
AV-3	5.18 ± 0.08	CNS+	12.9 ± 2.4	23.7 ± 2.1
Donepezil	6.80 ± 0.06	CNS+	22.1 ± 1.4	33.2 ± 1.3

[a] 'CNS+' indicated high BBB permeation; [b] The results are expressed as mean ± SEM (n=3).

5.1.3.1.7. Self- and AChE-induced Aβ aggregation inhibition by thioflavin T assay

PI displacement experiment result indicated considerable binding of **AV-2** with AChE-PAS, and the AChE was discovered to be implicated in the advancement of Aβ aggregation by selectively binding to PAS. Specific AChE inhibitors after binding with the PAS may also stop the synthesis and deposition of Aβ [Verma et al. 2022]. Therefore, Compound **AV-2** was subjected to thioflavin T-based fluorometric experiment to determine its anti-Aβ aggregation properties. The experiment was performed at three different concentrations of standard and inhibitors while keeping the Aβ concentration constant (Aβ:inhibitor; 10:5, 10:10, and 10:20 μM) and the results were presented as % Aβ aggregation inhibition in (Figure 5.17) and normalized fluorescence intensity (NFI) in Figure 5.18. **AV-2** showed a comparable anti-Aβ aggregatory profile in self- (**AV-2**:

29.18 - 48.72 %) and hAChE-induced (**AV-2**: 60.38 – 69.00 %) experiments compared to curcumin (Self-induced: 30.91 - 54.01%) and donepezil (hAChE-induced: 40.47 – 65.88%). The % Aβ aggregation inhibition experiment results suggested that compound **AV-2** after binding with the AChE-PAS region there was reduction in the Aβ aggregation. The anti-Aβ aggregation behavior of the compound **AV-2** was further confirmed by the atomic force field microscopy (AFM).

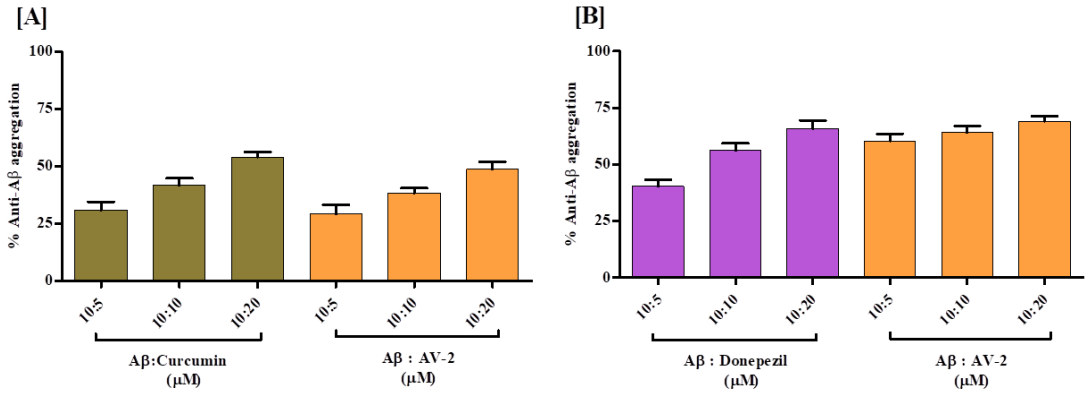

Figure 5.17. Thioflavin T assay of compound **AV-2**, [A] self-induced Aβ aggregation inhibition, [B] AChE-induced Aβ aggregation inhibition.

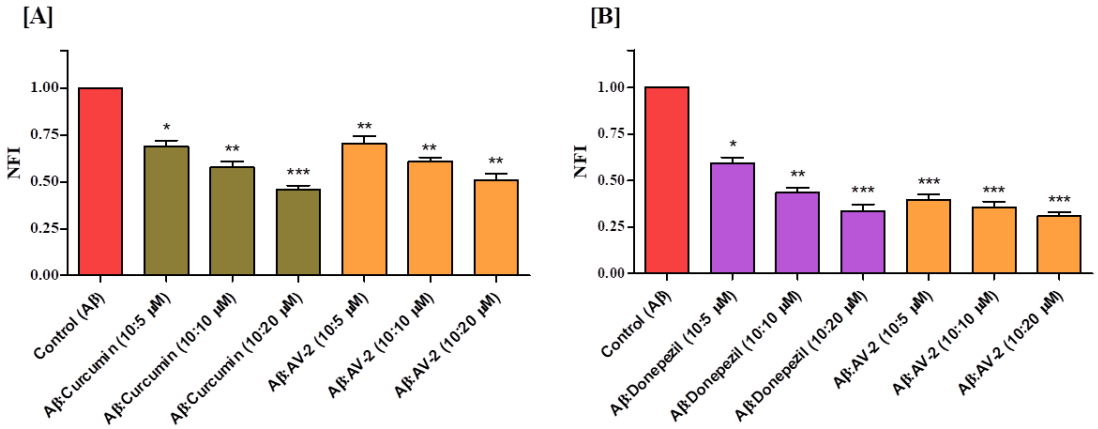

Figure 5.18. Thioflavin T assay with NFI of compound **AV-2** [A] self-induced Aβ aggregation inhibition, [B] hAChE-induced Aβ aggregation inhibition. Data are expressed as mean ± SEM (n=3). $^{*}p < 0.05$, $^{**}p < 0.01$, and $^{***}p < 0.001$ vs control, ns = non-significant.

5.1.3.1.8. AFM studies

AFM studies were carried out to compute the aggregate's size ranges and to view surface topographical maps in high-resolution [Sharma et al. 2019b]. Throughout the incubation period of six days, distinct time intervals were used to investigate the morphological changes of Aβ aggregates with or without inhibitor **AV-2**. AFM pictures were used to visually confirm the production of Aβ clumps, fibrils, and large oligomers. Additionally, maximum peak heights were determined to confirm the ability of compound **AV-2** to disaggregate the Aβ plaques. Aβ without inhibitor leads to the generation of oligomers and fibrils on 3rd day. Due to its aggregation over the incubation period of 3 days, the AFM histogram analysis revealed an increase in the maximum peak height of aggregates from 70 to 7400 nm. Further compound **AV-2** was incubated for 72 h with the aggregates formed after 3 days resulting in a sharp reduction in the maximum peak height of the aggregates (from 7400 to 100 nm).

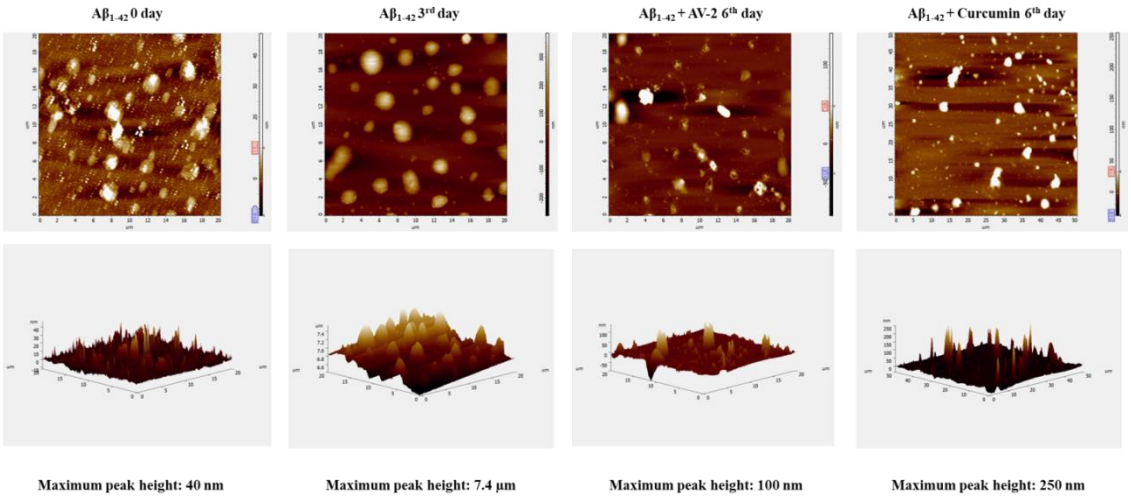

Figure 5.19. 2D and 3D AFM analysis of anti-Aβ aggregation potential of compound **AV-2** and curcumin at different time intervals.

While, the curcumin as a reference compound showed decrease in maximum peak height from 7400 to 150 nm. The results of the AFM experiment proved that compound **AV-2** significantly reduces the Aβ aggregation and also stop its further aggregation (Figure 5.19).

5.1.3.1.9. Neurotoxicity estimation on RA/BDNF differentiated SH-SY5Y cell lines

The neurotoxic liability of test compound **AV-2** was checked on retinoic acid (RA)/brain-derived neurotrophic factor (BDNF)-induced differentiated SH-SY5Y cell lines. In comparison to undifferentiated SH-SY5Y cell lines, the differentiated cell lines showed neuron-like characteristics after being treated with RA or BDNF, including larger neurite structures and increased axon span. These cells also exhibited neurite connections with surrounding cells [Forster et al. 2016]. The four increasing concentrations 10, 20, 40, and 80 μM of compound **AV-2** were taken and compared with the same concentrations of standard donepezil. The results indicated that upon exposure of compound **AV-2** to differentiated neuroblastoma SH-SY5Y cell lines at maximum tested concentration of 80 μM showed higher % cell viability as compared to maximum tested concentration of donepezil ($^{*}p < 0.05$). The % cell viabilities was observed in the range of 76.96-82.95% at the tested concentrations which indicated that compound **AV-2** was non-neurotoxic and did not affect the neuroblastoma cell integrity including their shape or structures that resemble neuron-like properties (Figure 5.20 and Figure 5.21).

5.1.3.1.10. Neuroprotective estimation on RA/BDNF differentiated SH-SY5Y cell lines

On differentiated SH-SY5Y cell lines, the neuroprotective activity of the compound **AV-2** was calculated. Briefly, the cells were incubated in the presence of different concentrations of compound **AV-2** (5, 10, and 20 μM) for 2 h. After that, H_2O_2 (200 μM) was incorporated into each well and further incubated for 24 h. The results indicated that the cell viability was significantly reduced to the minimum (43.86%) ($^{\pi\pi\pi}p < 0.001$) in H_2O_2 treated group. While in the case of compound **AV-2** and standard donepezil, the cell viability was enhanced in a dose-dependent manner. The compound **AV-2** demonstrated cell viability of 51.33% ($^{*}p < 0.05$) at 5 μM, 61.15% ($^{**}p < 0.01$) at 10 μM, and 77.47%

($^{***}p < 0.001$) at 20 µM concentrations and found statistically non-significant as compared to the donepezil having cell viability 58.75% ($^{*}p < 0.05$) at 5 µM, 67.58% ($^{**}p < 0.01$) at 10 µM, and 82.88% ($^{***}p < 0.001$) at 20 µM concentrations which indicated neuroprotective behavior of representative compound **AV-2** (Figure 5.20).

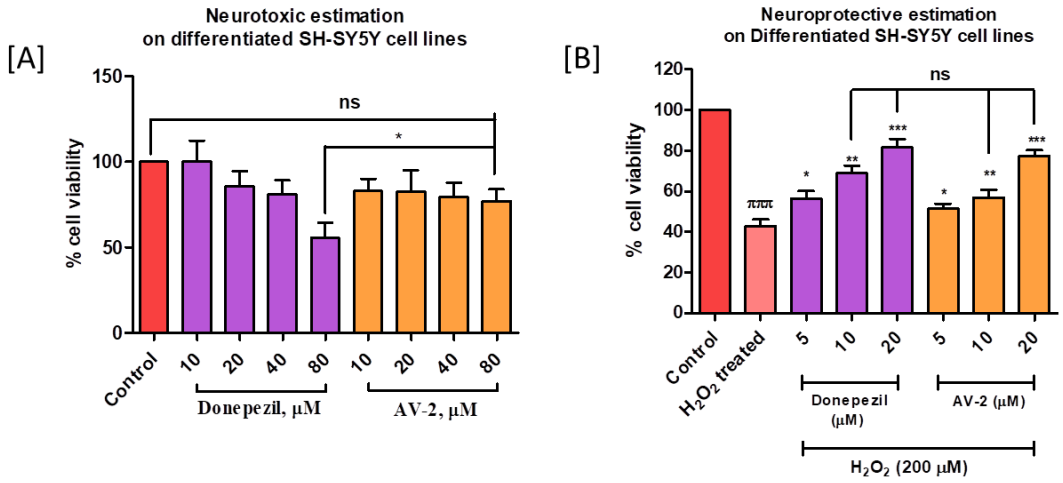

Figure 5.20. Neurotoxicity (A) and neuroprotective analysis (B) of compound **AV-2** on RA/BDNF differentiated neuroblastoma cell lines. Data are expressed as mean ± SEM (n=3). $^{\pi\pi\pi}p < 0.001$ vs control; $^{*}p < 0.05$, $^{**}p < 0.01$, and $^{***}p < 0.001$ vs H_2O_2 treated; ns = non-significant.

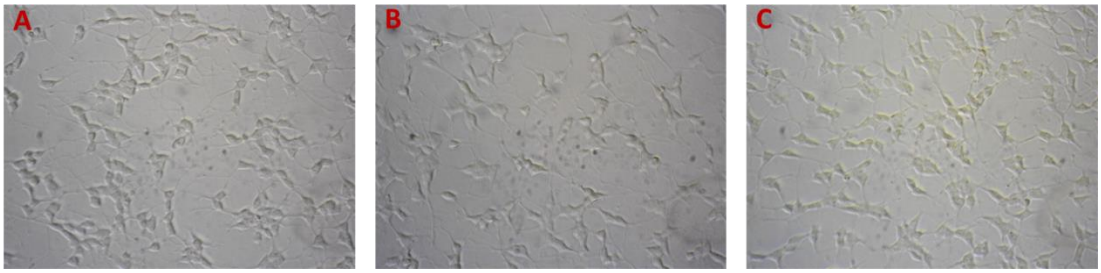

Figure 5.21. Cell morphological study on RA/BDNF differentiated neuroblastoma cell lines, [A] Control; [B] after treatment with donepezil; [C] after treatment with compound **AV-2**.

5.1.3.2. *In-vivo* and *ex-vivo* studies

5.1.3.2.1. Acute toxicity studies

As per following the OCED guidelines 423, the acute toxicity study of compound **AV-2** was determined on female Wistar rats. A dose of 500 mg/kg p.o was administered and the

animals were examined for up to 14 days. The careful observation of the group of animals treated with compound **AV-2** suggested that the compound was well tolerated and exhibited no signs of adverse responses or any toxicity. However, a slight weight loss was observed in treated animals for the initial days i.e. up to 4 days after which they regained their weight during the study. The hepatic and renal function tests revealed that all the related parameters were within the normal range. After the study, the histopathological examination of various organs like the kidney, liver, brain, lungs, and heart was performed which indicated normal morphological and tissue appearance. These findings indicated that the compound **AV-2** had a substantial margin of safety (Figure 5.22).

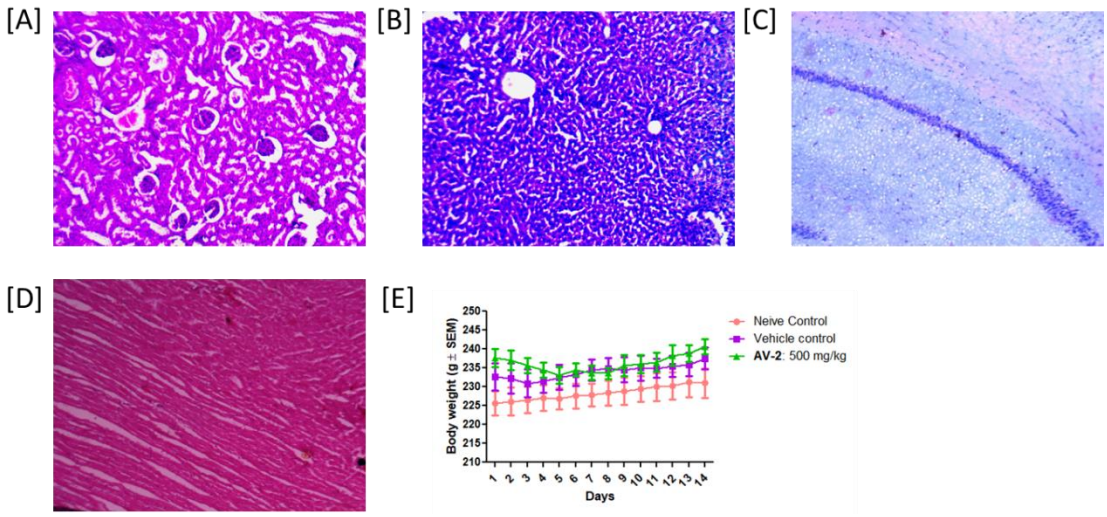

Figure 5.22. Histopathological examination of the different animal organs via H & E staining after acute toxicity studies; [A] Kidney tissue showing normal DCT, PCT and Glomerulus; [B] Liver tissue showing the presence of normal Kupfer cells; [C] brain tissue showing normal hippocampus and cortex after crystal violet staining; [D] Heart slice showing normal cardiac muscles; [E] change in body weight up to 14 days.

Table 5.8. Liver and kidney function test of experimental animals under acute toxicity studies.

Parameters	**Control (±SD)**	**100mg/kg (±SD)**	**300mg/kg (±SD)**	**500mg/kg (±SD)**
AST (U/L)	131 ± 14.6	129 ± 11.9	132 ± 10.4	136 ±12.5

ALT (U/L)	47 ± 4.3	45 ± 4.7	46 ± 3.9	49 ± 4.0
ALP (KA/dL)	13 ± 2.1	13 ± 1.8	14 ± 1.4	16 ± 1.6
Creatinine (mg/dL)	0.59 ± 0.03	0.66 ± 0.02	0.71 ±0.02	0.77 ± 0.03

5.1.3.2.2. Scopolamine-induced amnesia models for testing cognition enhancement in rats

To check the memory and cognition behavioral improvement of compound **AV-2**, the scopolamine-induced Y-maze test was carried out. The scopolamine is a gold standard medication and used to study cognitive dysfunction owing to its ability to cause cholinergic deficiency [Klinkenberg and Blokland 2010]. Compound **AV-2** at the doses of 5, 10, and 20 mg/kg p.o. was administered daily to the healthy male Wistar rats for 7 days. The Y-maze experiment was carried out on the 7th day of the trial to determine the spatial working memory after injecting scopolamine intraperitoneally in rats. The treatment dose was given before 30 min of scopolamine and the % spontaneous alterations were evaluated. The findings were consistent with the *in-vitro* investigations and indicated that compound **AV-2** would likely reversed the dementia caused by scopolamine. In the scopolamine group of rats, the % spontaneous alternations were significantly lower ($^{\pi\pi\pi}p < 0.001$) as compared to the control group (**Figure 5.23**), suggesting impaired learning and memory functions. Significantly increased (***$p < 0.001$) % spontaneous alterations were observed in donepezil (5 mg/kg) and compound **AV-2** (20 mg/kg) as compared to scopolamine ($^{\pi\pi\pi}p < 0.001$). The compound **AV-2** (20 mg/kg) indicated statistically non-significant (***$p < 0.001$) % spontaneous alterations as compared to the donepezil (5 mg/kg). In all groups, total arm entries (Figure 5.23) remained almost constant which demonstrated that scopolamine did not interfere with

animal locomotor activity. The outcomes of the scopolamine-induced Y-maze studies supported that compound **AV-2** has the capability to improve memory deficit functions.

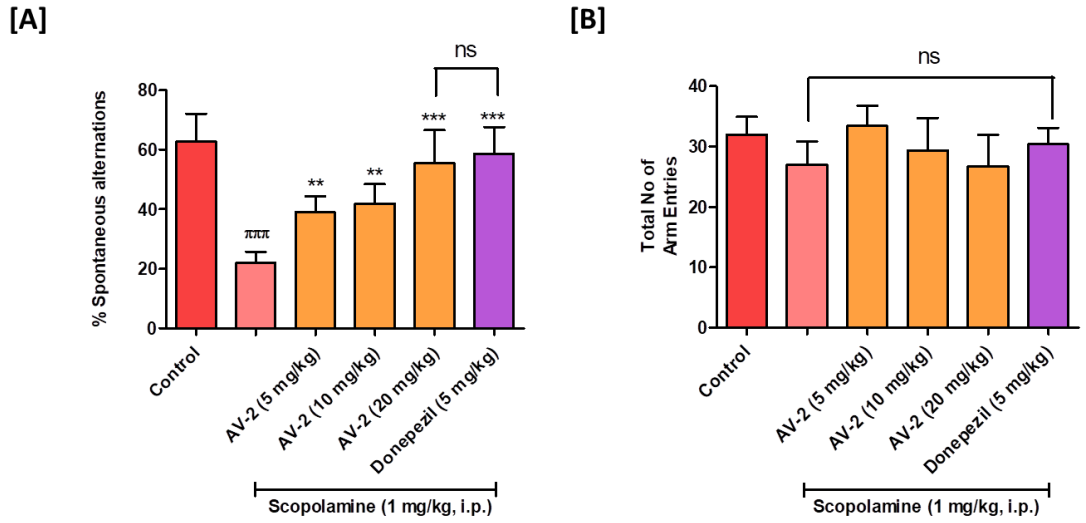

Figure 5.23. Effect of compound **AV-2** and donepezil in cognition enhancement *via* scopolamine-induced Y-maze amnesia model: [A] % spontaneous alterations, [B] Total no of arm entries. Data are expressed as mean ± SEM (n=6). $^{\pi\pi\pi}p < 0.001$ vs control; $^{**}p < 0.01$, and $^{***}p < 0.001$ vs scopolamine; ns = non-significant.

5.1.3.2.3. Ex-vivo and biochemical estimation

Ex-vivo studies using modified Ellman's technique was performed to assess brain hippocampal AChE levels post **AV-2** treatment [Ellman et al. 1961]. The results indicated that the scopolamine group of rats had elevated AChE levels and a higher rate of substrate hydrolysis than the control group (Figure 5.24A) ($^{\pi\pi\pi}p < 0.001$). The AChE levels were significantly attenuated upon treatment with compound **AV-2** in a dose dependent manner as compared to the scopolamine group. While, in comparison to the standard donepezil (5 mg/kg) group, the AChE inhibitory potential of compound **AV-2** at 20 mg/kg was found to be statistically non-significant ($^{***}p < 0.001$) which also confirm BBB permeability of the compound **AV-2**.

Upon scopolamine i.p. administration the AChE level goes up which results in subsequent decreases of ACh level in the brain [Tota et al. 2012]. Therefore, the ACh level in the brain hippocampal was also evaluated following the manufacture's procedure (KRISHGEN Biosystems, rat acetylcholine ACh GENLISA ELISA kit). The results indicated that the ACh level in the brain hippocampal of the scopolamine treated group ($^{\pi\pi\pi}p < 0.001$) was significantly reduced as compared to the control group. While **AV-2** treated group at a dose of 20 mg/kg were found to be statistically significant ($^{***}p < 0.001$) as compared to the scopolamine group (Figure 5.24B). However, the 20 mg/kg treated group showed statistically non-significant ($^{***}p < 0.001$) results as compared to the standard donepezil 5 mg/kg.

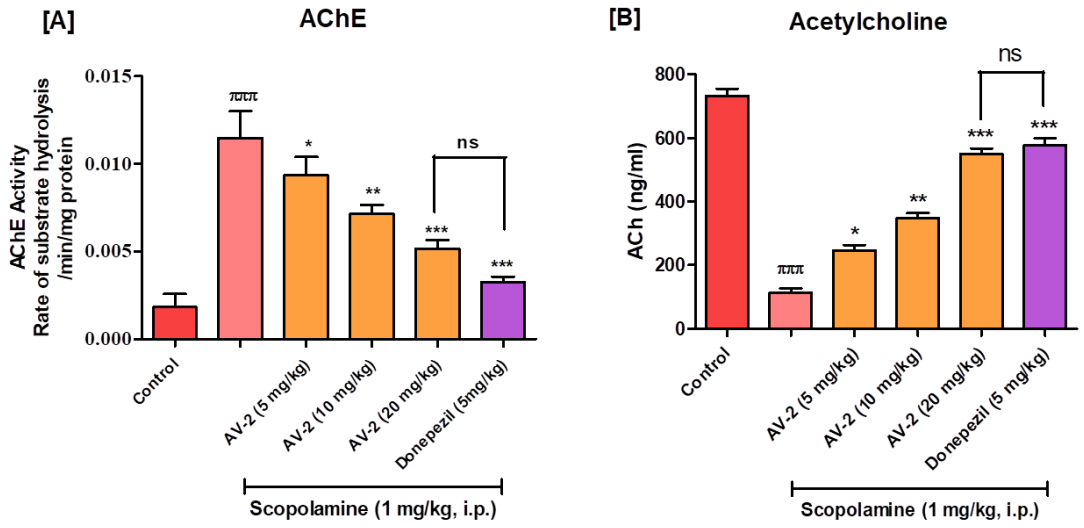

Figure 5.24. *Ex-vivo* analysis of compound **AV-2** [A] AChE levels in hippocampal brain and [B] Acetylcholine levels in hippocampal brain. Data are expressed as mean ± SEM (n=6). $^{\pi\pi\pi}p < 0.001$ vs control; $^{*}p < 0.05$, $^{**}p < 0.01$, and $^{***}p < 0.001$ vs scopolamine; ns = non-significant.

The levels of oxidative stress biomarkers like malonaldehyde (MDA) and superoxide dismutase (SOD) were also estimated in the brain hippocampal homogenates. MDA is a by-product of lipid peroxidation reactions and SOD is actively engaged in the dismutation of superoxide radical to free oxygen and can be studied as an oxidative stress biomarkers.

According to our *ex-vivo* results, scopolamine administration to the experimental animals causes oxidative stress, raised MDA levels ($^{\pi\pi\pi}p < 0.001$), and decreases superoxide dismutation and consequently, SOD levels ($^{\pi\pi\pi}p < 0.001$). The **AV-2** treated groups demonstrated significant decrease in the MDA levels and increase in SOD levels in a dose dependent manner (5, 10, and 20 mg/kg, respectively) as shown in Figure 5.25A & B. It was also observed that **AV-2** (20 mg/kg) and donepezil (5 mg/kg) treated group had statistically non-significant difference.

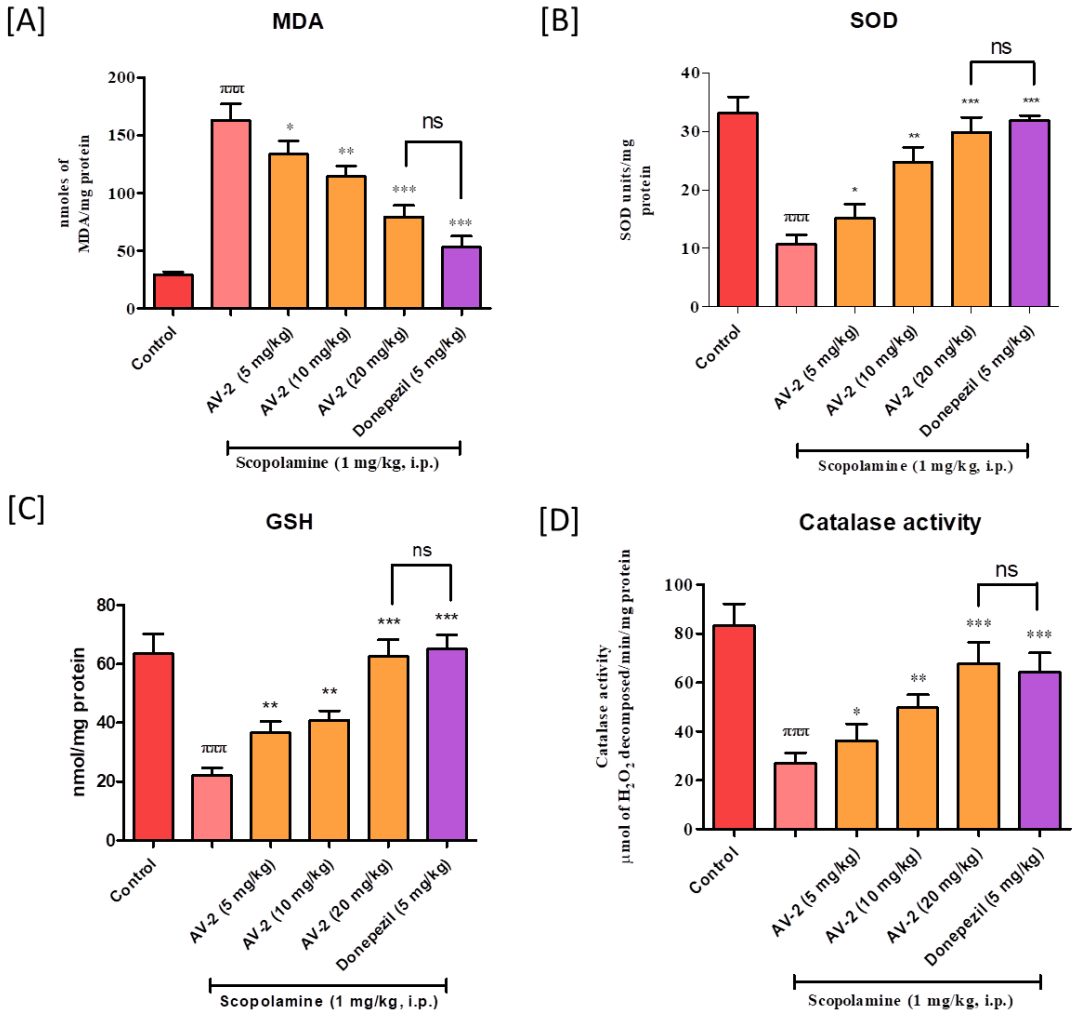

Figure 5.25. *Ex-vivo* analysis of compound **AV-2** in hippocampal brain of experimental animals: [A] MDA level, [B] SOD level, [C] GSH level, and [D] catalase level. Data are expressed as mean ± SEM (n=6). $^{\pi\pi\pi}p < 0.001$ vs control; $^{*}p < 0.05$, $^{**}p < 0.01$, and $^{***}p < 0.001$ vs scopolamine; ns = non-significant.

The glutathione (GSH) and catalase levels were also determined in the hippocampal brain homogenate of all the experimental groups and results indicated that there was significant increase in both GSH and catalase levels in a dose dependent manner (5, 10, and 20 mg/kg) in **AV-2** treated groups. These biomarker levels in **AV-2** (20 mg/kg) treated group were found statistically non-significant as compared to the donepezil (5 mg/kg) (Figure 5.25C & D).

5.1.3.2.4. $A\beta_{1-42}$ induced ICV rat model: Morris water maze test

The primary component of senile plaques in AD patient brains is Aβ, and its deposition has been linked with the elevated activity of BACE-1. Therefore, Administering $A\beta_{1-42}$ intracerebroventricularly (ICV) is one of the most effective ways to induce learning and memory impairments as well as the phenotypic condition that resembles AD [Chambon et al. 2011]. After injecting Aβ (4 μM, 5 μL) into all groups except the sham group (only vehicle was injected) and, the animals were kept for 7 days for Aβ oligomer/plaque generation. The Morris water maze test was utilized to evaluate the anti-Aβ aggregation potential of compound **AV-2** in rat models. Rats from all groups received the appropriate treatments for nine days after the seven-day rest period. The Morris water maze experiment was conducted to measure escape latency time (ELT) and the number of platform crossings over 90 seconds during the final five days of therapy. The results indicated that in the diseased model group, the ELT was significantly higher ($^{a}p < 0.05$) while the time spent in the platform quadrant, and the number of platform crossing were gradually declined as compared to the control group which suggested learning and memory impairment. After treatment with standard donepezil (5 mg/kg) and compound **AV-2** (20 mg/kg)**,** there was a significant decrease in the ELT while an increase in the number of platform crossing ($^{b}p < 0.05$), and time spent in the platform quadrant ($^{b}p < 0.05$) as compared to the disease group (Aβ). The **AV-2** (20 mg/kg) and donepezil (5

mg/kg) results were found statistically non-significant which demonstrated that compound **AV-2** remarkably improved the learning and cognitive functions at maximum (20 mg/kg) tested concentration (Figure 5.26).

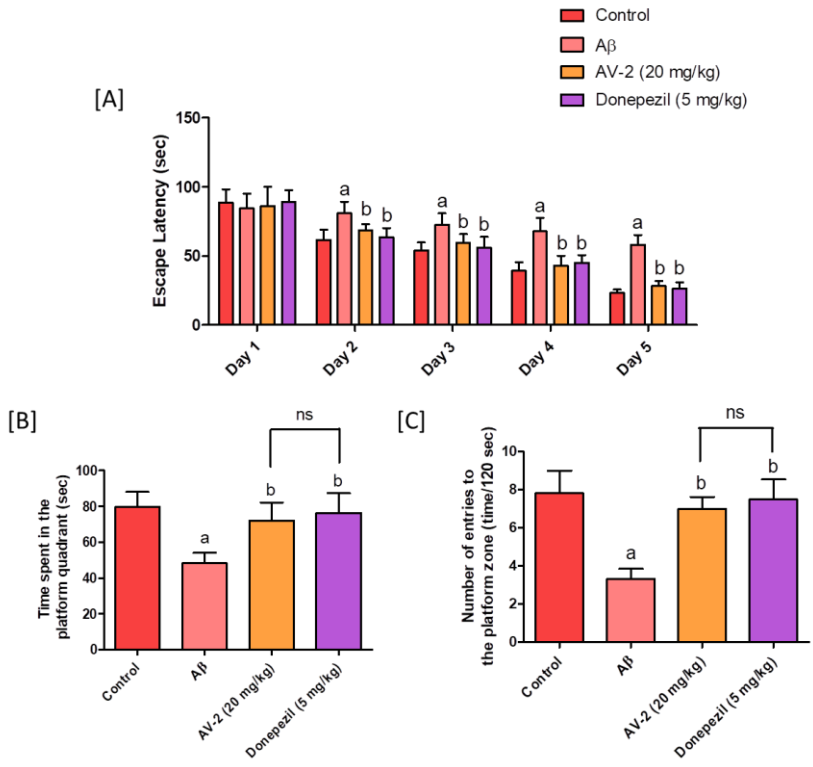

Figure 5.26. Effect of compound **AV-2** and donepezil *via* ICV $A\beta_{1-42}$-induced Morris water maze test: (A) escape latency; (B) time spent in the platform quadrant; and (C) a number of entries to the platform zone.

5.1.3.2.5. Western blot analysis

The BACE-1, APP, and Tau proteins were linked and played a significant role in development and progression of AD [Verma et al. 2022]. Therefore, after the Morris water maze test, the molecular expression levels of these proteins were estimated in the hippocampal tissue of all the experimental animal groups via Western blot analysis. The findings suggested that the molecular expression of proteins (BACE-1, APP, and Tau) were significantly increased in the diseased model group as compared to the sham group. Treatment with compound **AV-2** significantly attenuated these proteins expression.

Additionally, the protein expressions were found statistically non-significant as compared to the donepezil treated group and corroborate our *in-vivo* findings (Figure 5.27).

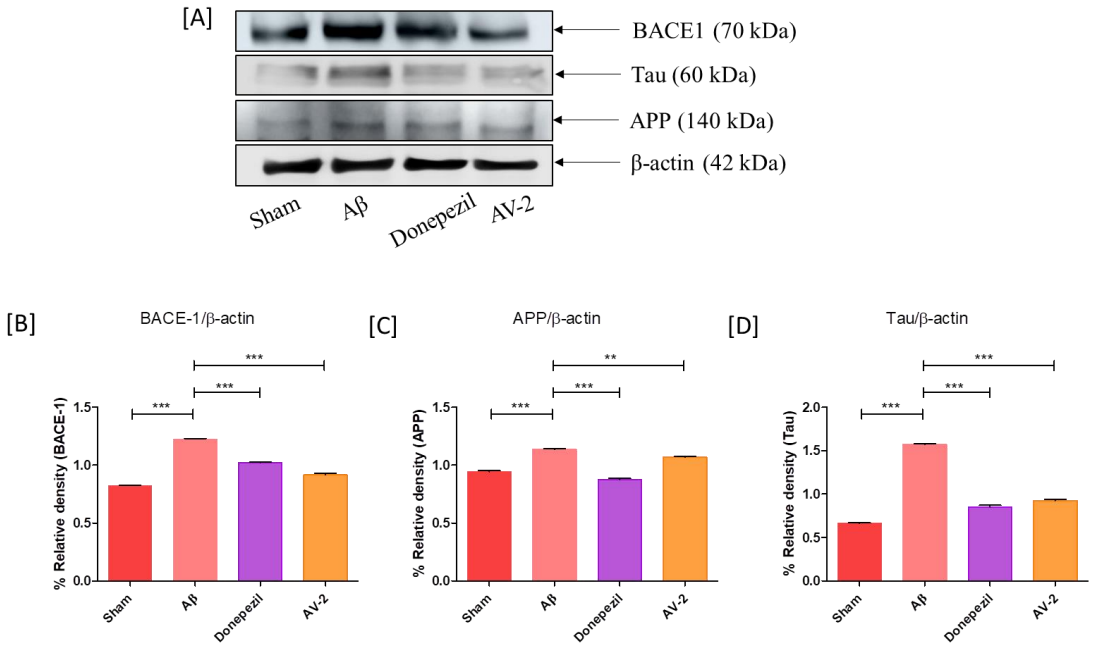

Figure 5.27. Western blot analysis of molecular protein expressions in hippocampal brain of compound **AV-2** treated rats after Aβ administered (ICV). [A] Western blot representing bands; [B] Quantification of BACE-1 expression; [C] Quantification of APP expression; [D] Quantification of Tau expression. ***p < 0.001 and **p < 0.01 vs Aβ diseased model. Values are expressed as mean ± SEM (n=3).

5.1.3.2.6. Immunohistochemistry analysis

The immunohistochemistry (IHC) analysis was performed to determine the expression of BACE-1 and Aβ in the hippocampal region of different experimental groups like sham, Aβ diseased model, compound **AV-2**, and donepezil treated groups. The IHC results indicated that the expression of BACE-1 and Aβ were significantly (***p < 0.001) elevated in diseased (Aβ) group as compared to the sham group while after treatment with compound **AV-2**, the expression of these proteins were significantly (***p < 0.001) reduced as compared to the Aβ diseased group and found statistically non-significant (***p < 0.001) as compared to the standard donepezil-treated group (Figure 5.28).

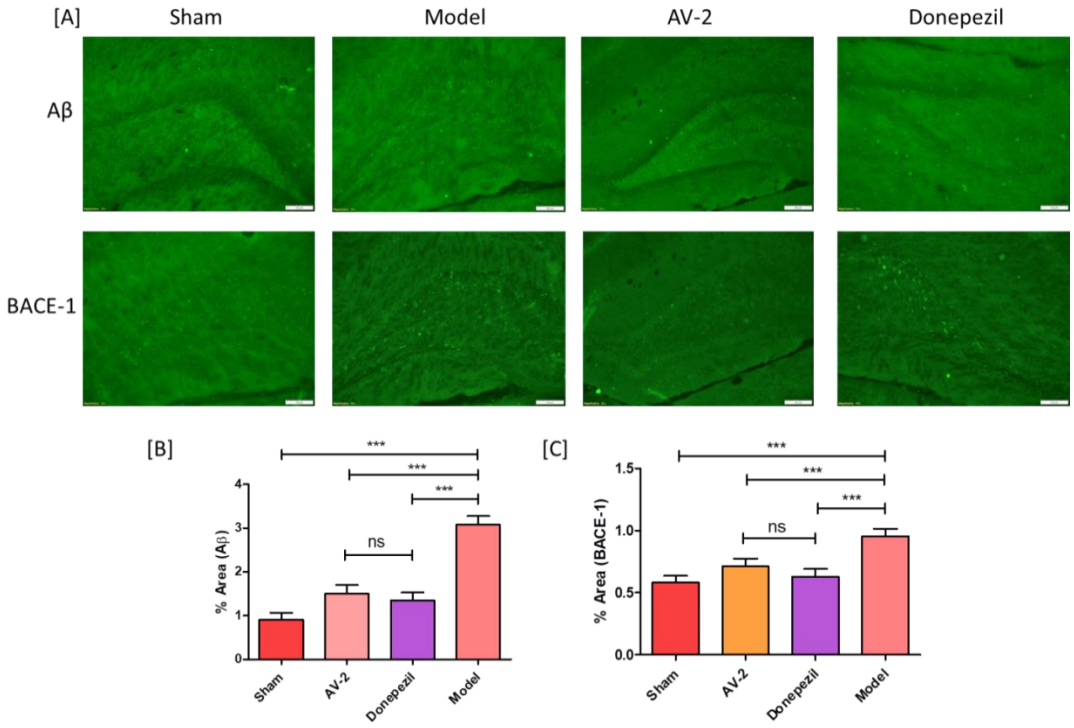

Figure 5.28. The Aβ and BACE-1 expression levels estimated *via* IHC analysis: [A] Representing IHC images of different experimental groups; [B] Densitometric quantification of % area of Aβ expression; [C] Densitometric quantification of % area of BACE-1 expression. ***p < 0.001 vs Model; ns = non-significant. Values are expressed as mean ± SEM (n=3).

5.1.3.2.7. Brain histopathology

The histopathology of the rat brain tissue was carried out in the control, Aβ, donepezil, and **AV-2** treated groups via Nissl staining. The morphology and number of neuronal cells were estimated. When compared to the control group, the histopathological examination of the $A\beta_{1-42}$ infused group revealed disorganized neuronal arrangement, vacuolar fiber development, and decreased neuronal density. While, in the case of donepezil (5 mg/kg) and **AV-2** (20 mg/kg) treated groups, the neuronal density was higher as compared to the $A\beta_{1-42}$ infused group while the morphology of the DG region was almost similar to that of the Sham group (Figure 5.29).

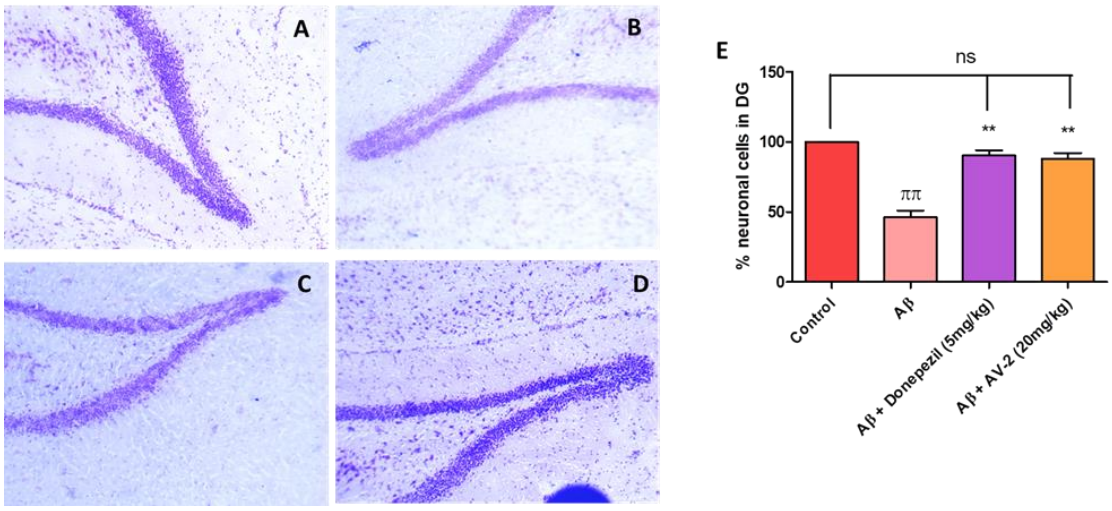

Figure 5.29. Histopathological examination of brain hippocampal (Dentate gyrus DG): [A] control, [B] Aβ-treated, [C] Aβ+Donepezil-treated, [D] Aβ+**AV-2**-treated, [D] % neuronal density in DG with respect to control. $^{\pi\pi}p < 0.01$ vs control; $^{**}p < 0.01$ vs Aβ treated.

5.1.3.2.8. In-vivo blood-brain permeability

The 10 and 20 mg/kg doses of compound **AV-2** were orally administered for four consecutive days to their respective treatment rat groups (n=3). On the fourth day, the rats were sacrificed and their brain tissue homogenates were prepared. The HPLC analysis was performed to evaluate the *in-vivo* blood-brain permeability. The calibration curve was plotted using different concentrations of compound **AV-2** and their respective areas. The concentration of compound **AV-2** in the brain homogenate was determined using standard calibration curve. The results indicated that the concentrations of **AV-2** in brain homogenate after oral administration of 10 and 20 mg/kg doses were 0.0153 and 0.0547 µg/mL respectively. The study suggested that compound **AV-2** was partitioned across the BBB and could reach to the specific targeted area in the brain.

5.1.3.2.9. Pharmacokinetic study

In healthy male Wistar rats, preliminary pharmacokinetic study of compound **AV-2** was planned at a dose of 20 mg/kg, p.o. At various time intervals, the blood was collected

from the retro-orbital plexus as discussed in the experimental section. The extravascular non-compartment model was considered and the analysis was executed to calculate the PK parameters using PK solver software (version 2.0). The findings indicated that compound **AV-2** has peak plasma concentration C_{max} = 10.65 ± 0.8 µg/mL achieved at T_{max} = 1 ± 0.1 h. The elimination half-life ($t_{1/2}$) and mean residence time (MRT) were found to be 7.95 ± 1.3 h and 10.09 ± 0.9 h, respectively. These findings indicated that the compound **AV-2** produced good oral absorption and bioavailability (Table 5.9) (Figure 5.30).

Table 5.9. The findings of Pharmacokinetic analysis after oral administration of compound **AV-2** (20 mg/kg).

Parameters	**Effect of compound AV-2**[a]
C_{max} (µg/mL)	10.65 ± 0.8
T_{max} (h)	1 ± 0.1
$(AUC)_{0-t}$ (µg/mL[a]*h)	73.45 ± 3.2
$t_{1/2}$	7.95 ± 0.3
MRT (h)	10.09 ± 0.9

[a]The values are represented as mean ± SEM (n=3)

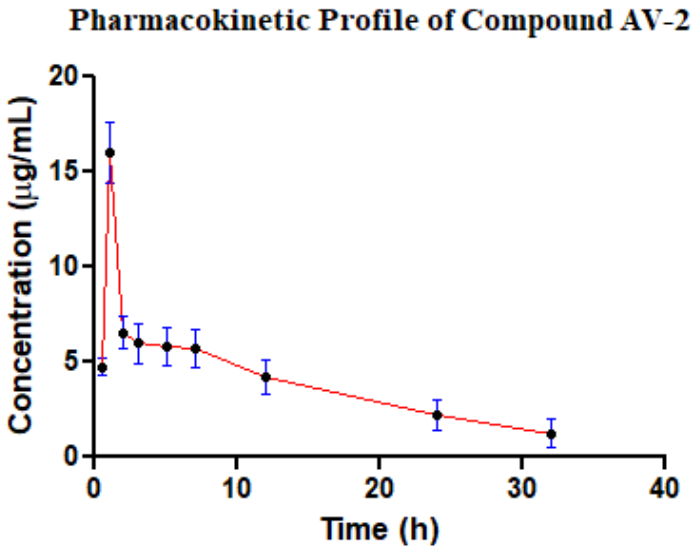

Figure 5.30. Pharmacokinetic analysis of compound **AV-2** representing its plasma concentration with respect to time.

5.2. PART-II : SERIES-II

5.2.1. Chemistry

5.2.1.1. Synthesis of Series II (AK-1 to AK-14)

The proposed series of compounds **AK-1** to **AK-14** were synthesized and characterized as per Scheme 2. The 2-amino-4,5-dimethoxybenzamide (**1b**) was treated with formaldehyde using an I_2-catalysed oxidative coupling reaction in CH_3OH at 80°C for 3-5 h to synthesize the desired intermediate 6,7-dimethoxyquinazolin-4(3*H*)-one (**2b**). The appearance of a typical stretching band at the vicinity of 3300 cm^{-1} in FTIR-ATR represents the cyclization and formation of amide linkage in the intermediate (**2b**). The intermediate **(2b)** formation was also confirmed by the ^1H NMR spectroscopy which displayed the characteristic 3 aromatic peaks in the range of 9-7 ppm. The chlorination of intermediate (**2b**) was carried out by dissolving it into dry dichloromethane (DCM) and adding $SOCl_2$ with a catalytic amount of N, N-dimethylformamide (DMF) at 40 °C to synthesize the secondary intermediate 4-chloro-6,7-dimethoxyquinazoline (**3b**). In FTIR-ATR, the appearance of the characteristic peak of chlorine at 767 cm^{-1}, confirmed the

substitution of chlorine in place of C=O. The structural confirmation of the secondary intermediate (**3b**) was also done by ^{13}C NMR, which displayed the characteristics signals of (Cl-C=N and N=C) at δ_C = 159.10 and 156.81 ppm. Targeted compounds (**AK-1** to **AK-14**) were synthesized by treating the secondary intermediate (**3b**) with substituted piperazines in the presence of K_2CO_3 in DMF at 80 °C for 3-4 h. FT-IR spectra of **AK-1** to **AK-14** revealed that the -Cl signal vanished at 767 cm^{-1} and a distinctive stretching band for the (C-N) of linked piperazine moiety appeared between 1350 and 1000 cm^{-1}. The synthesis of the compounds **AK-1** to **AK-14** was confirmed by the development of an eight-proton piperazine ring signal in the δ_H = 2-4 ppm range in the ^1H NMR spectra. The equatorial and axial hydrogens interconversions in the boat and chair conformations of piperazine, the piperazine moiety of all the designed compounds **AK-1** to **AK-14** displayed two larger triplet peaks for both -NCH_2. Additionally, the piperazine ring of the compounds **AK-1** to **AK-14** appeared to have signals in between δ_C = 40-50 ppm of ^{13}C NMR spectra. By using mass spectrophotometry, the molecular weights of all synthesized compounds were determined. The HPLC percentage purity of all the targeted compounds was also checked and found to be more than 95%.

5.2.1.2. Characterization of the intermediate 2b

5.2.1.2.1. 6,7-dimethoxyquinazolin-4(3*H*)-one (2b)

Yield: 68%; mp: 162-164 ^oC; R_f = 0.95 (MeOH:DCM, 3:97 v/v); α-ATR (υ cm^{-1}): 1222,1121 (Ph-O-CH_3), 1591 (C=N), 2929 (C-H, aromatic), 767 (-Cl); ^1H NMR (500 MHz, $\delta_{H,}$ $CDCl_3$): 8.70 (s, 1H), 7.28 (s, 1H), 7.11 (s, 1H), 4.04 (s, 3H), 4.01 (s, 3H). ^{13}C NMR (125 MHz, $\delta_{C,}$ $CDCl_3$): 154.89, 154.67, 153.05, 149.23, 148.75, 111.60, 107.61, 102.71, 28.43.

5.2.1.3. Characterization of the intermediate 3b

5.2.1.3.1. 4-chloro-6,7-dimethoxyquinazoline (3b)

Yield: 68%; MW: 224.64; mp: 162-164 ^{o}C; R_f = 0.95 (MeOH:DCM, 3:97 v/v); α-ATR (υ cm^{-1}): 1222,1121 (Ph-O-CH_3), 1591 (C=N), 2929 (C-H, aromatic), 767 (-Cl); ^{1}H NMR (500 MHz, $\delta_{H,}$ $CDCl_3$): 8.89 (s, 1H), 7.42 (s, 1H), 7.37 (s, 1H), 4.10 (s, 3H), 4.10 (s, 3H). ^{13}C NMR (125 MHz, $\delta_{C,}$ $CDCl_3$): 159.10, 156.81, 152.50, 151.48, 149.06, 119.60, 106.90, 102.69, 56.66, 56.47.

5.2.1.4. Characterization of the targeted compounds (AK-1 to AK-14)

5.2.1.4.1. 4-(4-benzhydrylpiperazin-1-yl)-6,7-dimethoxyquinazoline (AK-01)

Yield: 84%; mp: 161-163 ^{o}C; R_f = 0.48 (MeOH:DCM, 3:97 v/v); α-ATR (υ cm^{-1}): 1246,1107 (Ph-O-CH_3), 993 (C-N), 1586 (C=N), 3354 (C-H, aromatic); ^{1}H NMR (500 MHz, $\delta_{H,}$ $CDCl_3$): 8.67 (s, 1H), 7.50 – 7.48 (m, 3H), 7.31 (dd, *J* = 16.5, 8.7 Hz, 5H), 7.24 – 7.21 (m, 3H), 7.09 (s, 1H), 4.34 (s, 1H), 4.03 (s, 3H), 3.95 (s, 3H), 3.70 (t, *J* = 5.1 Hz, 4H), 2.64 (t, *J* = 5.3 Hz, 4H).^{13}C NMR (125 MHz, $\delta_{C,}$ $CDCl_3$): 163.83, 154.44, 153.14, 149.12, 148.41, 142.42, 128.64, 127.92, 127.15, 111.50, 107.53, 103.19, 76.34, 56.20, 56.03, 51.89, 49.93. HPLC purity: 98.83%, rt: 2.026 min. ESI-MS (m/z): 441.221 $[M + H]^{+}$.

5.2.1.4.2. 4-(4-benzylpiperazin-1-yl)-6,7-dimethoxyquinazoline (AK-02)

Yield: 76%; mp: 153-155 ^{o}C; R_f = 0.51 (MeOH:DCM, 3:97 v/v); α-ATR (υ cm^{-1}): 1333,1199 (Ph-O-CH_3), 987 (C-N), 1666 (C=N), 3105 (C-H, aromatic); ^{1}H NMR (500 MHz, $\delta_{H,}$ $CDCl_3$): 8.67 (s, 1H), 7.40 – 7.34 (m, 5H), 7.30 (dt, *J* = 6.8, 2.4 Hz, 2H), 7.11 (s, 1H), 4.03 (s, 3H), 3.98 (s, 3H), 3.71 (t, *J* = 5.3 Hz, 4H), 3.62 (s, 2H), 2.69 (t, *J* = 5.1 Hz, 4H).^{13}C NMR (125 MHz, $\delta_{C,}$ $CDCl_3$): 163.81, 154.46, 153.12, 149.15, 148.42,

137.82, 129.16, 128.34, 127.25, 111.46, 107.54, 103.21, 63.10, 56.03, 52.98, 49.72. HPLC purity: 99.39%, rt: 1.891 min. ESI-MS (m/z): 365.190 $[M + H]^+$.

5.2.1.4.3. 6,7-dimethoxy-4-(4-(4-nitrophenyl)piperazin-1-yl)quinazoline (AK-03)

Yield: 71%; mp: 167-169 ^oC; R_f = 0.41 (MeOH:DCM, 3:97 v/v); α-ATR (υ cm^{-1}): 1312, 1197 (Ph-O-CH_3), 981 (C-N), 1583, 1391 (-NO_2), 1666 (C=N), 3104 (C-H, aromatic); ^1H NMR (500 MHz, $\delta_{H,}$ $CDCl_3$): 8.72 (s, 1H), 8.18 (d, *J* = 9.3 Hz, 2H), 7.31 (s, 1H), 7.16 (s, 1H), 6.91 (d, *J* = 9.5 Hz, 2H), 4.06 (s, 3H), 4.03 (s, 3H), 3.89 (t, *J* = 5.2 Hz, 4H), 3.69 (t, *J* = 5.0 Hz, 4H).^{13}C NMR (125 MHz, $\delta_{C,}$ $CDCl_3$): 163.52, 154.83, 154.66, 152.96, 149.27, 148.90, 138.98, 125.98, 112.77, 111.45, 107.67, 102.65, 56.32, 49.02, 46.76. HPLC purity: 98.89%, rt: 2.126 min. ESI-MS (m/z): 396.159 $[M + H]^+$.

5.2.1.4.4. 6,7-dimethoxy-4-(4-phenylpiperazin-1-yl)quinazoline (AK-04)

Yield: 78%; mp: 159-161 ^oC; R_f = 0.56 (MeOH:DCM, 3:97 v/v); α-ATR (υ cm^{-1}): 1331, 1088 (Ph-O-CH_3), 980 (C-N), 1664 (C=N), 2926 (C-H, aromatic); ^1H NMR (500 MHz, $\delta_{H,}$ $CDCl_3$): 8.71 (s, 1H), 7.32 (dd, *J* = 10.6, 5.4 Hz, 2H), 7.17 (s, 1H), 7.01 (dd, *J* = 8.8, 1.1 Hz, 2H), 6.92 (t, *J* = 7.3 Hz, 2H), 4.04 (s, 3H), 4.00 (s, 3H), 3.83 (t, *J* = 5.4 Hz, 4H), 3.43 (t, *J* = 5.2 Hz, 4H). ^{13}C NMR (125 MHz, $\delta_{C,}$ $CDCl_3$): 163.88, 162.54, 154.64, 153.07, 151.08, 149.17, 148.69, 129.24, 120.26, 116.26, 111.60, 107.58, 102.95, 56.25, 56.06, 49.73, 49.18. HPLC purity: 97.41%, rt: 1.946 min. ESI-MS (m/z): 351.174 $[M + H]^+$.

5.2.1.4.5. 6,7-dimethoxy-4-(4-(pyridin-2-yl)piperazin-1-yl)quinazoline (AK-05)

Yield: 69%; mp: 172-174 ^oC; R_f = 0.54 (MeOH:DCM, 3:97 v/v); α-ATR (υ cm^{-1}): 1297,1196 (Ph-O-CH_3), 978 (C-N), 1705 (C=N), 3106 (C-H, aromatic); ^1H NMR (500 MHz, $\delta_{H,}$ $CDCl_3$): 8.70 (s, 1H), 8.25 (dd, *J* = 4.9, 2.1 Hz, 1H), 7.58 – 7.52 (m, 1H), 7.35

(s, 1H), 7.18 (s, 1H), 6.76 – 6.69 (m, 2H), 4.05 (s, 3H), 4.01 (s, 3H), 3.83 (dd, *J* = 6.7, 2.6 Hz, 4H), 3.80 (dd, *J* = 6.6, 2.5 Hz, 4H). ^{13}C NMR (125 MHz, $\delta_{C,}$ $CDCl_3$): 163.89, 159.36, 154.75, 152.82, 148.80, 148.72, 147.96, 137.70, 113.92, 111.42, 107.37, 107.29, 102.95, 56.31, 56.06, 49.45, 4.17. HPLC purity: 96.89%, rt: 2.543 min. ESI-MS (m/z): 352.170 $[M + H]^+$.

5.2.1.4.6. 4-(4-(4-chlorobenzyl)piperazin-1-yl)-6,7-dimethoxyquinazoline (AK-06)

Yield: 72%; mp: 154-156 ^oC; R_f = 0.47 (MeOH:DCM, 3:97 v/v); α-ATR (υ cm^{-1}): 1252, 1156 (Ph-O-CH_3), 944 (C-N), 1667 (C=N), 3029 (C-H, aromatic); ^{1}H NMR (500 MHz, $\delta_{H,}$ $CDCl_3$): 8.63 (s, 1H), 7.19 (s, 1H), 7.08 (s, 1H), 7.06 – 7.04 (m, 2H), 6.86 – 6.84 (m, 2H), 3.96 (s, 3H), 3.92 (s, 3H), 3.74 (t, *J* = 5.2 Hz, 4H), 3.29 (t, *J* = 5.4 Hz, 4H).^{13}C NMR (125 MHz, $\delta_{C,}$ $CDCl_3$): 165.35, 156.06, 154.53, 150.60, 150.44, 150.10, 131.32, 131.22, 118.09, 113.04, 109.01, 104.41, 57.71, 57.50, 51.23, 21.90. HPLC purity: 97.21%, rt: 2.116 min. ESI-MS (m/z): 399.151 $[M + H]^+$.

5.2.1.4.7. 4-(4-(4-fluorophenyl)piperazin-1-yl)-6,7-dimethoxyquinazoline (AK-07)

Yield: 77%; mp: 169-171 ^oC; R_f = 0.49 (MeOH:DCM, 3:97 v/v); α-ATR (υ cm^{-1}): 1209, 1092 (Ph-O-CH_3), 982 (C-N), 1655 (C=N), 2934 (C-H, aromatic); ^{1}H NMR (500 MHz, $\delta_{H,}$ $CDCl_3$): 8.79 (s, 1H), 8.10 (s, 1H), 7.36 (s, 1H), 7.11 – 7.03 (m, 4H), 4.12 (s, 3H), 4.09 (s, 3H), 3.91 (t, *J* = 5.5 Hz, 4H), 3.42 (t, *J* = 5.3 Hz, 4H).^{13}C NMR (125 MHz, $\delta_{C,}$ $CDCl_3$): 163.87, 162.54, 158.43, 156.52, 154.68, 153.07, 149.19, 148.73, 147.77, 118.17, 118.11, 115.77, 115.59, 111.61, 107.60, 102.91, 56.26, 56.07, 50.20, 49.77. HPLC purity: 97.89%, rt: 2.238 min. ESI-MS (m/z): 369.165 $[M + H]^+$.

5.2.1.4.8. 4-(4-(4-fluorobenzyl)piperazin-1-yl)-6,7-dimethoxyquinazoline (AK-08)

Yield: 78%; mp: 166-168 ^{o}C; R_f = 0.58 (MeOH:DCM, 3:97 v/v); α-ATR (υ cm^{-1}): 1209, 1133 (Ph-O-CH_3), 992 (C-N), 1614 (C=N), 2958 (C-H, aromatic); ^{1}H NMR (500 MHz, $\delta_{H,}$ $CDCl_3$): 8.68 (s, 1H), 7.34 (dd, *J* = 8.4, 5.6 Hz, 2H), 7.25 (s, 1H), 7.11 (s, 1H), 7.04 (t, *J* = 8.7 Hz, 2H), 4.03 (s, 3H), 3.99 (s, 3H), 3.70 (t, *J* = 5.6 Hz, 4H), 3.58 (s, 2H), 2.66 (t, *J* = 5.3 Hz, 4H).^{13}C NMR (125 MHz, $\delta_{C,}$ $CDCl_3$): 163.81, 161.13, 154.48, 153.12, 149.17, 148.45, 133.57, 130.55, 115.24, 111.47, 107.56, 103.16, 62.26, 56.22, 52.89, 49.71. HPLC purity: 98.45%, rt: 2.279 min. ESI-MS (m/z): 383.181 $[M + H]^+$.

5.2.1.4.9. 6,7-dimethoxy-4-(4-(4-methylbenzyl)piperazin-1-yl)quinazoline (AK-9)

Yield: 80%; mp: 157-159 ^{o}C; R_f = 0.55 (MeOH:DCM, 3:97 v/v); α-ATR (υ cm^{-1}): 1206, 1133 (Ph-O-CH_3), 992 (C-N), 1615 (C=N), 2960 (C-H, aromatic); ^{1}H NMR (500 MHz, $\delta_{H,}$ $CDCl_3$): 8.68 (s, 1H), 7.29-7.25 (m, 4H), 7.18 (s, 1H), 7.16 (s, 1H), 7.11(s, 1H), 4.03 (s, 3H), 3.98 (s, 3H), 3.70 (t, *J* = 5 Hz, 4H), 3.59 (s, 2H), 2.68 (t, *J* = 5 Hz, 4H), 2.37 (s, 3H). ^{13}C NMR (125 MHz, $\delta_{C,}$ $CDCl_3$): 163.80, 154.44, 153.13, 149.14, 148.39, 136.90, 134.68, 129.16, 111.45, 107.53, 103.21, 62.83, 56.23, 56.03, 52.94, 49.72, 21.13. HPLC purity: 98.66%, rt: 2.313 min. ESI-MS (m/z): 379.206 $[M + H]^+$.

5.2.1.4.10. 6,7-dimethoxy-4-(4-methylpiperazin-1-yl)quinazoline (AK-10)

Yield: 83%; mp: 151-153 ^{o}C; R_f = 0.49 (MeOH:DCM, 3:97 v/v); α-ATR (υ cm^{-1}): 1208, 1131 (Ph-O-CH_3), 987 (C-N), 1611 (C=N), 2967 (C-H, aromatic); ^{1}H NMR (500 MHz, $\delta_{H,}$ $CDCl_3$): 8.68 (s, 1H), 7.28 (s, 1H), 7.11 (s, 1H), 4.03 (s, 3H), 4.00 (s, 3H), 3.70 (t, *J* = 5 Hz, 4H), 2.64 (t, *J* = 5 Hz, 4H), 2.40 (s, 3H).^{13}C NMR (125 MHz, $\delta_{C,}$ $CDCl_3$): 164.02, 154.80, 152.98, 149.23, 148.93, 111.73, 107.59, 102.67. HPLC purity: 98.19%, rt: 2.352 min. ESI-MS (m/z): 289.159 $[M + H]^+$.

5.2.1.4.11. 1-(4-(6,7-dimethoxyquinazolin-4-yl)piperazin-1-yl)ethan-1-one (AK-11)

Yield: 86%; mp: 138-140 ^{o}C; R_f = 0.44 (MeOH:DCM, 3:97 v/v); α-ATR (υ cm^{-1}): 1719 (C=O), 1210, 1129 (Ph-O-CH_3), 982 (C-N), 1614 (C=N), 2963 (C-H, aromatic); ^{1}H NMR (500 MHz, $\delta_{H,}$ $CDCl_3$): 8.69 (s, 1H), 7.28 (s, 1H), 7.10 (s, 1H), 4.04 (s, 3H), 4.00 (s, 3H), 3.83 (t, *J* = 5.5 Hz, 4H), 3.65 (t, *J* = 5.1 Hz, 4H), 2.18 (s, 3H). ^{13}C NMR (125 MHz, $\delta_{C,}$ $CDCl_3$): 164.02, 154.80, 152.98, 149.23, 148.93, 111.73, 107.59, 102.67. HPLC purity: 99.33%, rt: 2.662 min. ESI-MS (m/z): 317.154 $[M + H]^+$.

5.2.1.4.12. 6,7-dimethoxy-4-(4-(p-tolyl)piperazin-1-yl)quinazoline (AK-12)

Yield: 78%; mp: 132-134 ^{o}C; R_f = 0.49 (MeOH:DCM, 3:97 v/v); α-ATR (υ cm^{-1}): 1217, 1118 (Ph-O-CH_3), 974 (C-N), 1609 (C=N), 2958 (C-H, aromatic); ^{1}H NMR (500 MHz, $\delta_{H,}$ $CDCl_3$): 8.72 (s, 1H), 7.28 (s, 2H), 7.15 – 7.13 (m, 2H), 6.95 – 6.93 (m, 2H), 4.05 (s, 3H), 4.01 (s, 3H), 3.83 (t, *J* = 5.7 Hz, 4H), 3.38 (t, *J* = 5.6 Hz, 4H), 2.31 (s, 3H). ^{13}C NMR (125 MHz, $\delta_{C,}$ $CDCl_3$): 163.91, 154.62, 153.10, 149.16, 149.00, 148.66, 129.89, 129.78, 116.65, 111.61, 107.58, 102.97, 56.27, 56.07, 49.80, 20.46. HPLC purity: 99.44%, rt: 2.574 min. ESI-MS (m/z): 365.190 $[M + H]^+$.

5.2.1.4.13. 4-(4-(4-bromophenyl)piperazin-1-yl)-6,7-dimethoxyquinazoline (AK-13)

Yield: 73%; mp: 152-153 ^{o}C; R_f = 0.51 (MeOH:DCM, 3:97 v/v); α-ATR (υ cm^{-1}): 1219, 1123 (Ph-O-CH_3), 977 (C-N), 1613 (C=N), 2965 (C-H, aromatic); ^{1}H NMR (500 MHz, $\delta_{H,}$ DMSO-d_6): 8.58 (s, 1H), 8.15 (dd, *J* = 4.9, 2.0 Hz, 1H), 7.58 (ddd, *J* = 8.8, 7.1, 2.0 Hz, 1H), 7.24 (s, 1H), 7.22 (s, 1H), 6.88 (d, *J* = 8.5 Hz, 1H), 6.69 (dd, *J* = 7.0, 4.9 Hz, 1H), 3.94 (d, *J* = 2.4 Hz, 8H), 3.74 (s, 6H).^{13}C NMR (125 MHz, $\delta_{C,}$ DMSO-d_6): 172.51, 163.39, 159.40, 154.73, 152.90, 148.96, 148.62, 148.14, 113.81, 110.98, 107.62, 103.75,

56.46, 56.22, 49.29, 44.86. HPLC purity: 98.22%, rt: 2.449 min. ESI-MS (m/z): 429.085 $[M + H]^+$.

5.2.1.4.14. 6,7-dimethoxy-4-(4-(2-nitrophenyl)piperazin-1-yl)quinazoline (AK-14)

Yield: 79%; mp: 158-160 ^oC; R_f = 0.42 (MeOH:DCM, 3:97 v/v); α-ATR (υ cm^{-1}): 1317, 1192 (Ph-O-CH_3), 979 (C-N), 1581, 1389 (-NO_2), 1663 (C=N), 3113 (C-H, aromatic); ^1H NMR (500 MHz, $\delta_{H,}$ DMSO-*d*$_6$): 8.57 (s, 1H), 8.11 (d, *J* = 9.3 Hz, 2H), 7.25 (s, 2H), 7.05 (d, *J* = 9.4 Hz, 2H), 3.95 (s, 3H), 3.94 (s, 3H), 3.86 (t, *J* = 5.1 Hz, 4H), 3.74 (t, *J* = 5.2 Hz, 4H).^{13}C NMR (125 MHz, $\delta_{C,}$ $CDCl_3$): 168.44, 159.15, 157.62, 153.69, 153.53, 153.19, 134.41, 134.31, 121.18, 116.13, 112.10, 107.50, 60.80, 60.59, 54.32. HPLC purity: 97.26%, rt: 2.121 min. ESI-MS (m/z): 396.159 $[M + H]^+$.

5.2.1.5. Single crystal X-ray crystallography

Crystallographic description of compound AK-2

The SC-XRD study of compound **AK-2** was carried out to estimate various crystallographic parameters like crystal size, system, space group, orientation, molecular geometry, etc. The findings indicated that the compound **AK-2** crystal system and space group were found to be monoclinic and $P2_1/m$, respectively. The molecular packing of compound **AK-2** in a monoclinic crystal system along with its image is shown in Figure 5.32 and Figure 5.33. In compound **AK-2** (4-(4-benzylpiperazin-1-yl)-6,7-dimethoxyquinazoline), the phenyl ring A (C1/C5-C8 to C2), pyrimidine ring B (C1/C2/N1/C3/N2/C4), and benzyl ring C (C15 to C19) are planar with r.m.s. deviation of 0.0049, 0.0053, and 0.0182, respectively. The dihedral angle between the mean planes of A/B is 179.74(9)°. The bond angles at N4-C13-C14, C6-O2-C20, C7-O1-C21, and N2-C4-N3 were found to be 115.50, 120.96, 114.70, and 120.70, respectively. The SC-XRD

ORTEP diagram of compound **AK-2** is represented in Figure 5.31. The overall crystal data and structural refinement of compound **AK-2** are shown in Table 5.10.

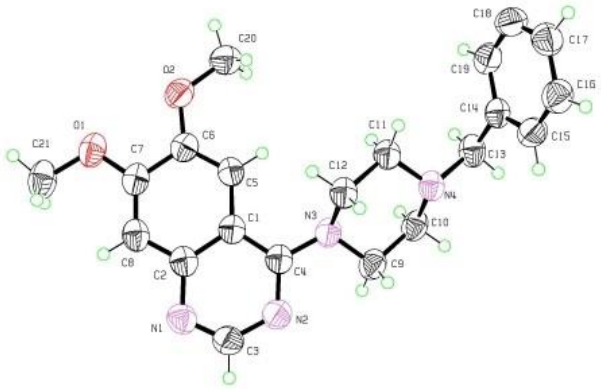

Figure 5.31. The ORTEP diagram of compound **AK-2** obtained at 100 K.

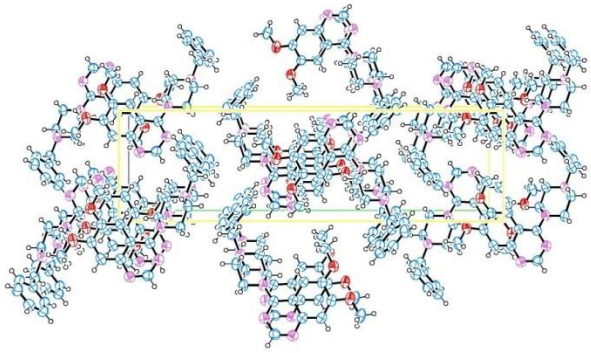

Figure 5.32. Molecular packing of compound **AK-2** in monoclinic crystal system.

Figure 5.33. Crystal image of compound **AK-2** during SC-XRD analysis.

Table 5.10. Crystal data and structure refinement for **AK-2**

Identification code	**AK-2**
Empirical formula	$C_{21}H_{24}N_4O_2$
Formula weight	364.44

Temperature/K	100
Crystal system	monoclinic
Space group	$P2_1/m$
a/Å	7.65098(13)
b/Å	29.4566(6)
c/Å	8.46828(18)
α/°	90
β/°	93.6778(18)
γ/°	90
Volume/Å^3	1904.58(6)
Z	4
ρ_{calc}g/cm^3	1.271
μ/mm^{-1}	0.673
F(000)	776.0
Crystal size/mm^3	0.3 × 0.114 × 0.091
Radiation	Cu Kα (λ = 1.54184)
2Θ range for data collection/°	6 to 144.142
Index ranges	$-9 \leq h \leq 7$, $-36 \leq k \leq 36$, $-10 \leq l \leq 10$
Reflections collected	21496
Independent reflections	3837 [R_{int} = 0.0341, R_{sigma} = 0.0240]
Data/restraints/parameters	3837/0/161
Goodness-of-fit on F^2	4.999
Final R indexes [I>=2σ (I)]	R_1 = 0.3776, wR_2 = 0.7801
Final R indexes [all data]	R_1 = 0.3987, wR_2 = 0.8042
Largest diff. peak/hole / e Å^{-3}	2.34/-1.79
CCDC No.	2335291

5.2.2. Pharmacology

5.2.2.1. In-vitro studies

5.2.2.1.1. ChE inhibition experiment

To investigate the inhibitory activity and selectivity index of the designed compounds, the hAChE and hBChE enzyme inhibition assay was conducted *via* Ellman's method using rivastigmine and donepezil as reference compounds [Ellman et al. 1961]. The outcomes of the enzymatic inhibition experiments are listed in Table 5.11. The SAR was established by introducing various substituted piperazines at the C4 position of quinazoline moiety (Figure 5.35). The results demonstrated moderate to good inhibition

of hAChE at concentrations between the micromolar and sub-micromolar range. The introduction of methyl and acetyl groups at piperazine exhibited a lower inhibitory profile against hAChE (**AK-10,** IC_{50}: 1.275 μM; and **AK-11,** IC_{50}: 1.192 μM). Replacing these groups with lipophilic and aromatic phenyl or pyridinyl rings didn't affect the hAChE inhibitory activity as much (**AK-4,** IC_{50}: 1.006 μM; **AK-5,** IC_{50}: 1.148 μM). The para-substitution of variable electron-releasing group (ERG) like methyl group at phenyl ring (**AK-12,** IC_{50}: 1.171 μM) further lowered the inhibitory profile as compared to the electron-withdrawing groups (EWG_s) like $–NO_2$, –Br and –F (**AK-3,** IC_{50}: 0.481 μM; **AK-13,** IC_{50}: 0.973 μM; **AK-7,** IC_{50}: 1.038 μM). The concomitant modification by introducing one carbon methylene group in between the piperazine and phenyl ring increases the hAChE inhibitory activity (**AK-2,** IC_{50}: 0.283 μM). Substitution of methyl group at the para-position of the benzyl ring reduces the inhibitory activity (**AK-9,** IC_{50}: 1.024 μM) as compared to the EWGs groups like –Cl and –F groups (**AK-6,** IC_{50}: 0.921 μM; **AK-8,** IC_{50}: 0.932 μM). Further, the introduction of the diphenylmethylene group on the piperazine moiety increased the inhibitory potential against hAChE which may be due to the enhanced lipophilicity imparted by the diphenylmethylene group (**AK-1,** IC_{50}: 0.436 μM). Overall, the compound **AK-2** showed good inhibitory activity due to its optimum conformational flexibility and optimum binding profile with the active site residues of AChE (**AK-2,** IC_{50}: 0.283 μM). The *in-vitro* activity of the compounds was compared with the reference compound donepezil (IC_{50}: 0.043 μM) against hAChE.

Additionally, several research suggested that hBChE is crucial for the ACh regulation and the preservation of regular cholinergic activities in AD and it was perceived to be increased in AD [Mesulam et al. 2002]. Hence, combined inhibition of hAChE and hBChE can be thought of as a potential therapeutic benefit in late-stage and severe AD states. All the synthesized compounds were also screened for hBChE inhibitory activity

which demonstrated IC_{50} >10 μM. The hBChE activity as compared to the standard rivastigmine (IC_{50}: 1.1 μM).

Table 5.11. Inhibitory profile of the synthesized compounds (**AK-1** to **AK-14**) against hChE and hBACE-1 enzymes.

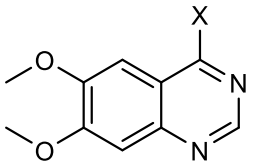

Comp. Code	**X**	**IC_{50} (μM) ± SEM[a]**		
		hAChE	**hBChE**	**hBACE-1**
AK-1	Benzhydryl piperazine	0.436 ± 0.082	>10	0.662 ± 0.078
AK-2	Benzyl piperazine	0.283 ± 0.015	>10	0.231 ± 0.049
AK-3	4-NO_2 phenyl piperazine	0.481 ± 0.027	>10	0.729 ± 0.086
AK-4	Phenyl piperazine	1.006 ± 0.014	>10	1.314 ± 0.070
AK-5	Pyridyl piperazine	1.148 ± 0.035	>10	1.561 ± 0.062
AK-6	4-Cl benzyl piperazine	0.921 ± 0.018	>10	1.652 ± 0.086
AK-7	4-F phenyl piperazine	1.038 ± 0.025	>10	1.47 ± 0.071
AK-8	4-F benzyl piperazine	0.932 ± 0.095	>10	2.925 ± 0.059
AK-9	4-methyl benzyl piperazine	1.024 ± 0.045	>10	1.432 ± 0.057
AK-10	4-methyl piperazine	1.275 ± 0.010	>10	3.28 ± 0.074
AK-11	4-acetyl piperazine	1.192 ± 0.035	>10	3.66 ± 0.052
AK-12	4-methyl phenyl piperazine	1.171 ± 0.056	>10	1.881 ± 0.078
AK-13	4-Br phenyl piperazine	0.973 ± 0.033	>10	1.714 ± 0.015

AK-14	2-NO_2 phenyl piperazine	0.914 ± 0.046	>10	1.816 ± 0.094
Donepezil	-	0.043 ± 0.01	1.4 ± 0.08	0.227 ± 0.013
Rivastigmine	-	2.288 ± 0.031	1.1 ± 0.04	nd

a – Findings are reported as the mean IC_{50} ± SEM (n = 3);

nd- Not-determined;

5.2.2.1.2. Enzyme kinetics study on hAChE

An enzyme kinetic study against hAChE was carried out to investigate the inhibition mechanism of the most promising compound **AK-2**. The Lineweaver-Burk double reciprocal plot between the substrate's initial velocities (y-axis) at increasing concentrations (x-axis; ATCI) was used to determine the mode of inhibition. The Lineweaver-Burk plot and Michaelis-Menten graph findings showed the mixed type of inhibition as substrate concentrations were raised, V_{max} decreased but K_m remained constant which indicated that compound **AK-2** inhibited both the free enzyme and the enzyme-substrate complex non-competitively. Since the intersection points of the 1/Vmax and 1/[S] axes were both greater than zero, it can be concluded that the inhibitor was more frequently associated with free enzymes than with complexes of enzymes and substrates (Figure 5.34A and B). The Dixon plot was built between the Lineweaver−Burk slope and the inhibitor concentration revealing that the point of interaction at the x-axis indicated inhibition constant (K_i) for compound **AK-2** which was found to be 0.246 µM (Figure 5.34C).

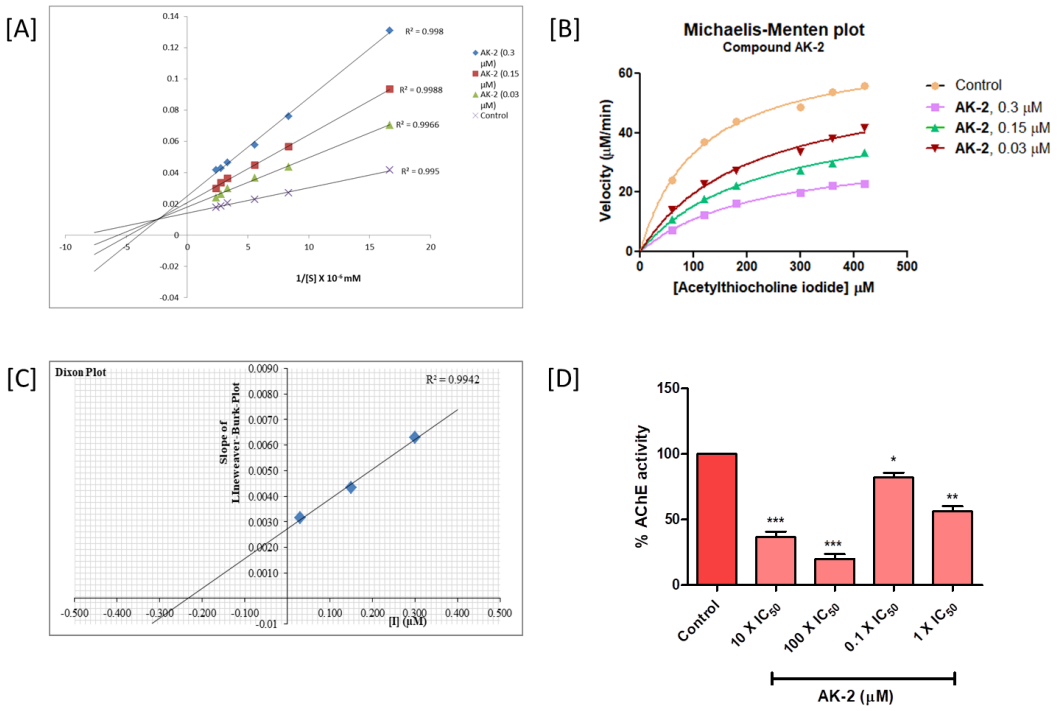

Figure 5.34. Enzyme kinetics studies of compound **AK-2** [A] Lineweaver-Burk plot, [B] Michaelis-Menten plot, and [C] Dixon plot, [D] Enzyme reversibility study. Findings are reported as the mean IC_{50} ± SEM (n = 3). *p < 0.05, **p < 0.01, and ***p < 0.001 vs control. One-way ANOVA followed by Newman-Keuls Multiple Comparison test.

5.2.2.1.3. Enzyme reversibility inhibition study

Irreversible types of drugs for example tacrine and physostigmine result in several adverse effects and toxicity [Colovic et al. 2013]. Therefore, one of the crucial factors to be determined is the reversible binding nature of the designed compound which was examined for most active compound **AK-2**. The reversibility inhibition assay showed that under the influence of compound **AK-2,** the enzymatic activity of hAChE was decreased to a minimum at concentrations of 10 and 100 times the IC_{50} of **AK-2**. Additionally, after being diluted 100 times with Acetylthiocholine iodide, the enzymatic activity was restored to > 60% as depicted in Figure 5.34D.

5.2.2.1.4. hBACE-1 inhibition study

The FRET-based fluorometric experiment was executed to assess the inhibition profile of designed derivatives against hBACE-1 using donepezil as a reference. Table 5.11 provides an overview of the hBACE-1 inhibition assay results. The results demonstrated moderate to good inhibition against hBACE-1 at concentrations in the range of micromolar to sub-micromolar range. The introductions of 1-methyl and 1-acetyl group on piperazine ring attached to quinazoline scaffold have shown lower hBACE-1 inhibitory activity (**AK-10,** IC_{50}: 3.28 μM; and **AK-11,** IC_{50}: 3.66 μM). The unsubstituted, pyridinyl and substituted phenyl piperazines with both EWGs and ERGs groups exhibited moderate hBACE-1 inhibition (**AK-4,** IC_{50}**:** 1.314 μM; **AK-5,** IC_{50}**:** 1.561 μM; **AK-7,** IC_{50}**:** 1.47 μM; **AK-12,** IC_{50}**:** 1.881 μM; **AK-13,** IC_{50}**:** 1.714 μM; and **AK-14,** IC_{50}**:** 1.816 μM) (**Table 1**). The substituted benzyl piperazine with both EWGs and ERG also produced moderate hBACE-1 inhibition (**AK-6,** IC_{50}: 1.652 μM; **AK-8,** IC_{50}: 2.925 μM; and **AK-9,** IC_{50}: 1.432 μM). The benzhydryl piperazine, benzyl piperazine, and 4-NO_2 phenyl piperazine-containing compounds exhibited significant hBACE-1 inhibition with IC_{50} in a submicromolar range amongst the synthesized compounds (**AK-1:** 0.662 μM; **AK-2:** 0.231 μM, and **AK-3:** 0.729 μM). Our findings suggested that the introduction of a carbon chain linker improves the interaction with aspartate dyad residues (Asp32 and Asp228) of hBACE-1. Based on *in-vitro* hAChE and hBACE-1 inhibition data compounds **AK-1, AK-2,** and **AK-3** were selected as MTDLs and considered to be investigated further. Moreover, the compound **AK-2** showed good hBACE-1 inhibitory activity (IC_{50}: 0.231 μM) as compared to the previously reported compound **AV-2** (IC_{50}: 0.254 μM). The overall SAR of the designed series against hAChE and hBACE-1 was represented in Figure 5.35.

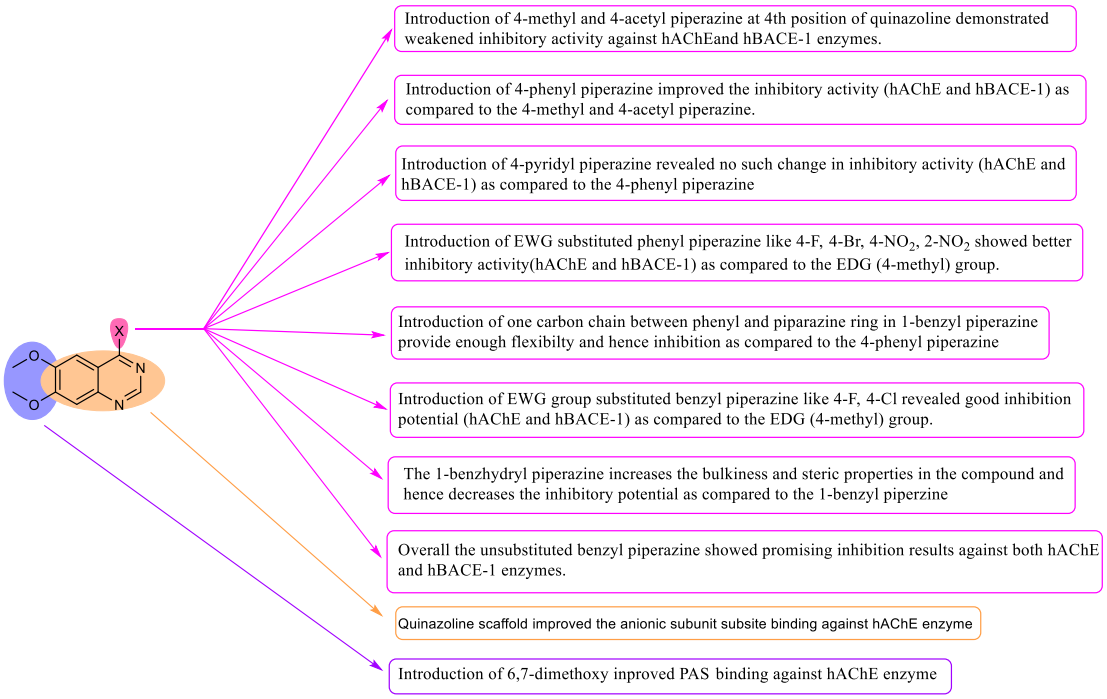

Figure 5.35. SAR of designed series against hAChE and hBACE-1 enzymes.

5.2.2.1.5. PAMPA-BBB assay

The primary challenge with drugs developed for AD treatment is to cross BBB. Following the procedure described by Di et al., the PAMPA-BBB experiment was performed to investigate the partitioning of the compounds (**AK-1**, **AK-2**, and **AK-3**) across BBB [Di et al. 2003]. The assay was based on the passive diffusion of the compound from the donor to the acceptor region of the microplate via an artificial porcine brain lipid membrane. The correlation between experimental $Pe_{(exp)}$ and reference permeability $P_{e(ref)}$ was determined using the permeability of nine commercial medicines as discussed in our previously reported work [Waiker et al. 2023c]. According to the CNS permeability cut-off values, substances with permeability (P_e) values greater than 4.78×10^{-6} cm s^{-1} were considered to be outstanding brain permeation, whereas substances with P_e values less than 1.82×10^{-6} cm s^{-1} were reflected to be poor brain permeation. While the permeability in between these values demonstrates uncertainty in BBB permeation properties. The findings of assay indicated that all tested derivatives possessed good BBB

permeability as shown in Table 5.12. Amongst them, the compound **AK-2** demonstrated better BBB permeability as compared to the previously reported compound **AV-2** (P_e = 5.82 ± 0.26 ×10^{-6} cm s^{-1}).

5.2.2.1.6. PI displacement assay

Using the protocol described by Taylor et al., the PI displacement assay was performed for the selected compounds to confirm the effective binding of selected compounds with AChE-PAS [TAYLOR et al. 1974]. The PI is a standard florescent ligand that binds selectively with AChE-PAS and exhibits approximately 10 times increase in fluorescence intensity *in-vitro*. The proportion of PI displacement from AChE-PAS in the presence of 10 and 50 μM inhibitor concentrations was used to calculate fluorescence intensity. The results indicated that at the tested compound concentration, compound **AK-2** has significantly displaced PI from the PAS active site of AChE (**AK-2:** 10 μM: 20.42 %, 50 μM: 28.85 %) and was found comparable to the donepezil (10 μM: 23.07 %, 50 μM: 32.11 %) (Table 5.12).

Table 5.12. The PAMPA-BBB permeability and PI displacement assay for screened derivatives **AK-1** to **AK-3**.

Comp.	**PAMPA-BBB permeability**		**PI displacement from AChE-PAS (% inhibition)[b]**	
	$P_{e(exp)}$ (10^{-6} cm s^{-1})	**Permeability prediction[a]**	**10 μM Conc.**	**50 μM Conc.**
AK-1	6.28 ± 0.10	CNS+	17.6 ± 1.8	25.3 ± 1.7
AK-2	6.03 ± 0.48	CNS+	20.4 ± 1.5	28.9 ± 1.2
AK-3	4.81 ± 0.09	CNS+	14.2 ± 2.4	21.5 ± 2.1
Donepezil	6.53 ± 0.13	CNS+	23.0 ± 1.4	32.1 ± 1.3

[a] 'CNS+' indicated good BBB permeation; [b] Findings are reported as the mean

IC_{50} ± SEM (n = 3).

5.2.2.1.7. Aβ aggregation inhibition by Thioflavin T assay

The accumulation and aggregation of Aβ can be considered as one of the primary risk factors for AD [Chen et al. 2017]. The findings of the PI displacement assay demonstrated the ability of compound **AK-2** to bind with hAChE-PAS. PAS inhibition plays a crucial role in both AChE inhibiting and hence preventing Aβ aggregation [Rees et al. 2003]. Additionally, compound **AK-2** was found to have a potential hBACE-1 inhibitory profile. All these findings compelled us to test compound**'s** (**AK-2**) ability to prevent Aβ aggregation using the self- and hAChE-induced thioflavin T assay. The results indicated that Aβ aggregation inhibition was concentration-dependent and the highest Aβ aggregation inhibition activity for **AK-2** was observed at a 20 μM (Aβ:inhibitor, 10:20 μM) concentration. The compound **AK-2** showed balanced Aβ inhibition (self-induced: 27.30−56.11%; hAChE-induced: 51.99−62.88%) as compared to the curcumin (self-induced: 29.85−61.78%) and donepezil (hAChE-induced: 34.29−61.65%) (Figure 5.36 and Figure 5.37). To check whether this decrease in the NFI on the addition of the compound **AK-2** in a dose-dependent manner is due to the Aβ aggregation inhibition property of the compound **AK-2** or displacement of ThT by the inhibitor, the interference with ThT assay was performed by measuring the spectral scan of excitation, emission of compound **AK-2** (with or without inhibitor) from 450 nm to 700 nm range. The findings demonstrated that the decrease in the fluorescence intensities was dose-dependent (Figure 5.38). To substantiate the above findings microscopic studies including AFM and confocal studies were also performed. The Aβ aggregation inhibition results confirmed that the inhibitor has access to the AChE-PAS region which also corroborated our *in-vitro* hAChE, hBChE, and hBACE-1 assay.

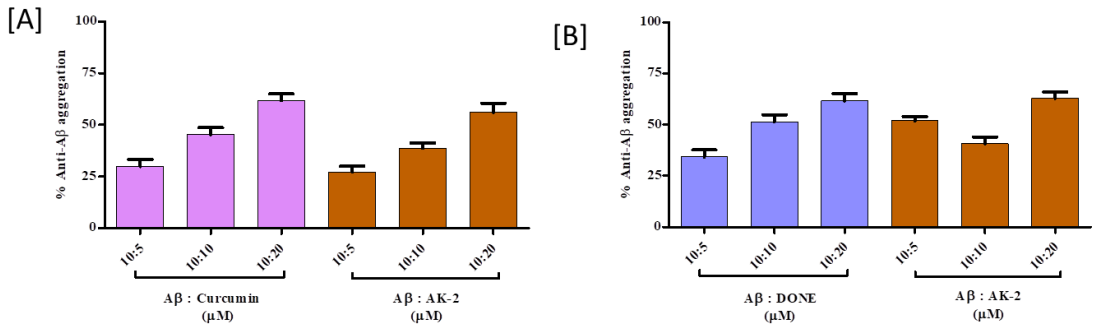

Figure 5.36. Thioflavin T assay of compound **AK-2**, [A] self-induced Aβ aggregation inhibition, [B] AChE-induced Aβ aggregation inhibition.

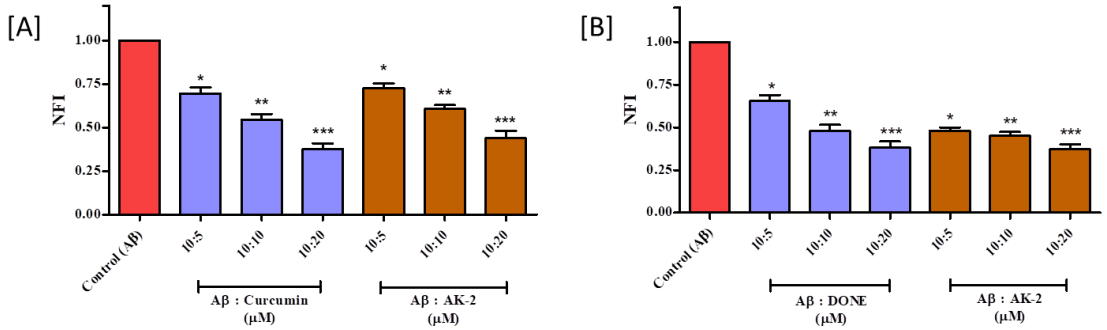

Figure 5.37. Thioflavin T assay of compound **AV-2**. [A] self-induced Aβ aggregation inhibition, [B] hAChE-induced Aβ aggregation inhibition. Findings are reported as the mean IC_{50} ± SEM (n = 3). *p < 0.05, **p < 0.01, and ***p < 0.001 vs control, ns = non-significant. One-way ANOVA followed by Newman-Keuls Multiple Comparison test.

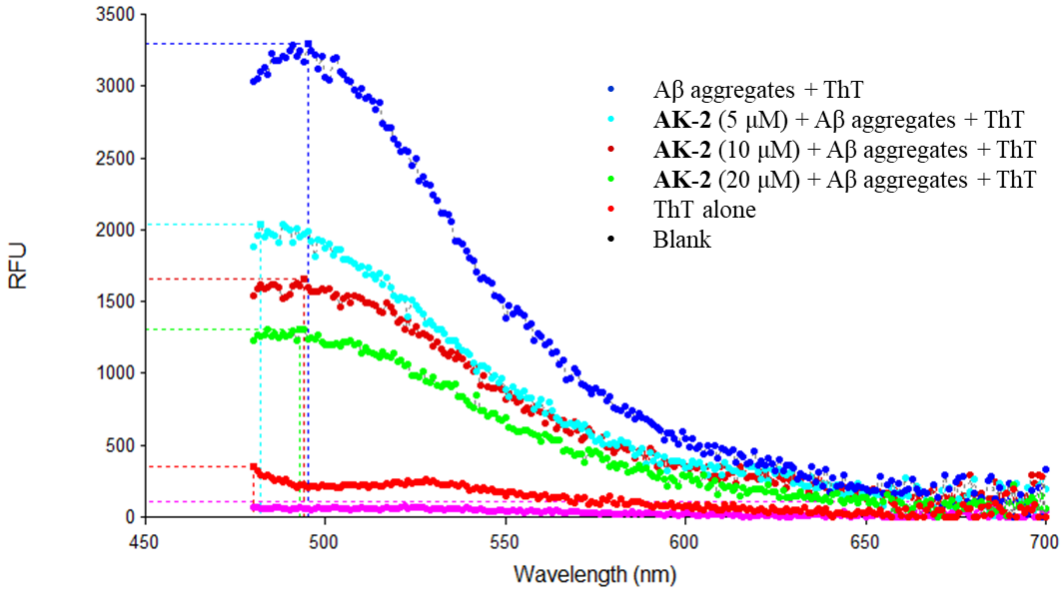

Figure 5.38. Thioflavin T experiment of compound **AK-2** showed reduced fluorescence intensity.

5.2.2.1.8. Microscopic (AFM and confocal) studies

To confirm the Aβ-inhibitory profile of compound **AK-2** during the incubation period of six days at various time points the AFM analysis was executed in which the surface topographical maps for Aβ with and without inhibitor were observed [Waiker et al. 2023b]. A microscopic morphological evaluation of the development of Aβ clumps, fibrils, and large oligomers was observed using AFM. A three-day incubation of $A\beta_{1-42}$ alone produces massive oligomers and fibrils (Figure 5.39, Panel A2) which were decreased significantly as a result of the addition of compound **AK-2** and curcumin, and finally stopped the aggregation of $A\beta_{1-42}$ (Figure 5.39, Panel A3 & 4). The results of the AFM experiment also proved that Aβ aggregation inhibition is due to the properties of the compound **AK-2**.

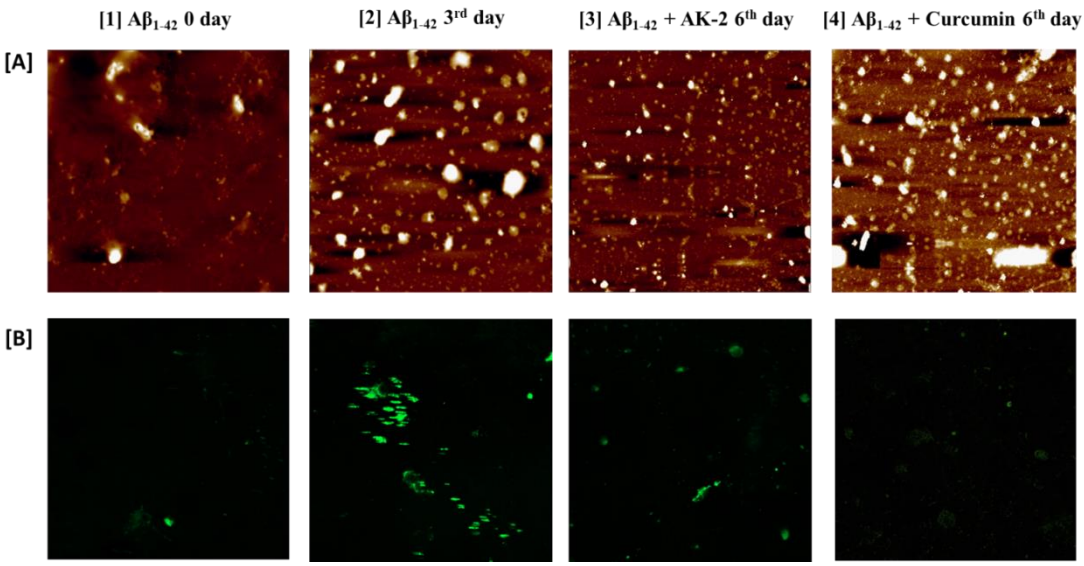

Figure 5.39. [A] AFM and [B] confocal microscopic studies of Aβ aggregation inhibition potency of compound **AK-2** and curcumin at various time intervals.

The confocal microscopic images were also captured in the presence and absence of inhibitors using Aβ aggregates staining dye. The results indicated that the full conversion of Aβ monomers to oligomers on 3rd day showed maximum fluorescence intensity as compared to the Aβ monomers on day 0 (Figure 5.39, Panel B2). The addition of compound **AK-2** leads to the disaggregation of Aβ and hence decreased fluorescence intensity on the 6th day of the study (Figure 5.39, Panel B3). The observations suggested that compound **AK-2** possesses Aβ disaggregation ability and is comparable to the standard curcumin (Figure 5.39B).

5.2.2.1.9. Neurotoxicity study of compound AK-2 on RA/BDNF differentiated SH-SY5Y cell lines

The retinoic acid (RA) and brain-derived neurotrophic factor (BDNF) cultured SH-SY5Y cells were used to study the neurotoxic potential of target compound **AK-2**. The RA and BDNF differentiated SH-SY5Y neuroblastoma cell lines have longer processes, polarized cell bodies, and neurite-like structures thus giving exact neuronal cell (axon and neurite-

outgrowth) similarity whereas undifferentiated SH-SY5Y cells grow in clusters, and have short, and truncated processes [Şahin et al. 2021]. The MTT results after incubation of SH-SY5Y cell lines with compound **AK-2** showed that there was a 26% reduction in cell viability at the maximum concentration of compound **AK-2** (80 μM) as compared to the control and statistically nonsignificant reduction in cell viability as compared to the donepezil. The findings demonstrated that the compound **AK-2** has non-neurotoxic properties and could be considered for more preclinical evaluations (Figure 5.40A).

5.2.2.1.10. Neuroprotective study of compound AK-2 on RA/BDNF differentiated SH-SY5Y cell lines

A cell viability study based on the MTT assay was carried out to investigate the cell rescue properties of **AK-2** in $A\beta_{1-42}$ treated SH-SY5Y cells. $A\beta_{1-42}$ (10 μM) monomers were incubated with the SH-SY5Y cell lines for 24 h, after which the culture media was changed by adding standard donepezil and compound **AK-2** and then observed the cell viability by MTT experiment after 48 and 72 h. The findings showed that the cells treated with compound **AK-2** recovered the cell viability to 75% and 80% after 48 and 72 h, respectively. The results also indicated that the cell viability of compound **AK-2** was found to be statistically significant as compared with the cell treated with Aβ alone ($^{\pi}p < 0.05$ vs Aβ (48 hr); $^{\#}p < 0.05$ and $^{\#\#}p < 0.01$ vs Aβ (72 hr)) and was also found comparable to the standard donepezil (rescued cell viability 68% and 79% after 48 and 72 h, respectively) (Figure 5.40 B).

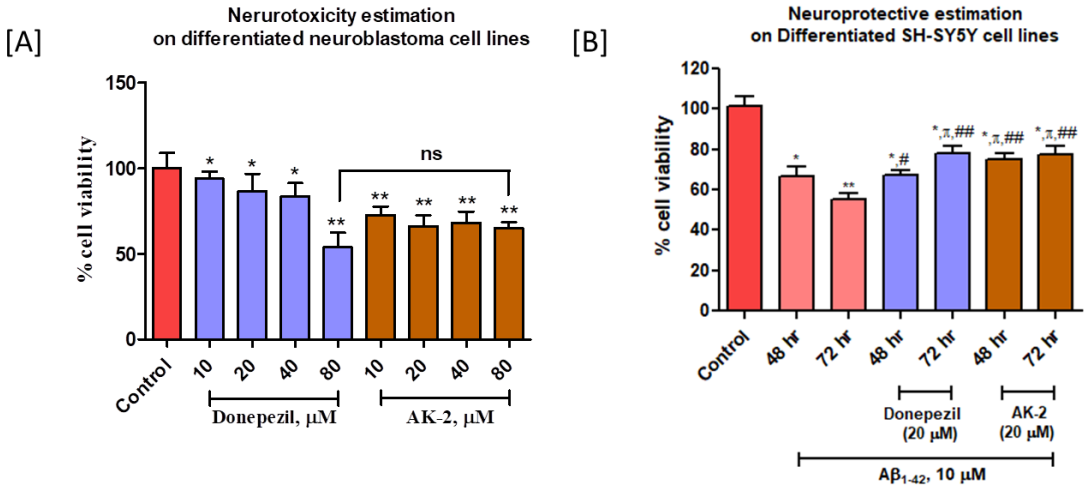

Figure 5.40. Cell culture studies of compound **AK-2** on RA/BDNF differentiated SH-SY5Y cell lines. [A] Neurotoxicity; [B] Neuroprotective analysis. Findings are reported as mean ± SEM (n=3). **p* < 0.05 and ***p* < 0.01 vs control; $^{\pi}$p < 0.05 vs Aβ (48 hr); $^{\#}$p < 0.05 and $^{\#\#}$p < 0.01 vs Aβ (72 hr); ns = non-significant. One-way ANOVA followed by Newman-Keuls Multiple Comparison test.

5.2.2.2. In-vivo and *ex-vivo* studies

5.2.2.2.1. Acute toxicity studies

The acute toxicity of compound **AK-2** was performed on female Wistar rats as per the guidelines of OCED 423. The doses of 100-500 mg/kg p.o. of compound **AK-2** were given and the animals were observed for 14 days. It was observed that there were no signs of toxicity or adverse side effects during the study period. Nevertheless, up to five days, a minor weight loss was seen in the **AK-2** treatment animal group. However, during the trial, their weight was eventually gained back. The renal and hepatic functional parameters were observed to be within the prescribed limits. Post-experiment, various major organs such as kidneys, heart, liver, and brains were histopathologically examined and found with normal tissue appearance (Figure 5.41 and Table 5.13). Therefore, it could be stated that compound **AK-2** possessed a substantial margin of safety and is safe to be utilized for further *in-vivo* investigations.

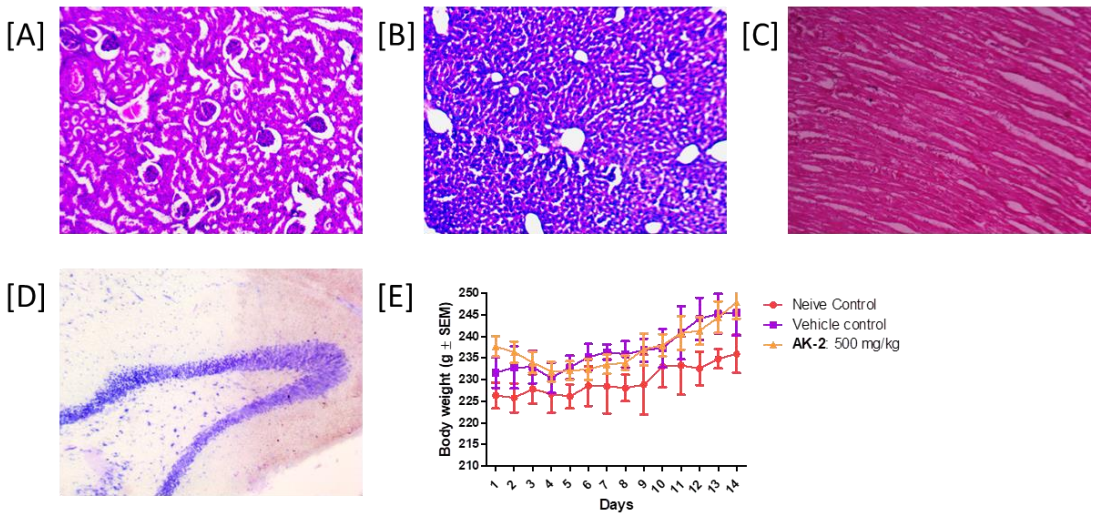

Figure 5.41. Histopathological examination of the different animal organs via H & E staining after acute toxicity studies; [A] Kidney tissue showing normal DCT, PCT and Glomerulus; [B] Liver tissue showing the presence of normal Kupfer cells; [C] Heart slice showing normal cardiac muscles; [D] brain tissue showing normal hippocampus and cortex after crystal violet staining; [E] change in body weight up to 14 days.

Table 5.13. Liver and kidney function test of experimental animals under acute toxicity studies.

Parameters	**Control (±SD)**	**100 mg/kg (±SD)**	**300 mg/kg (±SD)**	**500 mg/kg (±SD)**
AST (IU/L)	129 ± 11.6	136 ± 10.2	146 ± 15.6	153 ±11.5
ALT (IU/L)	37 ± 3.4	40 ± 2.8	44 ± 4.2	51 ± 4.5
ALP (IU/L)	42 ± 1.8	57 ± 2.1	68 ± 1.4	81 ± 2.8
Creatinine (mg/dL)	0.51 ± 0.04	0.57 ± 0.09	0.64 ±0.05	0.72 ± 0.03

5.2.2.2.3. Aβ-induced water maze test

Aβ formation and their aggregation in the neuronal synaptic region of the brain is the main pathophysiological hallmark responsible for AD progression. These Aβ aggregates or plaques are generated under the influence of the over-activation of the BACE-1

enzyme which cleaves APP through the amyloidogenic pathway [Sathya et al. 2012]. To assess the learning and memory alterations, the Aβ-induced water maze test was carried out. The $A\beta_{(1-42)}$ (4 μM, 5 μL) was injected stereotaxically *via* intercerebrovascular (ICV) into all the experimental animals except the sham group and kept them undisturbed for 7 days with normal food and water supply [Chambon et al. 2011]. On the 7^{th} day, the treatment with compound **AK-2** (20 mg/kg) and donepezil (5 mg/kg) was started in their respective experimental groups for 9 days. The control group animals received only vehicles. From the last 5 days of treatment, the Morris water maze test was conducted for 90 sec on all the experimental groups to determine the escape latency time (ELT) and total platform crossing. Overall results indicated that the Aβ diseased model group showed extended ELT and lowered total platform crossing as compared to the control group which indicated cognitive impairment induction ($^{a}p < 0.05$). After treatment with compound **AK-2**, the ELT was found to be decreased and an increased total platform crossing as compared to the diseased model group ($^{b}p < 0.05$). Moreover, the results of the compound **AK-2** treatment group revealed statistical significance as compared to the diseased model group and non-significant results as compared to the donepezil-treated group (Figure 5.42). The overall Aβ-induced behavioral rat model study suggested that compound **AK-2** has retrieved cognitive deficiencies probably by inhibiting BACE-1 activity and hence acted as an anti-Aβ agent at its tested doses.

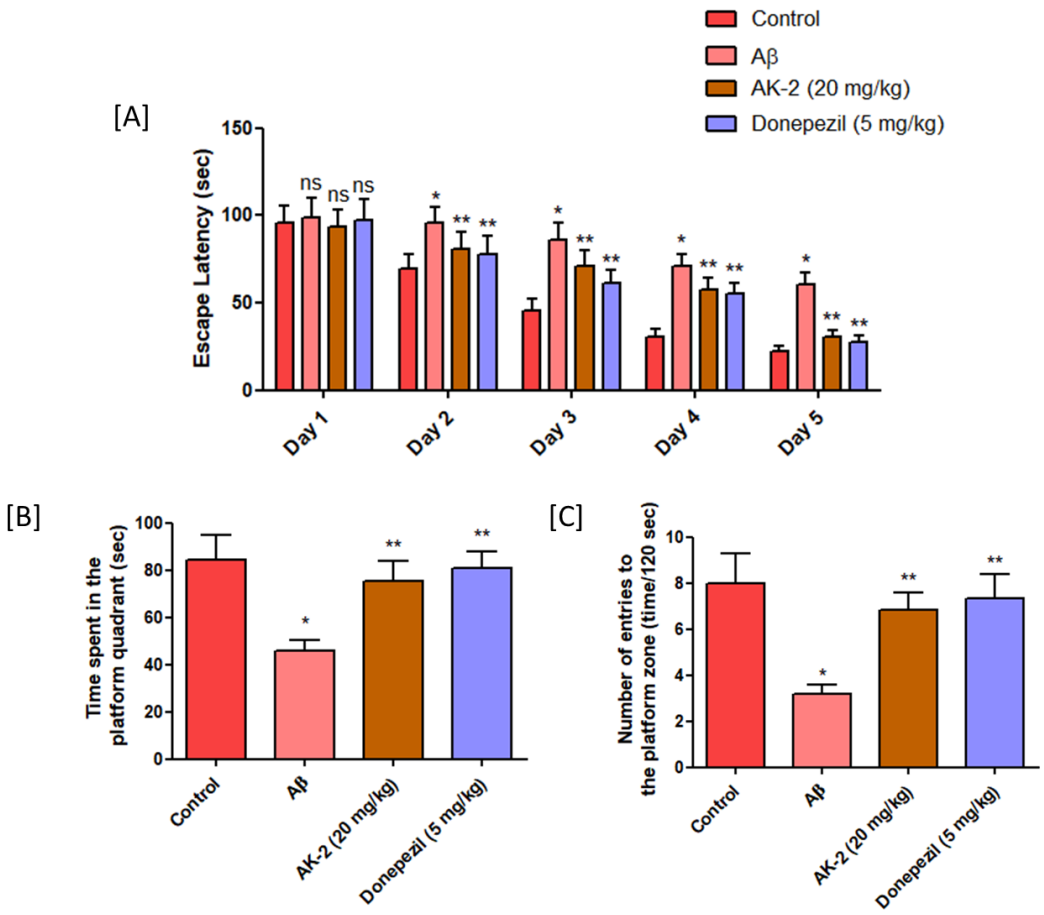

Figure 5.42. *In-vivo* efficacy of compound **AK-2** *via* $A\beta_{1-42}$ induced Morris water maze test: [A] escape latency determination; Two-way ANOVA followed by Bonferroni posttest. [B] Time spent on the platform quadrant; and [C] number of entries to the platform zone. $^{*}p < 0.05$ vs control and $^{**}p < 0.05$ vs Aβ. One-way ANOVA followed by Newman-Keuls Multiple Comparison test.

5.2.2.2.4. Ex-vivo immunohistochemistry analysis

The cryo-sectioned tissues of hippocampal brains of sham, Aβ disease model, **AK-2** treated, and donepezil grouped animals were further subjected to immunohistochemical analysis to investigate the levels of Aβ and BACE-1. The IHC analysis findings suggested that the levels of Aβ and BACE-1 were significantly ($^{***}p < 0.001$) increased in the Aβ disease model as compared to the sham group. However, after treatment with the compound **AK-2,** there was a significant ($^{***}p < 0.001$) decrease (Figure 5.43B & C) as compared to the Aβ diseased model group. On the other hand, both BACE-1 and Aβ

levels were found non-significant as compared to the standard donepezil-treated group (Figure 5.43B & C).

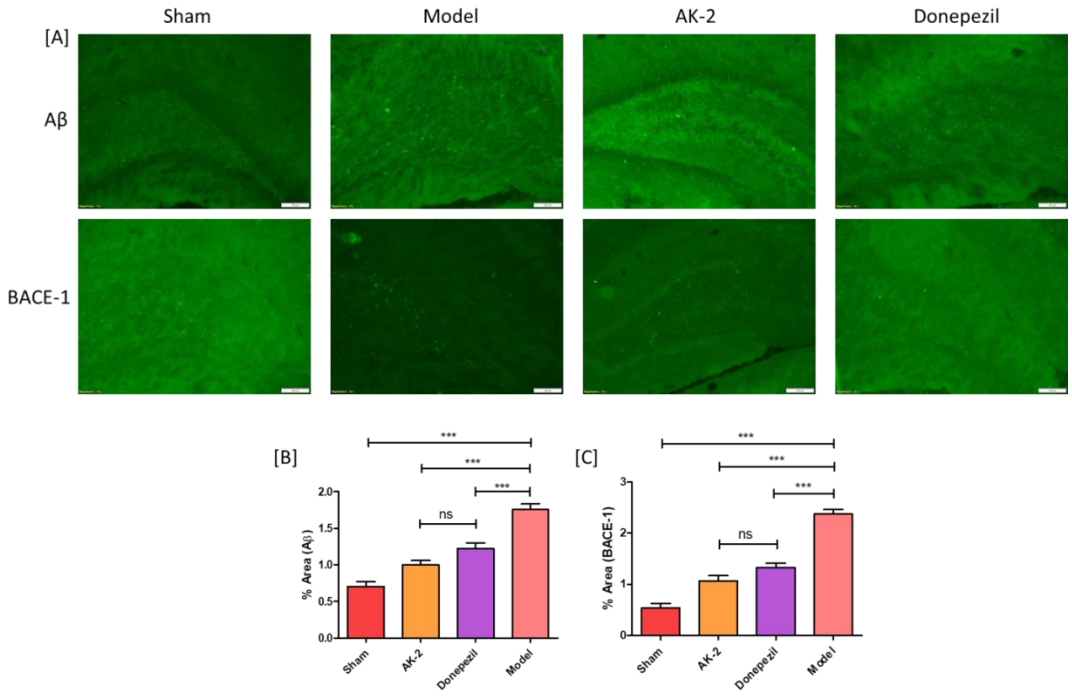

Figure 5.43. IHC analysis for investigating the levels of Aβ and BACE-1: [A] Representing IHC images of different experimental groups; [B] Histogram representing Aβ level; [C] Histogram representing BACE-1 level. $^{***}p < 0.001$ vs Model; ns = non-significant. Findings are reported as mean ± SEM (n=3). One-way ANOVA followed by Newman-Keuls Multiple Comparison test.

5.2.2.2.5. Brain tissue histopathology

After successfully conducting an Aβ-induced Morris water maze experiment, histopathology examination of the brain from each group was performed using Nissl staining. The various parameters such as integrated density, morphological characteristics, and % neuronal cells were determined. After staining, microscopical examination of the hippocampal section of $A\beta_{1\text{-}42}$ group rats showed decreased % neuronal density with disorganized neuronal arrangement as compared to the control group. The % neuronal density and neuronal arrangement were increased in the animals

treated with **AK-2** (20 mg/kg) and donepezil (5 mg/kg) as compared to the $A\beta_{1-42}$ group. However, the % neuronal density in the **AK-2** (20 mg/kg) group was found to be statistically non-significant as compared to the donepezil (5 mg/kg) group (Figure 5.44).

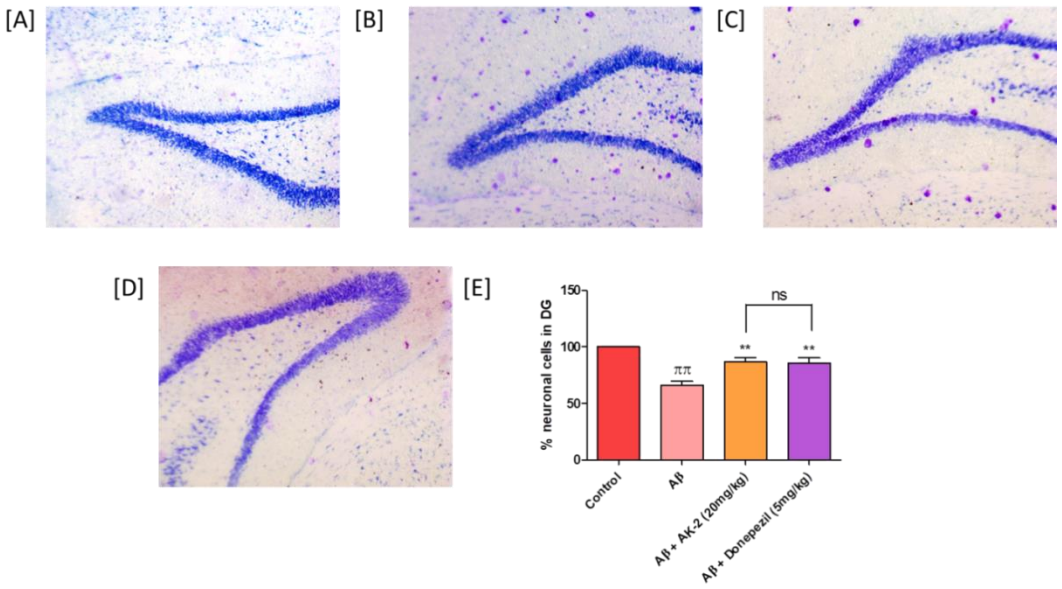

Figure 5.44. Histopathological examination of brain hippocampal (Dentate gyrus DG): [A] control, [B] Aβ-treated, [C] Aβ+**AK-2**-treated, [D] Aβ+Donepezil-treated [E] % neuronal density in DG with respect to control. $^{\pi\pi}p < 0.01$ vs control; $^{**}p < 0.01$ vs Aβ treated.

5.2.2.2.6. Drosophila phenotypic model

In AD progression, the build-up of $A\beta_{42}$ fibrils is strongly associated with memory impairment and neuronal damage, as evidenced by several studies [Deolankar et al. 2022, Deshpande et al. 2023, Prüßing et al. 2013]. The expression of UAS (Upstream Activation Sequence)-Aβ driven by ey-GAL4 (activator gene) effectively induces AD-like symptoms by neurodegeneration in *Drosophila*, as demonstrated by Chauhan et al [Chauhan et al. 2022]. This study aimed to investigate the potential antioxidant and neuroprotective properties of the compound **AK-2**, specifically its impact on the eye phenotype of a *Drosophila* model expressing $A\beta_{42}$, which correlates with AD. Our

findings indicate that compound **AK-2** may mitigate the complications caused by $A\beta_{42}$ fibrils in this AD *Drosophila* model.

5.2.2.2.6.1. Compound AK-2 toxicity analysis

Initially, the toxicity analysis of compound **AK-2** was performed. We evaluated different **AK-2** dosages (1, 10, 50, 100, and 200 µM) on Oregon R+ flies to determine the safest and most effective concentration. The results indicated that in F1 progeny there was a statistically non-significant reduction in the % eclosed flies up to 50 µM concentration. However, there was a significant reduction in the % eclosed flies at 100 (65% toxicity at the pupal stage, $^{**}p < 0.01$) and 200 µM (100% toxicity at the embryonic stages, $^{***}p < 0.001$) concentrations as compared to the control (Figure 5.45A) which indicated that **AK-2** could be affecting critical developmental processes in the flies, with more prominent effects at higher doses and doses up to 50 µM were considered to be non-lethal.

5.2.2.2.6.2. Cell viability of AK-2 in AD flies

Conducting an MTT assay on the gut tissue of *Drosophila*, when neurodegeneration is induced by Aβ deposition in the eyes, is indeed possible. The MTT assay is versatile and can be used to assess cell viability in various tissues, including the gut. This could provide insights into the systemic effects of Aβ toxicity beyond the nervous system [Mukherjee and Mishra 2020, Priyadarsini et al. 2020]. Therefore, while the primary focus might be on the eyes for Aβ deposition, analyzing the **AK-2**-treated gut tissue with an MTT assay could provide a more comprehensive understanding of the impact of **AK-2** treatment on Aβ induced cellular toxicity and overall health and function of *Drosophila* models used in AD research. MTT assay evaluated the cellular viability by measuring the oxidoreductase activity of 1X PBS-treated Control and **AK-2**-treated AD larval gut tissue.

The results indicated that there was a significant decrease in the % cell viability (60%, $^{***}p < 0.001$) of the AD gut tissue as compared to the control. In contrast, treatment with 1 µM and 5 µM of **AK-2** demonstrated an increase in % cell viability like 69% in 1 µM ($^{\pi}p < 0.05$) and 82% in 5 µM ($^{\pi\pi}p < 0.01$), respectively as compared to the AD group. However, treatment with 10 µM and 50 µM of **AK-2** revealed 62 and 75% cell viability as compared to the AD group as depicted in Figure 5.45B.

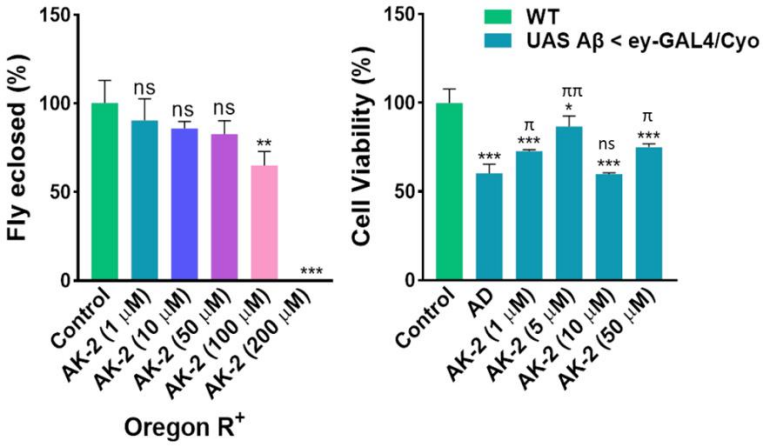

Figure 5.45. [A] The histogram represents the toxicity and percent of eclosed flies of treated and untreated groups. [B] The histogram represents the percent cell viability of control and AD larval gut tissue (n= 10 gut per group) at 570 nm. $^{*}p < 0.05$, $^{**}p < 0.01$, and $^{***}p < 0.001$ vs control; $^{\pi}p < 0.05$, $^{\pi\pi}p < 0.01$ vs AD; ns = non-significant; reported as Mean with SD. One-way ANOVA followed by Newman-Keuls Multiple Comparison test.

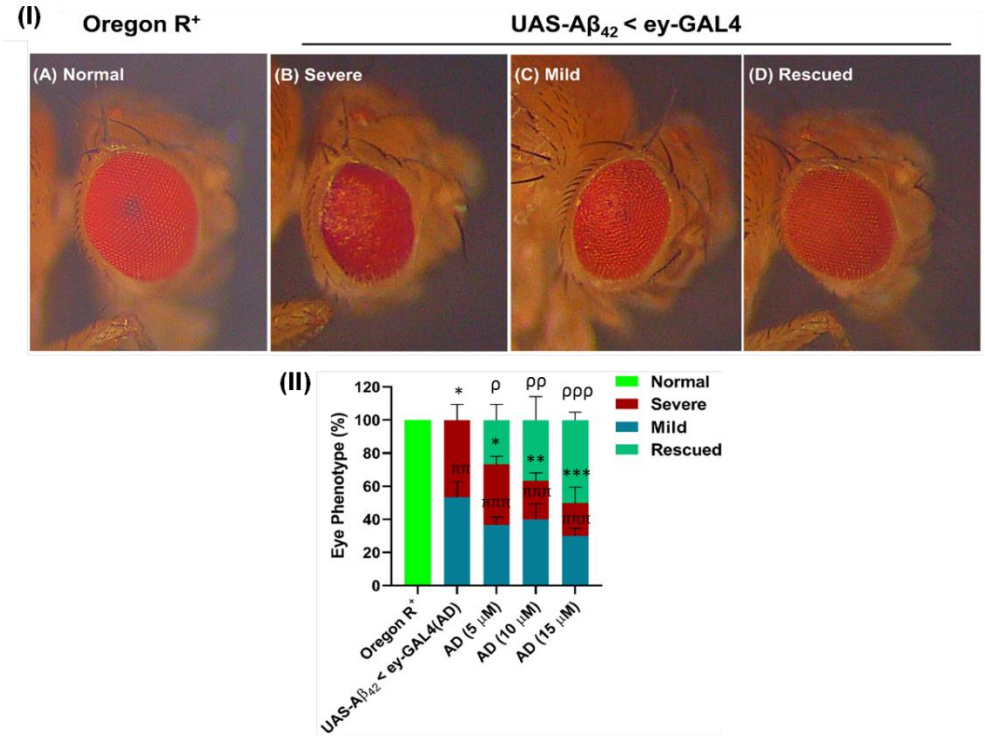

Figure 5.46. (I) Stereo zoom microscopic images (A) represent the normal eye phenotype in wild type (Oregon R^+), severe (B), mild (c), and rescued (D). The histogram (II) shows the percent of eye phenotypes treated with **AK-2**. $^{\rho}p < 0.05$, $^{\rho\rho}p < 0.01$, and $^{\rho\rho\rho}p < 0.001$ vs control in rescued case; $^{*}p < 0.05$, $^{**}p < 0.01$, and $^{***}p < 0.001$ vs control in severe case; $^{\pi\pi}p < 0.01$, and $^{\pi\pi\pi}p < 0.001$ vs control in mild case. Two-way ANOVA followed by Bonferroni posttest.

5.2.2.2.6.3. Drosophila eye phenotype

The genetically modified Aβ expressing AD (ey-GAL4 > UAS-$Aβ_{42}$) untreated flies when cultured on a normal food medium showed 53% mild and 47% severe eye ommatidial death phenotype as compared to normal wild-type flies which occurs in response to Aβ-induced ommatidial death. In contrast, the flies treated with compound **AK-2** showed a significant increase in % rescued (27, 36.6, and 57% in 5, 10, and 15 µM concentrations, respectively) of eye phenotypes in a dose-dependent manner as compared to the control wild type group. A significant decrease in % severe eye phenotype (36.6, 23.3, and 20% in 5, 10, and 15 µM concentrations, respectively) was observed in a dose-dependent manner as compared to the control wild-type group. Similarly, a significant

decrease in % mild eye phenotype (36.6, 37, and 30% in 5, 10, and 15 µM concentrations, respectively) was observed as compared to the control wild-type group (Figure 5.46). Additionally, the microscopic examination of the eye phenotype also corroborated the above findings. Current observations from *Drosophila* AD model studies indicate that the compound **AK-2** exhibits efficacy against Aβ-induced toxicity in both *in-vitro* and *in-vivo* experiments.

5.2.2.3. In-vivo blood-brain permeability assay

The *in-vivo* blood-brain permeability of compound **AK-2** was determined after administering 10 and 20 mg/kg doses to the experimental male Wistar rats (n=3) for four consecutive days. The rats were sacrificed on the fourth day and their brain homogenates were prepared. The calibration curve was plotted between area vs concentrations of compound **AK-2**. The concentrations of compound **AK-2** at their specific doses in the brain homogenates were determined. The results suggested that after administration of 10 and 20 mg/kg doses, the concentrations of **AK-2** in brain homogenates were observed to be 0.633 and 0.977 µg/mL which indicated that compound **AK-2** possessed the ability to cross the BBB and reached their specific site of action in the brain and also found more BBB permeable as compared to the previously reported compound **AV-2** (at 10 and 20 mg/kg doses = 0.015 and 0.054 µg/mL).

5.2.2.4. Pharmacokinetic studies

The pharmacokinetic study of compound **AK-2** was carried out at a dose of 20 mg/kg p.o. in healthy male Wistar rats. After dose administration, the blood was collected from the retro-orbital plexus at several time intervals (0.5, 1, 2, 3, 5, 7, 12, 24, and 32 h) and various pharmacokinetic parameters were estimated using the extravascular compartment model of PK solver software (version 2.0). The results suggested that the compound **AK-**

2 at T_{max} = 3 ± 0.4 h possessed C_{max} = 1.34 ± 0.21 µg/mL. The mean residual time (MRT) and elimination half-life were observed to be 6.07 ± 1.09 hr and 3.11 ± 0.3 h, respectively (Table 5.14) (Figure 5.47). These observations suggested that the compound **AK-2** has good bioavailability as well as oral absorption.

Table 5.14. The pharmacokinetic profile of orally administered compound **AK-2** (20 mg/kg).

Parameters	**Effect of compound AK-2**
C_{max} (µg/mL)	1.34 ± 0.21
T_{max} (h)	3 ± 0.4
$(AUC)_{0-t}$ (µg/mL*h)	6.99 ± 0.7
$t_{1/2}$ (h)	3.11 ± 0.3
MRT (h)	6.07 ± 1.09

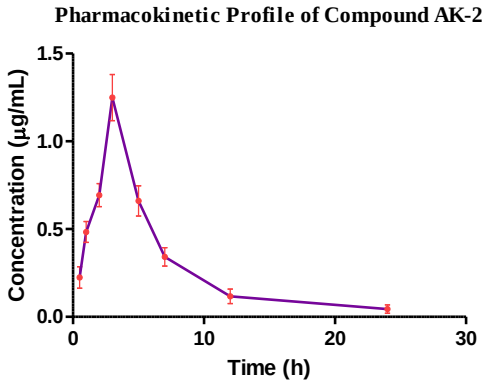

Figure 5.47. Pharmacokinetic analysis of compound **AK-2** representing its plasma concentration with respect to time.

5.2.3. Computational studies

5.2.3.1. Molecular docking studies

Using the Glide XP module of the Schrödinger Maestro 11.2, molecular docking experiments of compound **AK-2** were carried out [182]. The root-mean-square deviation (RMSD) value for hAChE and hBACE-1, respectively, was determined to be 0.0189 and

0.1752 (acceptable range < 2), following the extraction and re-docking of the co-crystallized bound ligands (donepezil for hAChE and F1M for hBACE-1) in the active sites of both enzymes for validating docking protocols (Figure 5.48). The binding modes of the co-crystallized and re-docked ligands were studied using the superimposition and XP visualizer tools. The consensus binding pattern of compound **AK-2** in the active sites of the enzymes hAChE (PDB: 4EY7), hBACE-1 (PDB: 2ZJM), and hAβ (PDB: 2BEG) was confirmed by the docking experiments. The docking scores of the compound **AK-2** were compared with the previously reported compound **AK-2** and standard donepezil (

Table **5.15**)

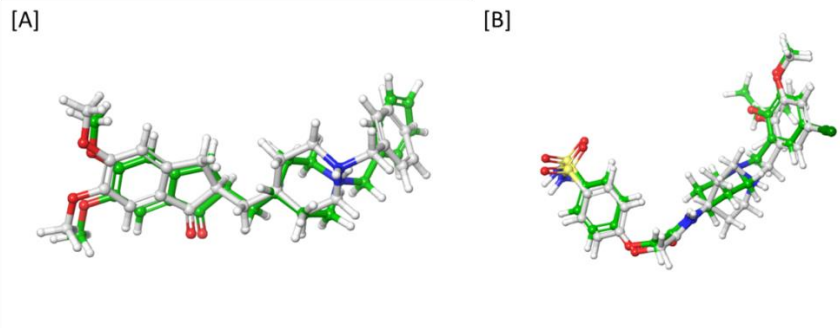

Figure 5.48. Superimposition images of re-docked ligands with the co-crstallized ones. [A] on hAChE (4EY7) (RMS: 0.0189); [B] on bBACE-1 (2ZJM) (RMS:0.1752).

5.2.3.1.1. Molecular docking studies on hAChE

The molecular docking results of compound **AK-2** against hAChE indicated that the quinazoline moiety was interacting with the Tyr72, Tyr124, Trp286, and Asp74 of the PAS region *via* hydrophobic and charged (negative) interactions, respectively. The π-cation interaction was observed between Tyr341 and protonated nitrogen of piperazine moiety. The compound **AK-2** has shown polar interactions with the Ser203 and His447 of the hAChE-CAS region. The Trp86 and Phe338 amino acid residues of the anionic subunit subsite showed hydrophobic interactions with **AK-2**. The Trp86 has also shown

π-π stacked interaction with the compound **AK-2**. The hydrophobic (Phe295 and Phe298) and glycine (Gly120 and Gly121) interactions were also observed in the acyl binding pocket and oxyanion hole, respectively with the compound **AK-2**. Overall, the compound **AK-2** has shown favorable binding affinity and interactions with the essential amino acids hence corroborating the *in-vitro* findings (Figure 5.49, Figure 5.53, and Figure 5.54).

5.2.3.1.2. Molecular docking studies on hBACE-1

The molecular docking studies of compound **AK-2** against hBACE-1 revealed that protonated nitrogen of piperazine moiety has shown charged and salt bridge interactions with the catalytic dyad region of hBACE-1 enzyme which is favorable of its inhibitory activity (Figure 5.50, Figure 5.53, and Figure 5.54). The docking score of the compound **AK-2** was found to be better as compared to the compound **AV-2** (

Table **5.15**).

5.2.3.1.3. Molecular docking studies on hAβ_{1-42}

To explore the potential binding sites linked with hAβ_{1-42}, we performed site-mapping software in the Schrödinger suite which analyzes the whole peptide and determines the potential binding site, especially in cases where the favorable binding sites are not known yet [251]. SiteMap generates a SiteScore which represents the binding sites including its characteristics like its size, solvent exposure, tightness between receptor-site point interactions, hydrophobicity and hydrophilicity balance, and degree of hydrogen bond acceptance and donation. An indication of a prospective binding site is a SiteScore ≈ 1. The findings of SiteMap analysis on hAβ_{1-42} indicated that there are two predicted binding sites {site 1: SiteScore (0.989) and druggability (Dscores) (0.988) and site 2:

SiteScore (0.751) and druggability (Dscores) (0.754)} (Figure 5.51). Therefore, site 1 was selected for various computational studies due to its better Sitecore and Dscore as compared to site 2.

Further, to investigate the binding profile of compound **AK-2** with hA$\beta_{1\text{-}42}$, molecular docking studies were executed. The results suggested that compound **AK-2** interacted with the chain A, B, C, D, and E amino acid residues. Amino acids residues of chain A (Leu17 and Phe19), chain B (Leu17, Val18, and Phe19), chain C (Leu17, Val18, Phe19, Val40, and Ala42), chain D (Leu17, Val40, and Ala42), and chain E (Leu17, Val40, and Ala42) were hydrophobically interacted with the compound **AK-2**. Additionally, Gly38 of chain D showed glycine interaction with **AK-2**. Overall, docking studies revealed that compound **AK-2** interacted with hA$\beta_{1\text{-}42}$ protofibrils and modulated its aggregation (Figure 5.52, Figure 5.53, and Figure 5.54).

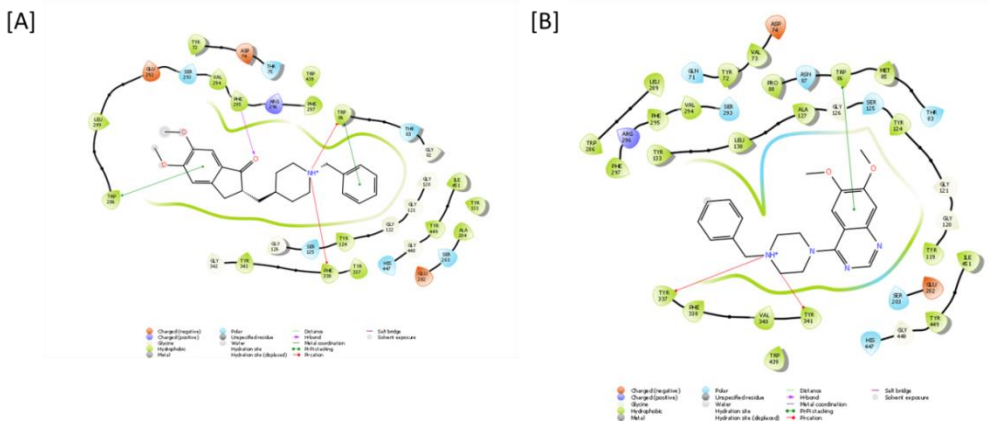

Figure 5.49. 2D binding interaction of [A] donepezil and [B] compound **AK-2** on hAChE active site.

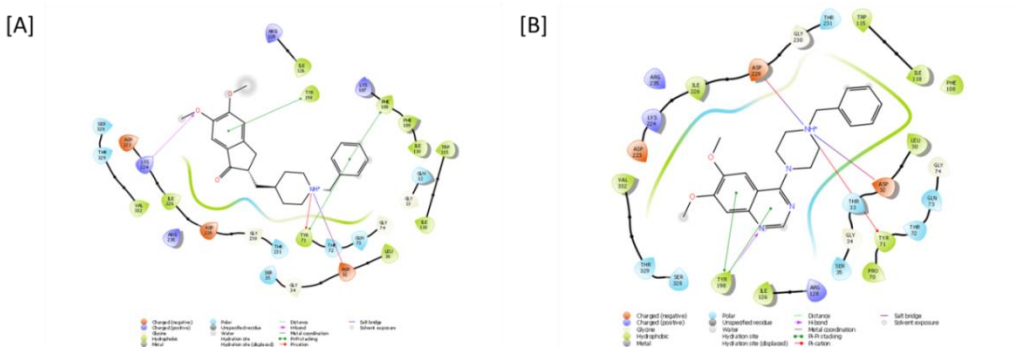

Figure 5.50. 2D binding interaction of [A] donepezil and [B] compound **AK-2** on hBACE-1 active site.

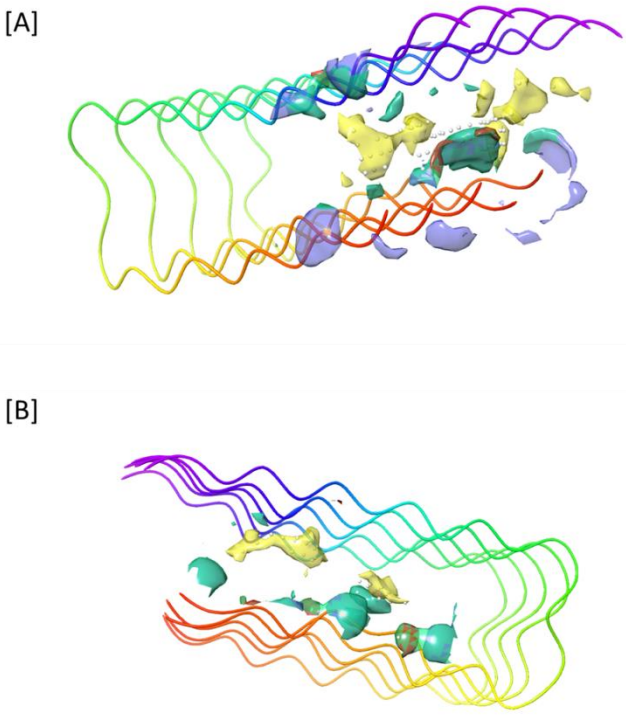

Figure 5.51. Site mapping analysis for favorable binding site prediction on hAβ (2BEG). [A] Site 1 and [B] Site 2. H-bond acceptor region (Red), H-bond donor region (Blue), Hydrophilic region (Green), Hydrophobic region (Yellow), and Metal binding region (Pink).

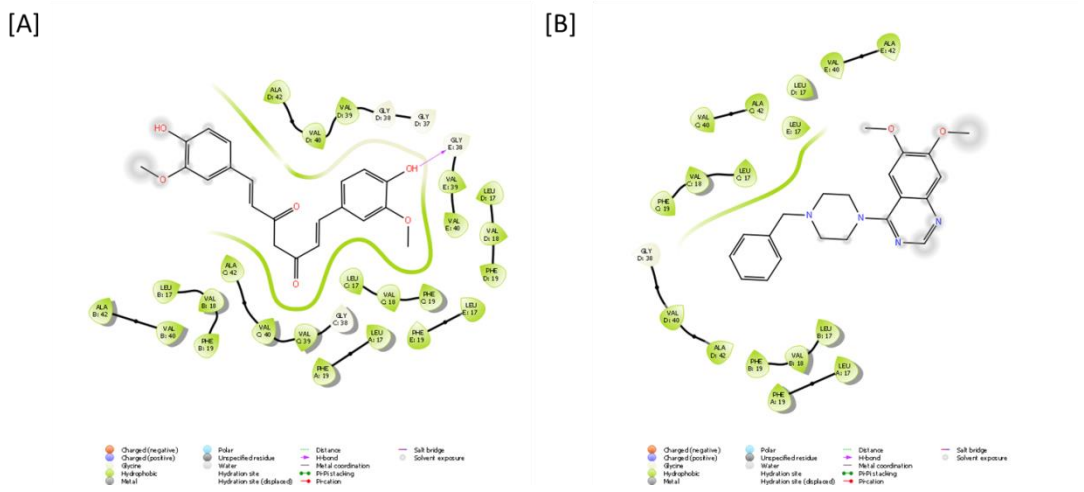

Figure 5.52. 2D binding interaction of [A] curcumin and [B] compound **AK-2** on hAβ active site.

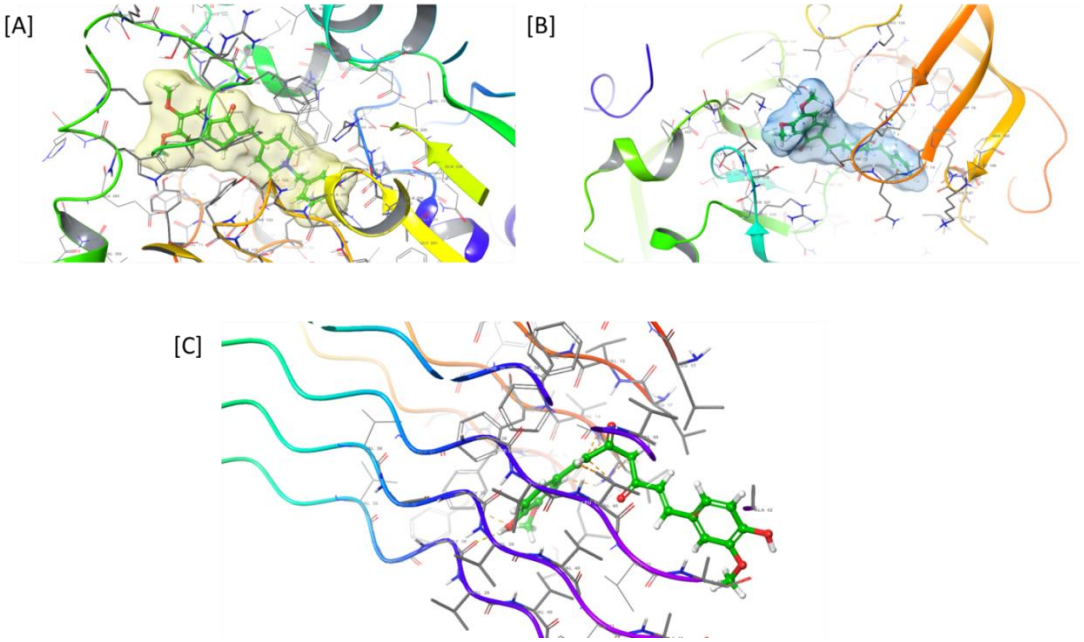

Figure 5.53. 3D binding interactions of standard compounds on their respective enzymes. [A] donepezil on hAChE; [B] donepezil on hBACE-1; and [C] curcumin on $hA\beta_{1\text{-}42}$.

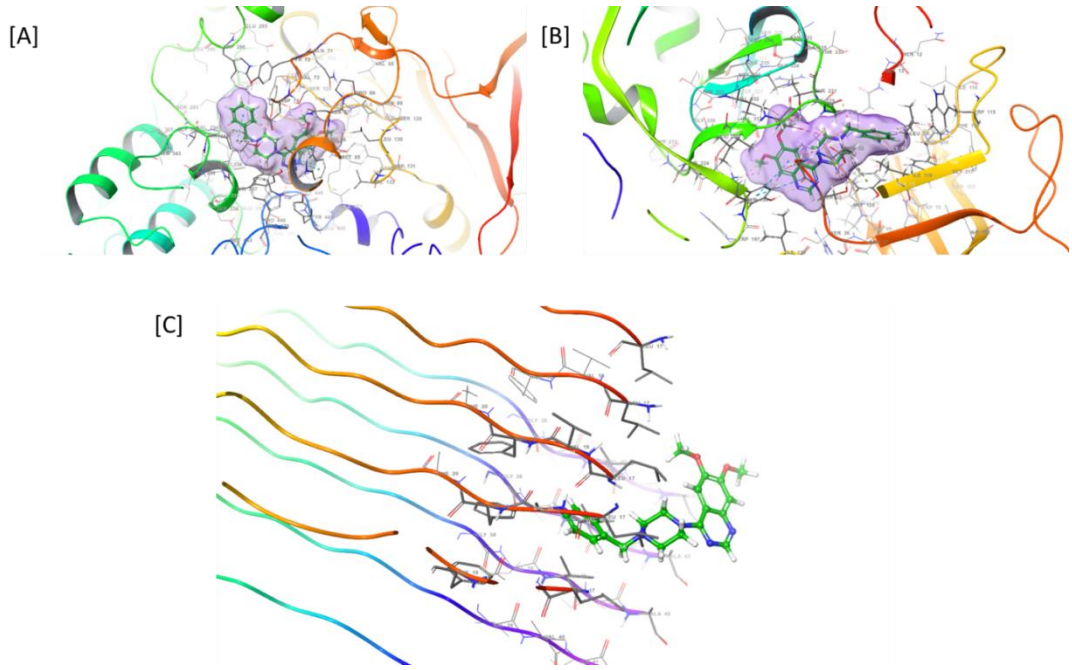

Figure 5.54. 3D binding interaction of compound **AK-2** with [A] hAChE (4EY7); [B] hBACE-1 (2ZJM); and [C] hAβ (2BEG), respectively.

Table 5.15. Docking scores of the compounds and standard with [A] hAChE and [B] hBACE-1 enzymes.

S.No.	Compound	Docking Scores on	
		hAChE (PDB:4EY7)	**hBACE-1 (PDB: 2ZJM)**
1.	**AK-2**	-11.72	-5.91
2.	**AV-2**	-14.90	-5.79
3.	**Donepezil**	-13.57	-5.35

5.2.3.2. *MD simulation studies*

The Desmond module of the Schrodinger suite was used to execute the MD simulation run of 100 ns for the ligand-protein complexes of compound **AK-2** with hAChE, hBACE-1, and $hA\beta_{1\text{-}42}$ to better conceive the docked complex stability [187]. The MD simulation findings of compound **AK-2** with hAChE, hBACE-1, and $hA\beta_{1\text{-}42}$ docked complex

revealed that the root-mean-square deviation (RMSD) was found to be below the permissible limit 3 Å and steady trajectory throughout the 100 ns simulation run.

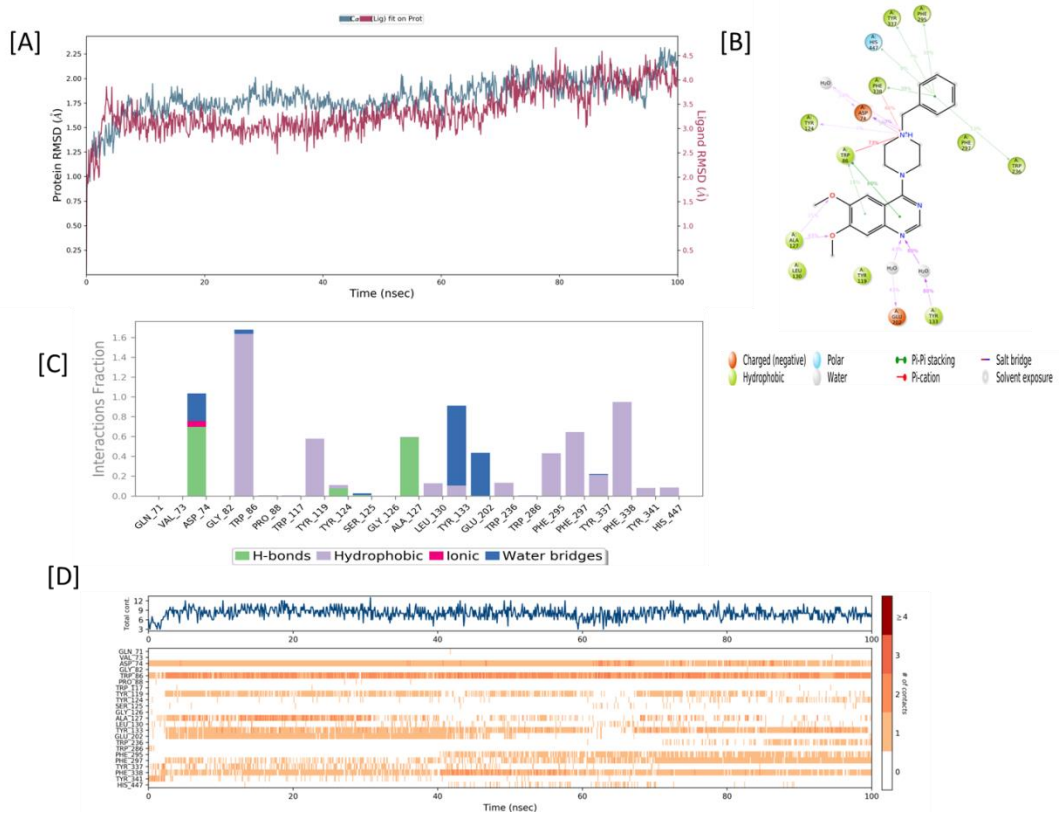

Figure 5.55. MD simulation study of **AK-2**-hAChE (4EY7) ligand-protein docked complex. [A] RMSD graph; [B] 2D interaction diagram of compound **AK-2** with the active region of hAChE; [C] Histogram revealing ligand interaction fractions with the active region of hAChE; [D] Timeline displaying protein-ligand interactions throughout 100 ns.

The binding profile of the ligand-protein complex of compound **AK-2** with hAChE demonstrated that the piperazine ring showed H-bond, ionic, and water bridge interaction with the Asp74 of PAS region of hAChE (1.0 interaction fraction (IF)). The hydrophobic and polar interactions were observed between the benzyl ring and His447 of the CAS active site of hAChE. The quinazoline and benzyl ring showed hydrophobic and π-π stacked interaction with the Trp86 (1.6 IF) and Phe338 (1.0 IF) amino acid residues of the anionic subunit subsite. The benzyl ring is also involved in the formation of hydrophobic

interactions with the Phe295 (0.4 IF) and Phe297 (0.7 IF) of the acyl binding pocket (Figure 5.55).

The binding profile of compound **AK-2** with hBACE-1 suggested that the protonated piperazine moiety showed H-bond (1.0 IF) and ionic interactions (0.7 IF) with the CAS region of hBACE-1 and found better as compared to the compound **AV-2** (1.0 IF at 1.0 Asp32 and 0.21 at Asp228) (Figure 5.56).

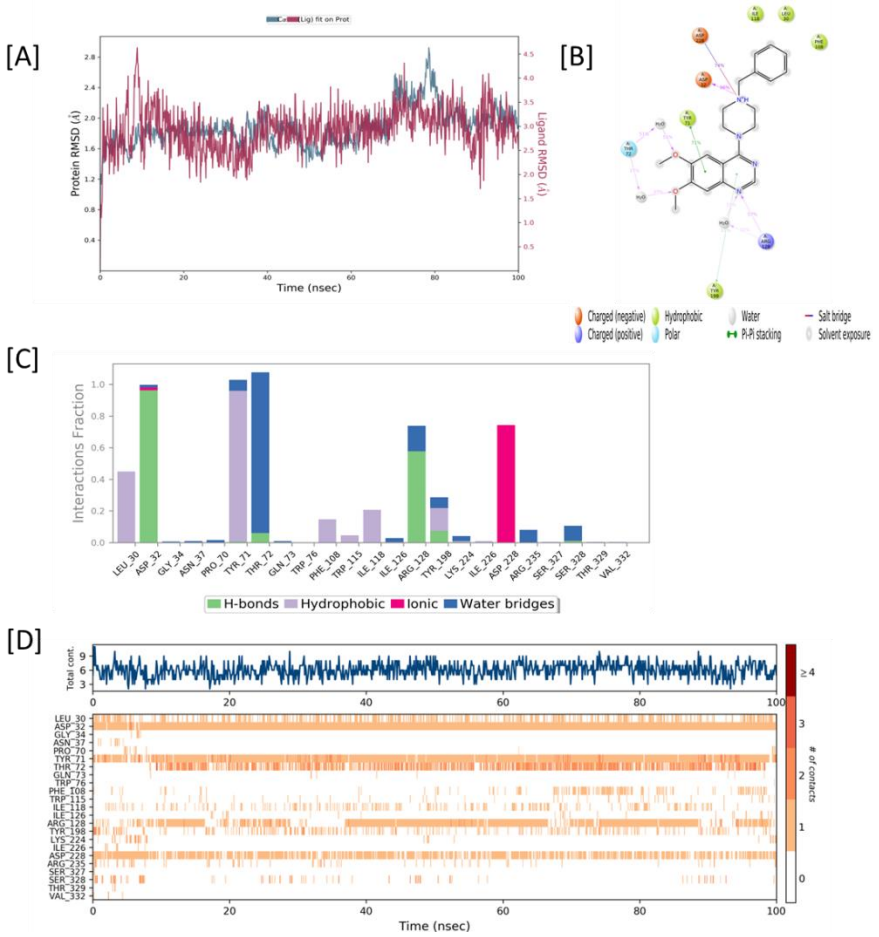

Figure 5.56. MD simulation study of **AK-2**-hBACE-1 (2ZJM) ligand-protein docked complex. [A] RMSD graph; [B] 2D interaction diagram of compound **AK-2** with the active region of hBACE-1; [C] Histogram revealing ligand interaction fractions with the active region of hAChE; [D] Timeline displaying protein-ligand interactions throughout 100 ns.

Moreover, the binding profile of compound **AK-2** with hAβ_{1-42} revealed that it showed hydrophobic interactions with the active amino acid residues of the peptide chains of hAβ_{1-42} (Figure 5.57).

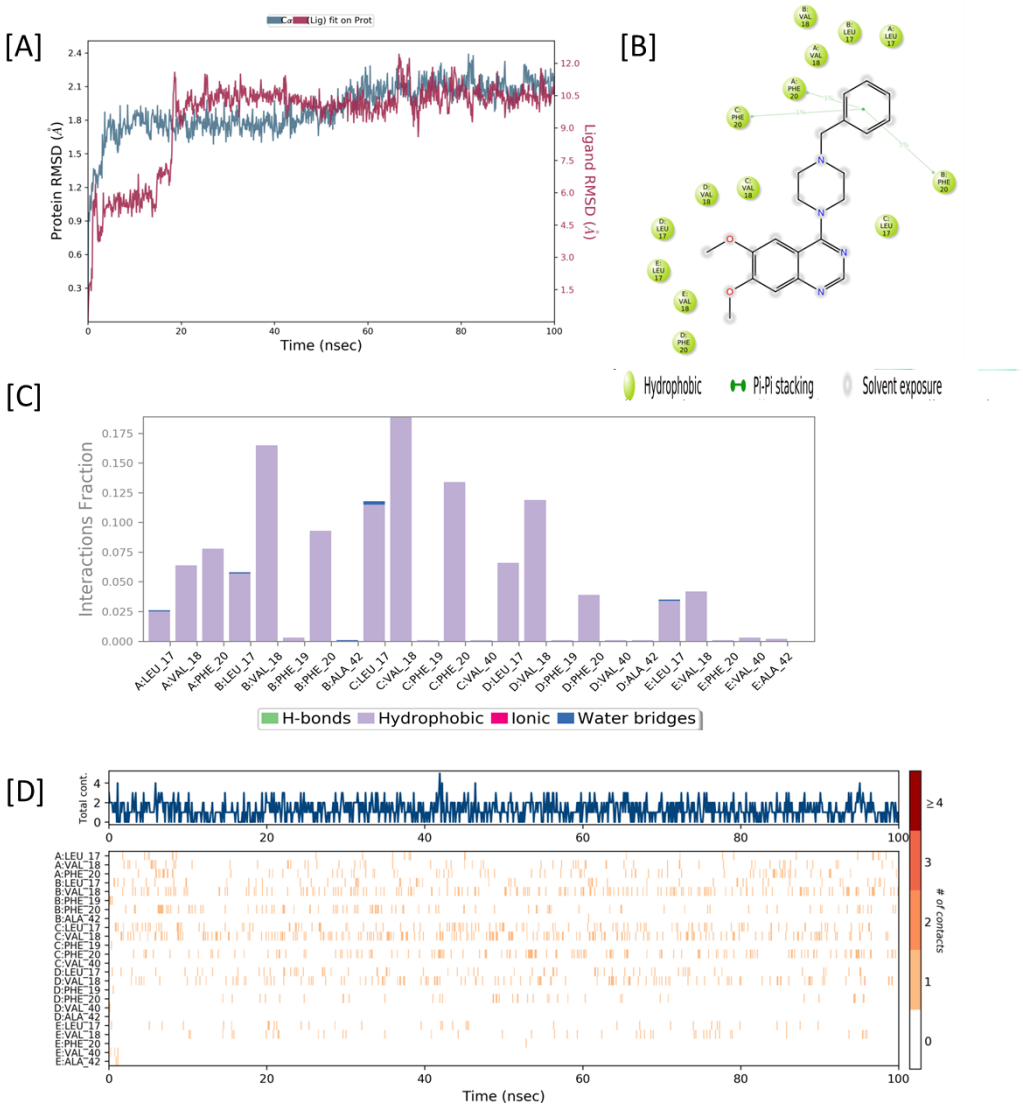

Figure 5.57. MD simulation study of **AK-2**-hAβ (2BEG) ligand-protein docked complex. [A] RMSD graph; [B] 2D interaction diagram of compound **AK-2** with the active region of hBACE-1; [C] Histogram revealing ligand interaction fractions with the active region of hAChE; [D] Timeline displaying protein-ligand interactions throughout 100 ns.

5.2.3.3. MM-GBSA analysis

The binding free energy between protein-ligand complexes was predicted using the molecular mechanics/generalized Born surface area (MM/GBSA) module of Maestro

11.2 [252]. This binding energy was calculated by combining the energies associated with the electrostatic solvation energy (GB), non-electrostatic solvation energy, and gas-phase energy (MM). The MM/GBSA of docked poses of the most promising compound **AK-2** with both hAChE and hBACE-1 was determined and compared with the standard donepezil and F1M. The results suggested that binding free energy of compound **AK-2** with both enzymes was found to be comparable to the standards and represented in Table 5.16.

Table 5.16. MM-GBSA analysis of compound **AK-2** with hAChE, hBACE-1, and hAβ enzymes.

Targeted enzyme	Compound	ΔG binding free energy
hAChE	Donepezil	-65.189
	AK-2	-40.853
hBACE-1	F1M	-36.77
	AK-2	-47.027
Aβ	Curcumin	-47.855
	AK-2	-28.554

5.2.3.4. *ADME drug-likeness analysis*

The various drug-like parameters like donor HB, accept HB, total solvent-accessible surface area (SASA), octanol/water partition coefficient ($QPlogP_{o/w}$), blood-brain partition coefficient (QPlog BB), Caco-2 cell permeability (QPCaco), and % human oral absorption (%HOA) of compound **AK-2** and standard donepezil were predicted using QikProp module of Schrodinger [Lipinski 2004]. The results suggested that the compound **AK-2** possessed drug-like properties like Mol_MW < 500, Donor HB < 5, Acceptor HB < 20, SASA < 1000, and Qplogo/w > 2 with good % HOA which indicated that compound **AK-2** was following the Rule of Five and found comparable with the

standard drug donepezil. The results of ADME drug-likeness analysis are represented in Table 5.17.

Table 5.17. ADME drug-likeness analysis of compound **AK-2**.

Compound	Mol_Wt[a]	Donor HB[b]	Acceptor HB[c]	SASA[d]	QplogBB[e]	Qplogo/w[f]	%HOA	Rule of Five
Donepezil	393.61	1	7.3	759.44	0.13	4.29	100	Yes
AK-2	364.18	0	6.0	646.14	0.35	3.56	100	Yes

[a]Mol_MW- Compound molecular weight (130 to 725).

[b]Donor HB- Hydrogen bond donor (0.0 to 5.0).

[c]Acceptor HB- Hydrogen bond acceptor (2.0 to 20.0).

[d]SASA- Total solvent accessible surface area (SASA) (300 to 1000).

[e]QPlogBB- Brain/blood partition coefficient (-3.0 to 1.2).

[f]QPlogPo/w- Predicted octanol/water partition coefficient (-2.0 to 6.5).

5.2.3.5. DFT-based computational studies

5.2.3.5.1. Frontier molecular orbitals studies

The highest occupied molecular orbital (HOMO) and lowest unoccupied molecular orbitals (LUMO) are referred to as Frontier molecular orbitals (FMOs) which are responsible for determining the global reactivity descriptors and hence stability of the compound. Based on the FMO studies, the energy associated with the HOMO and LUMO i.e., E_{HOMO} and $E_{LUMO,}$ and their energy difference were used to predict the stability, hardness, softness, and reactivity of the compound. The large energy gap reveals that the molecule is highly stable and hard while the lower energy gap indicates that the molecule is highly reactive and soft [Fleming 1976, Fukui 2006]. The results of FMO studies of compound **AK-2** indicated that the energy gaps in the gaseous environment were found to be 0.2196 kcal/mol (between E_{HOMO} and E_{LUMO}) and 0.2029 kcal/mol (between E_{LUMO+1} and E_{HOMO-1}) (Figure 5.58). Similarly, the energy gaps in the aqueous environment were

found to be 0.148 kcal/mol (between E_{HOMO} and E_{LUMO}) and 0.202 kcal/mol (between E_{LUMO+1} and E_{HOMO-1}) which demonstrated that compound **AK-2** is chemically stable in aqueous environments as compared to the gaseous (Figure 5.59).

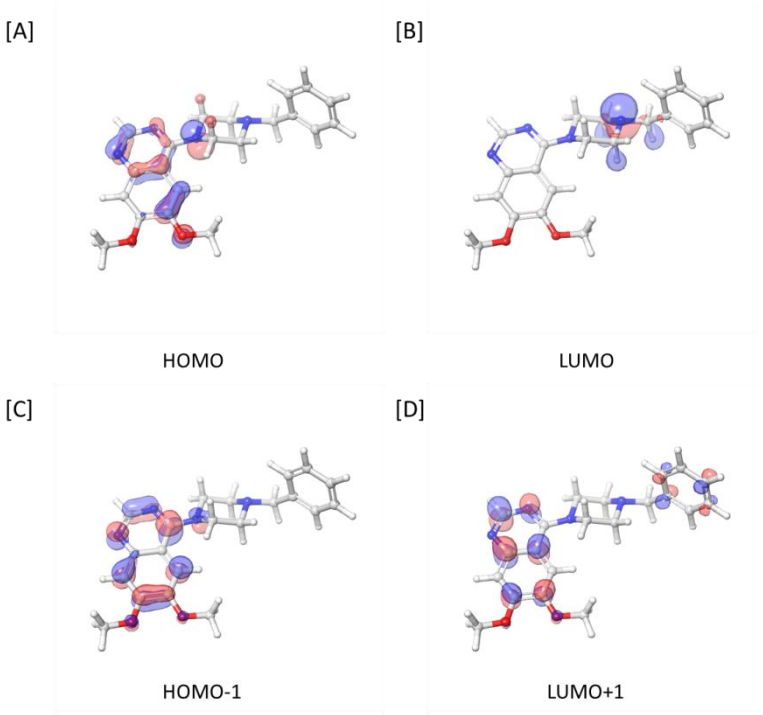

Figure 5.58. HOMO-LUMO orbital density of the compound **AK-2** in gaseous environment; A & C) HOMO and HOMO-1 orbital density of compound **AK-2**; B & D) LUMO and LUMO+1 orbital density of compound **AK-2**.

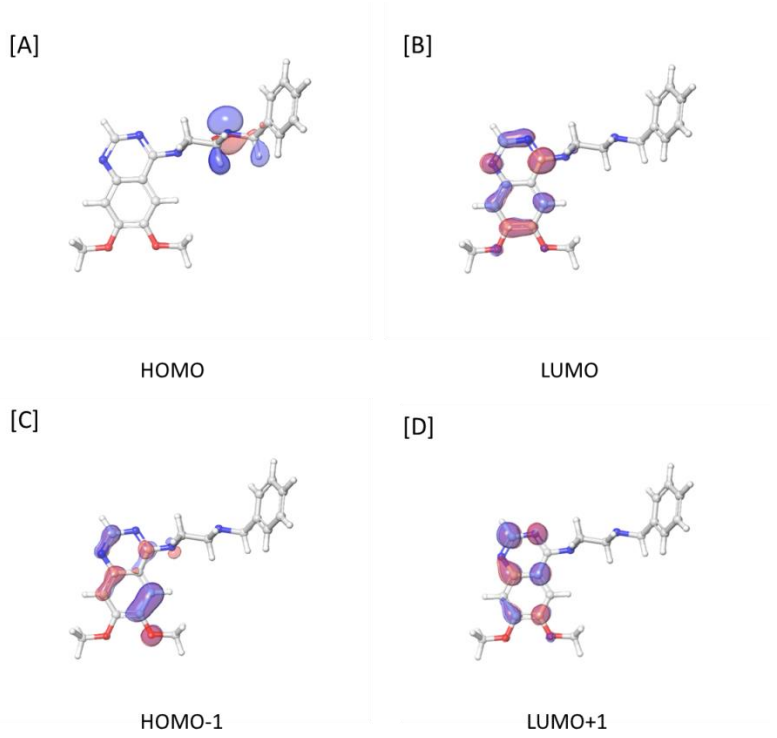

Figure 5.59. HOMO-LUMO orbital density of the compound **AK-2** in aqueous environment; A & C) HOMO and HOMO-1 orbital density of compound **AK-2**; B & D) LUMO and LUMO+1 orbital density of compound **AK-2**.

5.2.3.5.2. Global reactivity descriptors

The global reactivity descriptors like electron affinity (A), ionization potential (I), electronegativity (X), hardness (η), electrophilicity (ω), chemical potential (μ), and global softness (σ) were also considered to be an important parameter which was determined by using calculated E_{HOMO} and E_{LUMO} energies and their gaps [Chattaraj et al. 2003]. The results of compound **AK-2** demonstrated that the electron affinity (A) and ionization potential (I) were observed to be 0.0544 and 0.1651 kcal/mol in a gaseous environment and 0.0743 and 0.2221 kcal/mol in aqueous environment. The small difference between the electron affinity and ionization potential suggested that the compound **AK-2** could be kinetically reactive and have more electron-donating potential. The electronegativity (X) and hardness (η) of compound **AK-2** were calculated and found to be 0.1098 and 0.0553 kcal/mol in a gaseous environment and 0.259 and 0.185 kcal/mol in an aqueous

environment. Moreover, the chemical potential (μ), electrophilicity (ω), and global softness (σ) were also estimated and found to be -0.1098, 0.1089, and 0.9041 kcal/mol in a gaseous environment while -0.148, 0.059, and 0.0925 kcal/mol in aqueous environment, respectively.

5.2.3.5.3. Fukui function analysis

The Fukui function analysis of compound **AK-2** was performed and the probable reactive sites for electrophilic (f^-) and nucleophilic (f^+) attacks were investigated. The results of the Fukui function analysis revealed that the probable reactive sites for electrophilic (f^-) attack were both –O- groups, and -N atoms of quinazoline and piperazine rings. Probable reactive sites for nucleophilic (f^+) attack were also quinazoline and piperazine rings. The reactive sites for both electrophilic (f^-) and nucleophilic (f^+) attacks were represented in Figure 5.60. These findings demonstrated that compound **AK-2** possessed both the electrophilic and nucleophilic centers which are responsible for various interactions at the active binding sites of targeted enzymes.

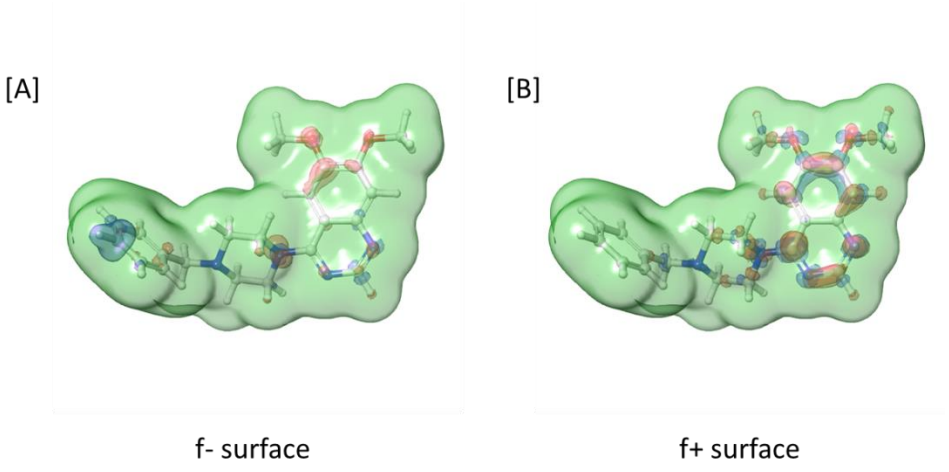

Figure 5.60. Graphical representations of fukui functions and [A] Nucleophilic fukui function - ve *f* (r) left, [B] Electrophilic fukui function + ve *f* (r) right.

5.2.3.5.4. Molecular electrostatic potential (MEP) analysis

The MEP analysis is a 3D plot electron density map which is considered to be an important parameter as it helps in predicting the electrophilic, nucleophilic attacks and non-covalent interactions of ligands. The electron density map as well as the electrostatic potential of compound **AK-2** was determined in both gaseous and aqueous environments [Ramirez-Balderrama et al. 2017]. The results indicated that nitrogen and oxygen atoms displaying light red color represent the negative zone where the chances of an electrophilic attack are more, light blue represents the positive zone where the probability of a nucleophilic attack is more and white color indicates zero electrostatic potential (Figure 5.61).

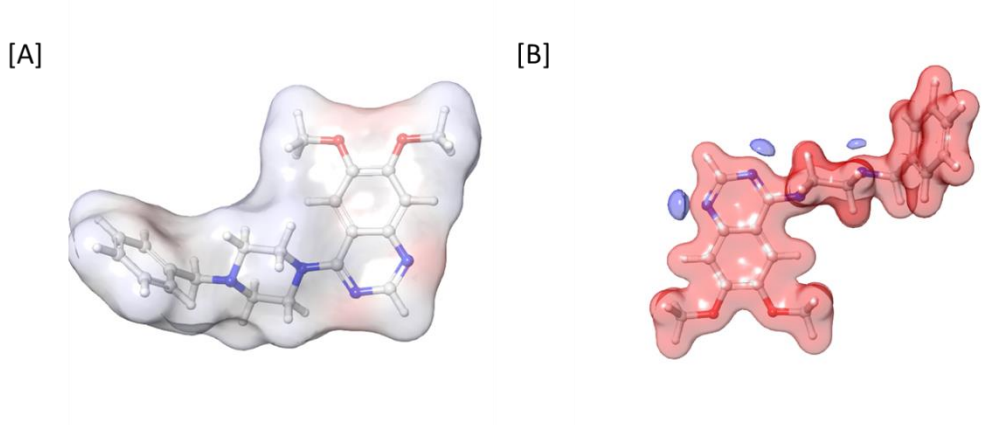

Figure 5.61. Graphical representation of molecular electrostatic potential (MEP) surface of the compound **AK-2**. [A] in gaseous [B] in aqueous environment.

5.2.3.5.5. pKa analysis

pKa is an important parameter that demonstrates the acidity or basicity of the molecule and hence the ability to donate or accept the proton [Brunetti et al. 2022]. The pKa_s of all the nitrogen atoms of piperazine in compound **AK-2** were predicted and the results revealed that the pKa_s of the nitrogen atoms of piperazine were observed to be 7.2 (linked with benzyl group) and 0.6 (linked with quinazoline moiety) which indicated that

nitrogen atom linked with benzyl group easily gets protonated at physiological pH and hence responsible for BACE-1 inhibition.